



저작자표시-비영리-변경금지 2.0 대한민국

이용자는 아래의 조건을 따르는 경우에 한하여 자유롭게

- 이 저작물을 복제, 배포, 전송, 전시, 공연 및 방송할 수 있습니다.

다음과 같은 조건을 따라야 합니다:



저작자표시. 귀하는 원저작자를 표시하여야 합니다.



비영리. 귀하는 이 저작물을 영리 목적으로 이용할 수 없습니다.



변경금지. 귀하는 이 저작물을 개작, 변형 또는 가공할 수 없습니다.

- 귀하는, 이 저작물의 재이용이나 배포의 경우, 이 저작물에 적용된 이용허락조건을 명확하게 나타내어야 합니다.
- 저작권자로부터 별도의 허가를 받으면 이러한 조건들은 적용되지 않습니다.

저작권법에 따른 이용자의 권리는 위의 내용에 의하여 영향을 받지 않습니다.

이것은 [이용허락규약\(Legal Code\)](#)을 이해하기 쉽게 요약한 것입니다.

[Disclaimer](#)

공학박사학위논문

축류팬에서 익단 누설 유동의 방랑 운동에  
대한 실험적 연구

Experimental study on the wandering motion of tip-  
leakage flow in an axial flow fan

2019 년 2 월

서울대학교 대학원

기계항공공학부

이 홍 권

# 축류팬에서 익단 누설 유동의 방랑 운동에 대한 실험적 연구

Experimental study on the wandering motion of tip-leakage flow in an axial flow fan

지도교수 최 해 천

이 논문을 공학박사 학위논문으로 제출함

2018 년 10 월

서울대학교 대학원

기계항공공학부

이 홍 권

이홍권의 공학박사 학위논문을 인준함

2018 년 12 월

위원장 : 송 성 진



부위원장 : 최 해 천



위원 : 박 형 민



위원 : 황 원 태



위원 : 안 준



# Experimental study on the wandering motion of tip-leakage flow in an axial flow fan

Hongkwon Lee

Department of Mechanical & Aerospace Engineering

Seoul National University

## Abstract

The characteristics of tip-leakage vortex (TLV) in a low-pressure axial flow fan are investigated using a digital particle image velocimetry. The blade rotational speed is fixed at 1,000 rpm for four different flow rates, and the Reynolds number is 547,000 based on the blade tip radius and tip velocity. The evolution of TLV in downstream is highly influenced by the incoming flow rate. A strong TLV is observed for higher flow rates, and the TLV breakup is found at the blade trailing edge for a peak efficiency- and stall conditions. The TLV breaks up sometimes at even higher flow rate. As the flow rate decreases, the TLV locates further upstream, and at the peak efficiency condition, the migration speed is faster than the higher flow condition due to the TLV breakup. The scatter plot of the TLV center location indicates that the TLV wanders around its mean location and the region swept by the wandering motion increases as the TLV migrates downstream. High turbulent kinetic energy exists at the phase-averaged TLV center and its upstream location, respectively, owing to the wandering motion and the interaction between the TLV and main axial flow. For the higher flow rates, the TLV presented near the blade trailing edge and casing wall rapidly decays as it moves out of the duct outlet. In the down-

stream of the outlet, the azimuthal migration speed of the TLV is faster than that of the blade wake, and thus it interacts with the wake of the next blade. The TLV, together with the blade wake, interferes the main flow and reduces fan performance.

Keywords: axial flow fan, particle image velocimetry, tip-leakage vortex, wandering motion, breakup

Student number: 2009-20713

# Contents

<b>Abstract</b>	<b>i</b>
<b>Contents</b>	<b>iii</b>
<b>List of Figures</b>	<b>xvii</b>
<b>Nomenclature</b>	<b>xviii</b>
<b>Chapter</b>	
<b>1 Introduction</b>	<b>1</b>
<b>2 Experimental Set-up</b>	<b>5</b>
2.1 Axial flow fan model . . . . .	5
2.2 Axial flow fan test system . . . . .	6
2.3 The fan performance . . . . .	7
2.4 Digital particle image velocimetry . . . . .	9
<b>3 Results and Discussion</b>	<b>24</b>
3.1 Stall condition of $\varphi= 0.231$ . . . . .	24
3.2 Peak efficiency condition of $\varphi= 0.276$ . . . . .	25
3.3 Over flow conditions of $\varphi= 0.353, 0.366$ . . . . .	25
3.4 Instantaneous tip-leakage vortex . . . . .	26
3.5 Tip-leakage vortex at the blade wake . . . . .	30
<b>4 Summary and Concluding Remarks</b>	<b>87</b>



# List of Figures

## Figure

1.1	Schematic diagram of tip-leakage flow and tip-leakage vortex in axial compressor blades (modified from Fischer <i>et al.</i> (2012)). . . . .	4
2.2	Schematic diagram of the axial flow fan: (a) front view; (b) side view. . . . .	13
2.3	Axial flow fan system. . . . .	14
2.4	Schematic diagram of the screen. . . . .	15
2.5	The experimental set-up for the velocity and pressure rise measurements: (a) schematic diagram of the pitot tube set-up; (b) the measurement locations of four radial directions. . . . .	16
2.6	Results of the measurement for condition 1 (see Table 2.3): (a) velocity profile for the volume flow rate; (b) static pressure profile for the total-to-static pressure rise. . . . .	17
2.7	Results of the measurement for condition 2 (see Table 2.3): (a) velocity profile for the volume flow rate; (b) static pressure profile for the total-to-static pressure rise. . . . .	18
2.8	Results of the measurement for condition 3 (see Table 2.3): (a) velocity profile for the volume flow rate; (b) static pressure profile for the total-to-static pressure rise. . . . .	19
2.9	Results of the measurement for condition 4 (see Table 2.3): (a) velocity profile for the volume flow rate; (b) static pressure profile for the total-to-static pressure rise. . . . .	20



2.10	Performance curves of the fan: pressure coefficient ( $\psi$ ) and efficiency ( $\eta$ ) versus flow coefficient ( $\varphi$ ). . . . .	21
2.11	Experimental set-up for digital PIV measurements:(a) signal processing for triggering the laser and camera simultaneously; (b) PIV planes for the blade wake. In (a), $f_{fan}$ is the fan rotating frequency. . . . .	22
2.12	Experimental set-up for digital PIV measurements for the blade passage flow:(a) side view; (b) perspective view; (c) PIV planes (green colored planes). In (a), the angle from the centerline to the chord line is $56.5^\circ$ , and the laser sheet (red arrow) is tilted downward by $33.5^\circ$ from the centerline. . . . .	23
3.1	The particle image of the PIV plane near the trailing edge. . . . .	32
3.2	Instantaneous velocity vectors and contours of the instantaneous vorticity in the direction normal to the PIV planes for $\varphi = 0.231$ . The grey area at the location of $\textcircled{1}$ indicates the shadow caused by the blade. The thick black and red lines in these figures denote the locations of internal casing wall and outlet edge of the casing, respectively (see Figure 3.1). . . . .	33
3.3	Instantaneous velocity vectors and contours of the instantaneous vorticity in the direction normal to the PIV planes for $\varphi = 0.231$ . The thick black and red lines in these figures denote the locations of internal casing wall and outlet edge of the casing, respectively (see Figure 3.1). . . . .	34

3.4	Instantaneous velocity vectors and contours of the instantaneous vorticity in the direction normal to the PIV planes for $\varphi = 0.231$ . The thick black and red lines in these figures denote the locations of internal casing wall and outlet edge of the casing, respectively (see Figure 3.1). . . . .	35
3.5	Contours of the phase-averaged vorticity in the direction normal to the PIV planes, together with the phase-averaged velocity vectors for $\varphi = 0.231$ . The grey area at the location of ① indicates the shadow caused by the blade. The thick black and red lines in these figures denote the locations of internal casing wall and outlet edge of the casing, respectively (see Figure 3.1). . . . .	36
3.6	Contours of the phase-averaged vorticity in the direction normal to the PIV planes, together with the phase-averaged velocity vectors for $\varphi = 0.231$ . The thick black and red lines in these figures denote the locations of internal casing wall and outlet edge of the casing, respectively (see Figure 3.1). . . . .	37
3.7	Contours of the phase-averaged vorticity in the direction normal to the PIV planes, together with the phase-averaged velocity vectors for $\varphi = 0.231$ . The thick black and red lines in these figures denote the locations of internal casing wall and outlet edge of the casing, respectively (see Figure 3.1). . . . .	38
3.8	Instantaneous velocity vectors and contours of the instantaneous vorticity in the direction normal to the PIV planes for $\varphi = 0.276$ . The grey area at the location of ① indicates the shadow caused by the blade. The thick black and red lines in these figures denote the locations of internal casing wall and outlet edge of the casing, respectively (see Figure 3.1). . . . .	39

3.9	Instantaneous velocity vectors and contours of the instantaneous vorticity in the direction normal to the PIV planes for $\varphi = 0.276$ . The thick black and red lines in these figures denote the locations of internal casing wall and outlet edge of the casing, respectively (see Figure 3.1). . . . .	40
3.10	Instantaneous velocity vectors and contours of the instantaneous vorticity in the direction normal to the PIV planes for $\varphi = 0.276$ . The thick black and red lines in these figures denote the locations of internal casing wall and outlet edge of the casing, respectively (see Figure 3.1). . . . .	41
3.11	Contours of the phase-averaged vorticity in the direction normal to the PIV planes, together with the phase-averaged velocity vectors for $\varphi = 0.276$ . The grey area at the location of $\textcircled{1}$ indicates the shadow caused by the blade. The thick black and red lines in these figures denote the locations of internal casing wall and outlet edge of the casing, respectively (see Figure 3.1). . . . .	42
3.12	Contours of the phase-averaged vorticity in the direction normal to the PIV planes, together with the phase-averaged velocity vectors for $\varphi = 0.276$ . The thick black and red lines in these figures denote the locations of internal casing wall and outlet edge of the casing, respectively (see Figure 3.1). . . . .	43
3.13	Contours of the phase-averaged vorticity in the direction normal to the PIV planes, together with the phase-averaged velocity vectors for $\varphi = 0.276$ . The thick black and red lines in these figures denote the locations of internal casing wall and outlet edge of the casing, respectively (see Figure 3.1). . . . .	44

3.14	Instantaneous velocity vectors and contours of the instantaneous vorticity in the direction normal to the PIV planes for $\varphi = 0.353$ . The grey area at the location of ① indicates the shadow caused by the blade. The thick black and red lines in these figures denote the locations of internal casing wall and outlet edge of the casing, respectively (see Figure 3.1). . . . .	45
3.15	Instantaneous velocity vectors and contours of the instantaneous vorticity in the direction normal to the PIV planes for $\varphi = 0.353$ . The thick black and red lines in these figures denote the locations of internal casing wall and outlet edge of the casing, respectively (see Figure 3.1). . . . .	46
3.16	Instantaneous velocity vectors and contours of the instantaneous vorticity in the direction normal to the PIV planes for $\varphi = 0.353$ . The thick black and red lines in these figures denote the locations of internal casing wall and outlet edge of the casing, respectively (see Figure 3.1). . . . .	47
3.17	Contours of the phase-averaged vorticity in the direction normal to the PIV planes, together with the phase-averaged velocity vectors for $\varphi = 0.353$ . The grey area at the location of ① indicates the shadow caused by the blade. The thick black and red lines in these figures denote the locations of internal casing wall and outlet edge of the casing, respectively (see Figure 3.1). . . . .	48
3.18	Contours of the phase-averaged vorticity in the direction normal to the PIV planes, together with the phase-averaged velocity vectors for $\varphi = 0.353$ . The thick black and red lines in these figures denote the locations of internal casing wall and outlet edge of the casing, respectively (see Figure 3.1). . . . .	49

3.19	Contours of the phase-averaged vorticity in the direction normal to the PIV planes, together with the phase-averaged velocity vectors for $\varphi = 0.353$ . The thick black and red lines in these figures denote the locations of internal casing wall and outlet edge of the casing, respectively (see Figure 3.1). . . . .	50
3.20	Instantaneous velocity vectors and contours of the instantaneous vorticity in the direction normal to the PIV planes for $\varphi = 0.366$ . The grey area at the location of ① indicates the shadow caused by the blade. The thick black and red lines in these figures denote the locations of internal casing wall and outlet edge of the casing, respectively (see Figure 3.1). . . . .	51
3.21	Instantaneous velocity vectors and contours of the instantaneous vorticity in the direction normal to the PIV planes for $\varphi = 0.366$ . The thick black and red lines in these figures denote the locations of internal casing wall and outlet edge of the casing, respectively (see Figure 3.1). . . . .	52
3.22	Instantaneous velocity vectors and contours of the instantaneous vorticity in the direction normal to the PIV planes for $\varphi = 0.366$ . The thick black and red lines in these figures denote the locations of internal casing wall and outlet edge of the casing, respectively (see Figure 3.1). . . . .	53
3.23	Contours of the phase-averaged vorticity in the direction normal to the PIV planes, together with the phase-averaged velocity vectors for $\varphi = 0.366$ . The grey area at the location of ① indicates the shadow caused by the blade. The thick black and red lines in these figures denote the locations of internal casing wall and outlet edge of the casing, respectively (see Figure 3.1). . . . .	54

3.24	Contours of the phase-averaged vorticity in the direction normal to the PIV planes, together with the phase-averaged velocity vectors for $\varphi = 0.366$ . The thick black and red lines in these figures denote the locations of internal casing wall and outlet edge of the casing, respectively (see Figure 3.1). . . . .	55
3.25	Contours of the phase-averaged vorticity in the direction normal to the PIV planes, together with the phase-averaged velocity vectors for $\varphi = 0.366$ . The thick black and red lines in these figures denote the locations of internal casing wall and outlet edge of the casing, respectively (see Figure 3.1). . . . .	56
3.26	Magnified view of Figure 3.15 at ③: (a) instantaneous velocity vectors and contours of the instantaneous vorticity in the direction normal to the PIV plane; (b) contours of the 2D turbulent kinetic energy. In (a), A denotes an approximate region where the mean flow encounters the TLV. . . . .	57
3.27	Contours of the 2D turbulent kinetic energy and phase-averaged velocity vectors on the PIV planes for $\varphi = 0.231$ . The number on the top of each figure denotes the measurement location shown in Figure 3.31. . . . .	58
3.28	Contours of the 2D turbulent kinetic energy and phase-averaged velocity vectors on the PIV planes for $\varphi = 0.276$ . The number on the top of each figure denotes the measurement location shown in Figure 3.31. . . . .	59
3.29	Contours of the 2D turbulent kinetic energy and phase-averaged velocity vectors on the PIV planes for $\varphi = 0.276$ . The number on the top of each figure denotes the measurement location shown in Figure 3.31. . . . .	60

3.30	Contours of the 2D turbulent kinetic energy and phase-averaged velocity vectors on the PIV planes for $\varphi = 0.353$ . The number on the top of each figure denotes the measurement location shown in Figure 3.31. . . . .	61
3.31	Contours of the 2D turbulent kinetic energy and phase-averaged velocity vectors on the PIV planes for $\varphi = 0.353$ . The number on the top of each figure denotes the measurement location shown in Figure 3.31. . . . .	62
3.32	Contours of the 2D turbulent kinetic energy and phase-averaged velocity vectors on the PIV planes for $\varphi = 0.366$ . The number on the top of each figure denotes the measurement location shown in Figure 3.31. . . . .	63
3.33	Contours of the 2D turbulent kinetic energy and phase-averaged velocity vectors on the PIV planes for $\varphi = 0.366$ . The number on the top of each figure denotes the measurement location shown in Figure 3.31. . . . .	64
3.34	Contour of the 2D turbulent kinetic energy from re-centered data of the PIV plane at for $\varphi = 0.353$ . A solid circle in this figure denotes the location of the phase-averaged TLV center. . . . .	65
3.35	Locations of the phase-averaged TLV center in the axial direction for three flow rates. Here, $x$ is the axial position from the blade LE. . . . .	66
3.36	Scatter plot of the location of the TLV center for $\varphi = 0.276$ . These scatter plots are obtained from 950 – 1,000 instantaneous flow fields. The number on the top of each figure denotes the measurement location shown in Figure 3.31. . . . .	67

3.37	Scatter plot of the location of the TLV center for $\varphi = 0.353$ . These scatter plots are obtained from 950 – 1,000 instantaneous flow fields. The number on the top of each figure denotes the measurement location shown in Figure 3.31. . . . .	68
3.38	Scatter plot of the location of the TLV center for $\varphi = 0.353$ . These scatter plots are obtained from 950 – 1,000 instantaneous flow fields. The number on the top of each figure denotes the measurement location shown in Figure 3.31. . . . .	69
3.39	Scatter plot of the location of the TLV center for $\varphi = 0.366$ . These scatter plots are obtained from 950 – 1,000 instantaneous flow fields. The number on the top of each figure denotes the measurement location shown in Figure 3.31. . . . .	70
3.40	Scatter plot of the location of the TLV center for $\varphi = 0.366$ . These scatter plots are obtained from 950– 1,000 instantaneous flow fields. The number on the top of each figure denotes the measurement location shown in Figure 3.31. . . . .	71
3.41	Contours of the phase-averaged axial vorticity, together with the phase-averaged velocity at $x/R_{tip} = 0.05$ for $\varphi = 0.353$ . The gray area indicates where PIV is not performed due to excessive exposure by laser light reflected from the blade. . . . .	72
3.42	Contours of the 2D turbulent kinetic energy and phase-averaged velocity vectors on the $r - \vartheta$ PIV plane at $x/R_{tip} = 0.05$ for $\varphi =$ 0.353. The gray area indicates where PIV is not performed due to excessive exposure by laser light reflected from the blade. . .	73



3.43	Instantaneous velocity vectors and contours of the instantaneous axial vorticity at $x/R_{tip} = 0.05$ for $\varphi = 0.353$ . The gray area indicates where PIV is not performed due to excessive exposure by laser light reflected from the blade. . . . .	74
3.44	Contours of the phase-averaged axial vorticity, together with the phase-averaged velocity at various positions for $\varphi = 0.353$ : (a) $x/R_{tip} = 0.05$ ; (b) $x/R_{tip} = 0.25$ ; (c) $x/R_{tip} = 0.45$ . The gray area indicates where PIV is not performed due to excessive exposure by laser light reflected from the blade. . . . .	75
3.45	Contours of the phase-averaged axial vorticity, together with the phase-averaged velocity at various positions for $\varphi = 0.276$ : (a) $x/R_{tip} = 0.05$ ; (b) $x/R_{tip} = 0.25$ ; (c) $x/R_{tip} = 0.45$ . The gray area indicates where PIV is not performed due to excessive exposure by laser light reflected from the blade. . . . .	76
3.46	Contours of the 2D turbulent kinetic energy and phase-averaged velocity vectors on the $r - \vartheta$ PIV plane at various positions for $\varphi = 0.353$ : (a) $x/R_{tip} = 0.05$ ; (b) $x/R_{tip} = 0.25$ ; (c) $x/R_{tip} = 0.45$ . The gray area indicates where PIV is not performed due to excessive exposure by laser light reflected from the blade. . . .	77
3.47	Contours of the 2D turbulent kinetic energy and phase-averaged velocity vectors on the $r - \vartheta$ PIV plane at various positions for $\varphi = 0.276$ : (a) $x/R_{tip} = 0.05$ ; (b) $x/R_{tip} = 0.25$ ; (c) $x/R_{tip} = 0.45$ . The gray area indicates where PIV is not performed due to excessive exposure by laser light reflected from the blade. . . .	78

3.48	Contours of the phase-averaged circumferential vorticity and phase-averaged velocity vectors on the $x-r$ PIV plane at various phases for $\varphi = 0.353$ . The gray area indicates where PIV is not performed due to excessive exposure by laser light reflected from the blade. . . . .	79
3.49	Contours of the phase-averaged circumferential vorticity and phase-averaged velocity vectors on the $x-r$ PIV plane at various phases for $\varphi = 0.276$ . The gray area indicates where PIV is not performed due to excessive exposure by laser light reflected from the blade. . . . .	80
3.50	The phase-averaged axial velocity profiles for various phase and unconditionally averaged axial velocity profile at $x/R_{tip} = 0.05$ for $\varphi = 0.353$ . . . . .	81
3.51	The phase-averaged axial velocity profiles for various phase and unconditionally averaged axial velocity profile at $x/R_{tip} = 0.05$ for $\varphi = 0.276$ . . . . .	82
3.52	Contours of the phase-averaged circumferential vorticity and the phase-averaged velocity vectors for $\varphi = 0.353$ with $x-r'$ PIV planes. . . . .	83
3.53	The phase-averaged and instantaneous vorticity in the direction normal to the PIV planes, together with velocity vectors at $r/R_{tip} = 0.95$ for $\varphi = 0.353$ . . . . .	84
3.54	Contours of the phase-averaged vorticity in the direction normal to the PIV planes, together with the phase-averaged velocity vectors for $\varphi = 0.353$ . . . . .	85

3.55	Contours of the phase-averaged vorticity in the direction normal to the PIV planes, together with the phase-averaged velocity vectors for $\varphi = 0.276$ . . . . .	86
------	---	----

# List of Tables

## Table

2.1	Specifications of the axial flow fan. . . . .	6
2.2	The locations of velocity and pressure rise measurements. . . . .	7
2.3	The volume flow rates and the total-to-static pressure rise of four flow conditions. . . . .	8
2.4	The normalised-relative uncertainties. . . . .	11
3.1	Radius of the phase-averaged TLV for three flow rates. . . . .	27

# Nomenclature

## Roman Symbols

$A$	width of screen grid
$B$	height of screen grid
$c$	tip chord length
$c_{hub}$	hub chord length
$c_x$	axial tip chord length
$D$	particle displacement
$f$	frequency
$f_{fan}$	rotational frequency
$k_{2D}$	two-dimensional turbulent kinetic energy
$P$	pressure
$P_a$	static pressure at the free outlet
$P_{total}$	total pressure
$Q$	volume flow rate
$Re$	Reynolds number
$R_{duct}$	radius of duct
$R_{hub}$	radius of hub
$R_{tip}$	radius of blade tip
$R_{TLV}$	radius of phase-averaged TLV
$r, \theta$	polar coordinate with the origin at the center of a rotating shaft
$U_{tip}$	blade tip velocity
$u'$	velocity fluctuation

$t$	delay time in chapter 2.4
$T$	delay time between image pairs
$x$	Cartesian coordinate with the origin at the blade leading edge
$y$	Cartesian coordinate with the origin at the inner surface of the duct
$x', r'$	Cartesian coordinate with the origin at the inclined PIV plane
$r_1, r_2$	Cartesian coordinate with the origin at the rotating axis
$w_g$	width of PIV grid

#### Greek Symbols

$\delta_{\Delta D}$	uncertainty in particle displacement
$\delta_e$	particle image diameter
$\delta_g$	displacement gradient
$\delta_m$	uncertainty in magnification
$\delta_N$	particle seeding density
$\delta_t$	laser jitter
$\varepsilon$	uncertainty
$\eta$	efficiency
$\theta$	efficiency
$\lambda_{hub}$	hub pitch angle
$\lambda_{tip}$	tip pitch angle
$\rho$	density
$\varphi$	flow coefficient
$\psi$	pressure coefficient
$\omega$	vorticity
$\Omega$	fan rotation speed

## Superscripts

( $\bar{\quad}$ ) phase averaging

## Abbreviations

BLDC	brushless direct current
CCD	charge-coupled device
FoV	field of view
HWA	hot-wire anemometry
LDV	laser doppler velocimetry
LES	large eddy simulation
Nd-Yag	neodymium-doped yttrium aluminum garnet
PDF	probable density function
PIV	particle image velocimetry
<i>power</i>	motor input power
PS	pressure side
RANS	Reynolds-averaged Navier-Stokes equations
SS	suction side
TLF	tip-leakage flow
TLV	tip-leakage vortex
TE	triling edge

# Chapter 1

## Introduction

A tip-leakage flow (TLF) occurs due to the difference between the pressures on the pressure and suction sides (PS and SS, respectively) of rotating blades (Lakshminarayana, 1996). A tip-leakage vortex (TLV) generated by the roll-up of the TLF has various adverse effects on axial turbomachines (Figure 1.1). The TLV interferes with the main flow in the passage, thereby reducing the efficiency (Inoue, *et al.*, 1986; Denton, 1993; Khalid *et al.*, 1999). Also, strong fluctuations of the TLV act as a major cause of the rotor vibration and generated the rotational instability (Mailach *et al.*, 2001). Furthermore, before it reaches the pressure side of the next blade, the TLV breaks up owing to a high adverse pressure gradient formed there, and the turbulent fluctuations are amplified by segmented vortex filaments (Wu *et al.*, 2011; Miorini *et al.*, 2012; Wu *et al.*, 2012). On the other hand, in axial flow fans operating under low pressures and high flow rates for cooling and ventilation, the detrimental effects of the TLV on the noise and efficiency have been studied (Corsini, *et al.*, 2007; Akturk & Camci, 2014; Kim *et al.*, 2014; Wang *et al.*, 2014; Heo, *et al.*, 2015; Jung & Joo, 2018). Because of increasing demands for low-noise and high-efficiency fan, understanding the TLV characteristics becomes essential, and thus numerical and experimental studies have been conducted extensively. Fukano & Jang (2004) measured the velocity fields near the blade tip in an axial flow fan using a rotating hot-wire anemometry (HWA), and showed that the tip clearance noise



consists of the discrete and broadband noise due to the velocity fluctuation in the blade passage. Jang *et al.* (2016) investigated the TLV trajectories for different flow rates using HWA, and found that, with increasing flow rate, the onset of TLV is delayed in downstream and the trajectory of the TLV tilts to the blade rotation axis. Liu *et al.* (2012) investigated the effect of the fan casing on the fan performance and flow field by measuring the velocity fields downstream of the fan blade using HWA. They showed that both the strength of the TLF and the fluctuation of the TLV increase for the case of a half casing (no casing at the front part). Cai *et al.* (2002) measured the flow field in the blade passage of an open axial fan with a two-dimensional (2D) laser Doppler velocimetry (LDV) and identified the onset location of tip vortex near the blade leading edge and the TLV trajectory in the blade passage. Myung & Baek (1999) measured the flow fields at the  $0.18R_{tip}$  downstream location from the trailing edge of a forward-swept axial flow fan at three different flow rates using a three-dimensional (3D) LDV. They showed the variations of the leakage flow, leakage vortex, hub vortex, and blade wake with respect to the flow rate, and they reported that at the peak efficiency condition the TLV interacts with the pressure surface of the next blade, directly affecting the wake behind its trailing edge. Lee *et al.* (2003, 2005) suggested that an anisotropic turbulence model such as the Reynolds stress model is required for RANS to predict the anisotropic nature of turbulent flow inside the TLV. Furthermore, they showed that the vorticity magnitude of the TLV rapidly decays with decreasing flow rate due to thick casing boundary layer and mixing between the main and leakage flows. Jang *et al.* (2011a, b) investigated vortical structures in an axial flow fan with a partial casing using LDV and large eddy simulation (LES). They identified 3D vortical structures such as the leading-edge separation vortex, tip vortex, and tip-leakage vortex near the blade tip, and found that the vortex

breakup plays a major role in the unsteadiness of the vortical structures. So far, most PIV studies of investigating the TLV structure have focused on the axial compressor and pump (Wu *et al.*, 2011; Miorini *et al.*, 2012; Wu *et al.*, 2012; Wang *et al.*, 2014; Heo, *et al.*, 2015; Jung & Joo, 2018; Oweis & Ceccio, 2005; Yu & Liu, 2007; Hah, *et al.*, 2015; Zhang *et al.*, 2015; Li *et al.*, 2017), but only very limited studies are available for axial flow fans because their blades are highly skewed and occupy large dimensions (Jin, *et al.*, 2011; Fike, *et al.*, 2014). Jin *et al.* (2011) investigated the TLV instability of forward- and backward-skewed fans at a peak pressure condition by measuring flow fields of the blade passage using PIV and pressure fluctuations on the casing wall using pressure sensors. For the forward-skewed blade, the interaction between the TLV and main flow was weaker than that for the backward-skewed blade, and thus the forward-skewed blade is found to be more effective in controlling TLF. Fike *et al.* (2014) used a PIV to investigate flow separation on axial fan blades at stall condition. However, in most of the axial flow fan studies, flow fields inside the blade passage (Nashimoto *et al.*, 2008) or downstream (Lee *et al.*, 2001, 2003; Nashimoto *et al.*, 2004; Paik *et al.*, 2010) of the axial fan (but without casing) have been measured. Therefore, the evolution of the TLV inside the passage of an axial flow fan (with casing) for various flow rates is still not fully understood. Therefore, in the present study, a fan test facility is designed to perform PIV measurements in a forward-swept axial flow fan, and the fan performance parameters are measured. We analyze the evolution of TLV within the passage from the instantaneous and phase-averaged flow fields for various flow rates. Especially, wandering motion of the TLV and its contribution to turbulent flow field are investigated. In Chapter 2, the experimental setup is explained. The characteristics of TLV and its evolution are presented in Chapter 3, followed by conclusions in Chapter 4.

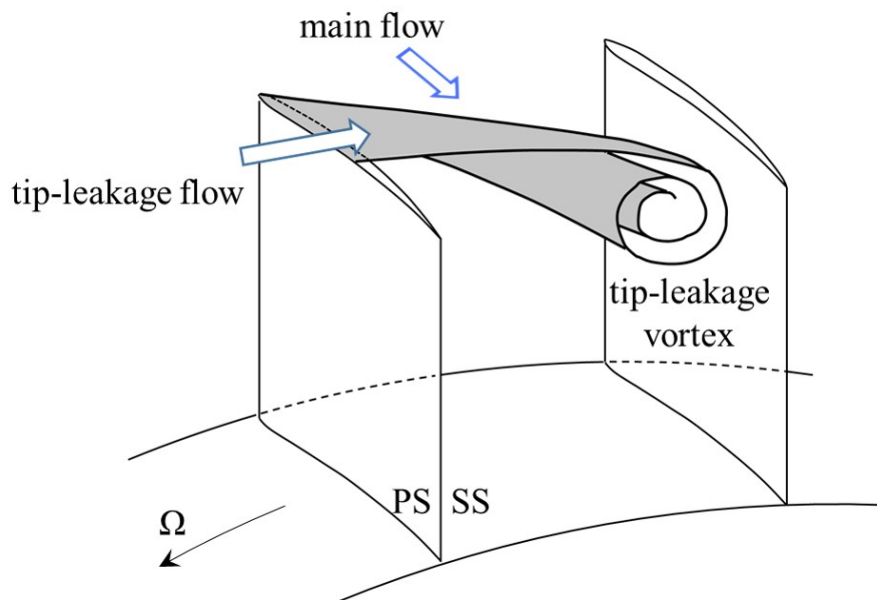


Figure 1.1. Schematic diagram of tip-leakage flow and tip-leakage vortex in axial compressor blades (modified from Fischer *et al.* (2012)).

## Chapter 2

### Experimental Set-up

To investigate the tip-leakage flow in an axial flow fan at various flow rates, an axial flow fan system is constructed. The flow rates and pressure rise are directly measured using a pitot tube and a manometer to measure the performance of the axial flow fan. The flow field around the fan blades is obtained using digital particle image velocimetry (DPIV). Sec. 2.1 describes the axial fan used in this study. The experimental set-up for measuring the performance of axial flow fan according to flow rates is described in Sec. 2.2. Detailed descriptions of the fan performance and the DPIV system are followed in Sec. 2.3 and Sec. 2.4, respectively.

#### 2.1 Axial flow fan model

In the present study, a forward-swept axial fan with a casing which is attached to an outdoor unit of an air conditioner for cooling (Figure 2.1) is investigated. The present fan is a forward-swept axial flow fan and has a low hub-to-tip ratio ( $R_{hub}/R_{tip} = 0.311$ ) as shown in Figure 2.2, where  $R_{hub}$  and  $R_{tip}$  are the radii of hub and blade tip, respectively. The Reynolds number is  $Re = 547,000$  based on the blade tip radius and tip velocity ( $U_{tip} = R_{tip}\Omega$ ), where  $\Omega$  is the fan rotational speed. The fan specifications are provided in Table 2.1.

Number of blades	4
Blade tip radius, $R_{tip}$	280 mm
Rotational speed, $\Omega$	1,000 rpm
Axial tip chord length, $c_x/R_{tip}$	0.8
Tip chord length, $c/R_{tip}$	1.439
Hub chord length, $c_{hub}/R_{tip}$	0.521
Tip pitch angle, $\lambda_{tip}$	$58^\circ$
Hub pitch angle, $\lambda_{hub}$	$45^\circ$
Tip gap, $t_{gap}/R_{tip}$	0.036
Hub-to-tip ratio, $R_{hub}/R_{tip}$	0.311
Solidity at the tip	0.917

Table 2.1. Specifications of the axial flow fan.

## 2.2 Axial flow fan test system

The experimental facility to measure the performance of the fan is shown in Figure 2.3. The fan casing and upstream duct have the same inner diameter of 580 mm, and the gap between the casing and the blade tip is 10 mm ( $\approx 0.036R_{tip}$ ). The screens with open areas of 56 % and 71 % are located upstream of the duct to adjust the flow rates from 1.67 to 2.65  $m^3/s$  (Figure 2.4). A brushless DC (BLDC) motor, which controls the rotational speed with 0.1 % accuracy through an inverter drive (A1000, Yaskawa), is directly connected to the fan. The fan rotates at 1,000 rpm at all flow conditions. The axial location of the blade trailing edge (TE) coincides with that of the casing outlet. The fan casing has a transparent curved window for PIV measurements.

### 2.3 The fan performance

The velocity at 600 mm upstream location from the blade leading edge (LE) is measured at ten radial locations (and at four azimuthal angles with 90 degree intervals for each radial location, see Table 2.2) by positioning a pitot tube through a traversing unit (Figure 2.5). The ten radial locations are chosen such that the ten annuli have the same cross-sectional area.

Measuring pts.	$r/R_{duct}$	$y/R_{duct}$
1	0	1.00
2	0.32	0.78
3	0.45	0.61
4	0.55	0.50
5	0.63	0.41
6	0.71	0.33
7	0.77	0.26
8	0.84	0.19
9	0.89	0.13
10	0.95	0.08
11	1.00	0.03

Table 2.2. The locations of velocity and pressure rise measurements.

The measured deviations of the dynamic and total pressures from their mean values are only 1.2 % and 2.0 %, respectively, at each radial location. The flow rates are calculated by integrating the velocities measured at ten radial locations using a modified log-linear method (Hansen, *et al.*, 2016). The total-to-static pressure rise ( $\Delta P$ ) is defined as  $\Delta P = P_a - P_{total}$ , where  $P_{total}$  is the (negative)

	Condition 1	Condition 2	Condition 3	Condition 4
Combination of screens	4 x screen1	2 x screen1 1 x screen2	1 x screen1	1 x screen2
Volume flow rates (m <sup>3</sup> /s)	1.67	2.00	2.55	2.65
$\Delta P$ (Pa)	110	93	48	34

Table 2.3. The volume flow rates and the total-to-static pressure rise of four flow conditions.

total pressure measured at the upstream of the fan and  $P_a$  is the static pressure at the free outlet (zero-gauge pressure). Flow rates and pressures are measured under four conditions using a combination of screens (Table 2.3).

The aerodynamic performances of the present fan are shown in Figure 2.10. Here, the flow coefficient ( $\varphi$ ), pressure coefficient ( $\psi$ ), and efficiency ( $\eta$ ) are defined as

$$\varphi = \frac{Q}{\pi R_{tip}^2 U_{tip}}, \quad \psi = \frac{2\Delta P}{\rho U_{tip}^2}, \quad \eta = \frac{\Delta P Q}{power(W)} \quad (2.1)$$

where  $Q$  is the volume flow rate,  $\Delta P$  is the total-to-static pressure rise, and  $power(W)$  denotes the motor input power. The motor input power was obtained by measuring the power consumption of the motor using a power analyzer (WT500, Yokogawa). The aerodynamic performances are measured for four different flow rates ( $\varphi = 0.231, 0.276, 0.353,$  and  $0.366$ ). The maximum efficiency is obtained at  $\varphi = 0.276$ . According to the method in Coleman and Steele (2009), the uncertainties of the flow and pressure coefficients and effi-

ciency are less than 3.3 %, 1.6 %, and 2.8 %, respectively.

## 2.4 Digital particle image velocimetry

The velocity field within the blade passage and the velocity field of blade wake are measured using a digital particle image velocimetry (PIV). An infrared photo-sensor detects a tiny hole located on a disc rotating together with the fan blades through a shaft (see Figure 2.3), and delivers a signal to a frequency divider (SN74LS29, Texas instruments). The frequency divider picks up every fourth signals at the frequency of  $f = 0.25f_{fan}$  (4.167 Hz) and delivers it to a timing hub (XS-TH, IDT) which simultaneously triggers the laser and camera for PIV measurements at a specific phase of rotation (Figure 2.11 (a)). To acquire images every 10 degrees in the azimuthal direction (Figure 2.12), a delay time ( $\Delta t = 1.667$  ms) is added to the output signal of the frequency divider using a timing hub. For the blade passage flow measurement, the laser sheet is not parallel to the axis of rotation. Due to the highly skewed blades, PIV is conducted on planes perpendicular to a chord line at the radial location of 90 % of blade span (Figure 2.12 (a)). A laser sheet is inclined by 33.5 degrees from the centerline. To illuminate the inclined planes, the light sheet optics (Dantec dynamics) consisting of the light sheet module, multi light angle modules, and mirror arm was installed in the downstream of the blade (Figure 2.12 (b)). An Nd-Yag laser system (Bernoulli PIV 200-15, Litron) with 512 nm wavelength and 200 mJ maximum power was used as the light source, and particle images are acquired by a CCD camera (Vieworks, VH-4MC). A thickness of a laser sheet generated by the laser optics is about 2 mm. To measure the velocity field of the wake of the blade, the PIV is performed by transferring the laser optics and the CCD camera through the traversing units. The field of view of



the camera with a 105 mm lens measured using calibration target (consisting of black dots of 1 mm diameter and 5 mm spacing) is  $139.9 \times 139.9$  mm at the blade passage and  $150.0 \times 150.0$  mm at the blade wake. The size differences of the camera field of view in the vertical and horizontal directions are less than 0.24 %. The particles whose average size is  $1 \mu\text{m}$  were generated by a fog generator (F2010, Safex) and are uniformly sprayed over the entire experimental space such that the interrogation window of PIV correlation process has at least 20 particles. The particle image pairs are filmed at a rate of 4.16 per second and the exposure delay time between the pair is 7-10  $\mu\text{s}$ . Total 1,000 pairs of images are averaged at each rotation phase for the phase-averaged flow fields. The velocity field is calculated by the cross-correlation process based on the fast-Fourier transform algorithm with an initial window size of pixels and a final interrogation window size of pixels. The interrogation window is overlapped by 50 %, leading to spatial resolution of about 1.12 mm ( $0.004R_{tip}$ ) for the blade passage measurement and about 1.2 mm ( $0.0043R_{tip}$ ) for the blade wake measurement. The uncertainty is determined by errors from the hardware in the PIV system and the correlation process (Raffel *et al.*, 2007). The overall uncertainty,  $\varepsilon_u$ , for a given image pair is determined by combining the relative uncertainties as

$$\varepsilon_u = \sqrt{\left(\frac{\delta_t}{\Delta T}\right)^2 + \left(\frac{\delta_e}{\Delta D}\right)^2 + \left(\frac{\delta_{\Delta D}}{\Delta D}\right)^2 + \left(\frac{\delta_N}{\Delta D}\right)^2 + \left(\frac{\delta_m}{w_g}\right)^2 + \left(\frac{\delta_g}{\Delta D}\right)^2} \quad (2.2)$$

where  $\delta_t$  is laser jitter,  $\delta_e$  is particle image diameter,  $\delta_{\Delta D}$  is uncertainty in particle displacement,  $\delta_N$  is seeding density,  $\delta_m$  is magnification, and  $\delta_g$  is displacement gradient, respectively (Hansen, *et al.*, 2016). The relative uncertainties related to laser jitter and magnification are normalised by the time delay between image pairs,  $\Delta T$ , and the grid width,  $w_g$ , respectively, and the other relative uncertainties are normalised by the particle displacement,  $\Delta D$ . The relative uncertainties give in Table 2.4. In the present study, the total uncertainty of the instantaneous velocity measurement is 8.72 %.

	Normalized uncertainty	Reference
$\frac{\delta_t}{\Delta T}$	0.01	Manufacturer's specifications
$\frac{\delta_e}{\Delta D}$	0.03	Raffel <i>et al.</i> (2006)
$\frac{\delta_{\Delta D}}{\Delta D}$	0.04	Willert & Gharib (1991)
$\frac{\delta_N}{\Delta D}$	0.01	Raffel <i>et al.</i> (2006)
$\frac{\delta_m}{w_g}$	0.01	Hansen <i>et al.</i> (2016)
$\frac{\delta_g}{\Delta D}$	0.07	Hansen <i>et al.</i> (2016)

Table 2.4. The normalized-relative uncertainties.

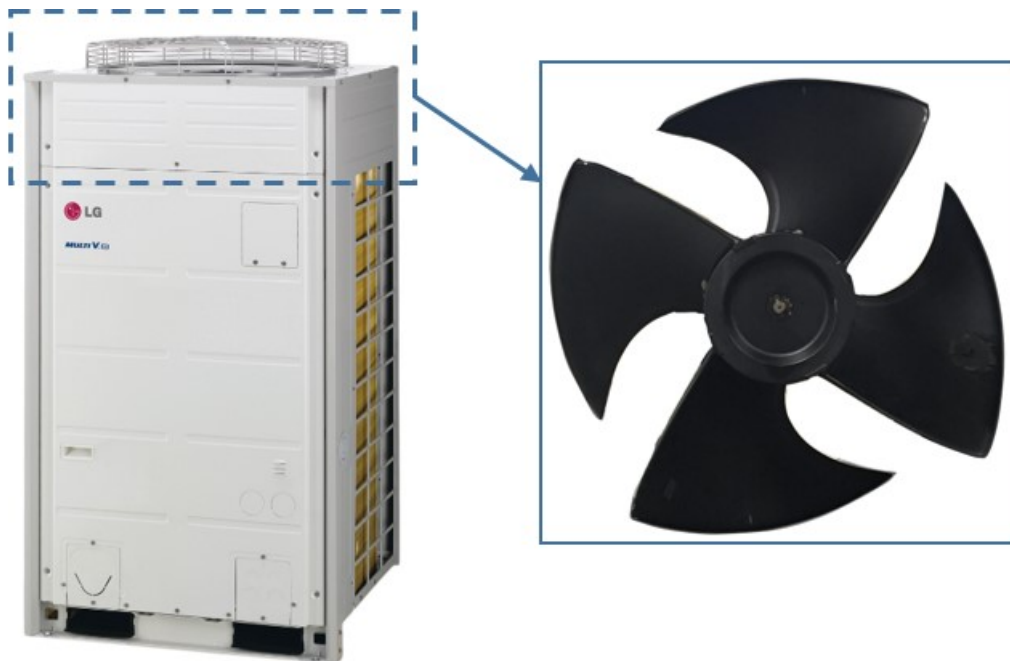


Figure 2.1. A outdoor unit of an air conditioner and an axial flow fan (from <http://www.buildingx.co/home>).

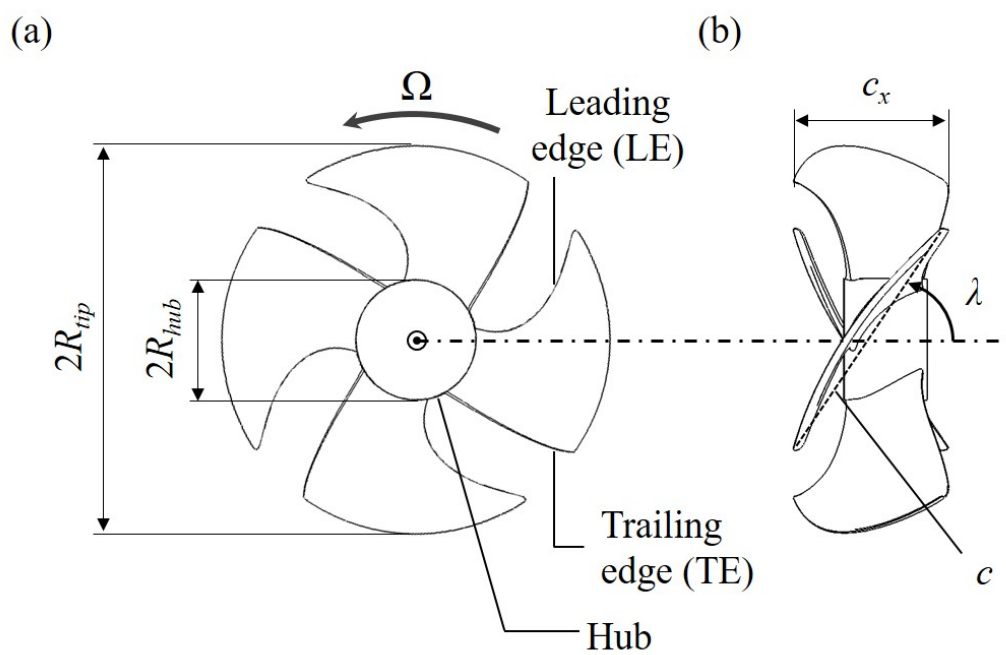


Figure 2.2. Schematic diagram of the axial flow fan: (a) front view; (b) side view.

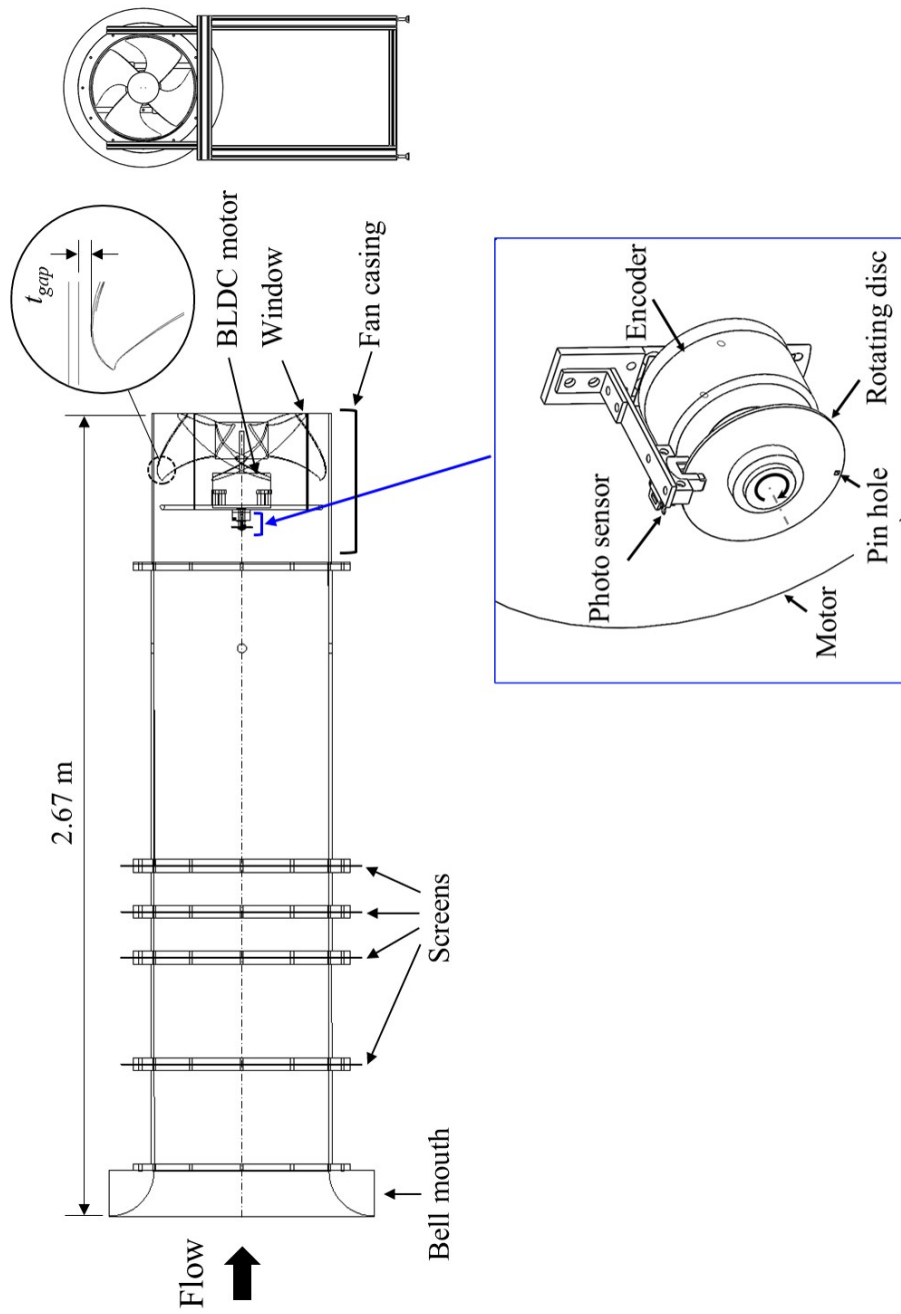
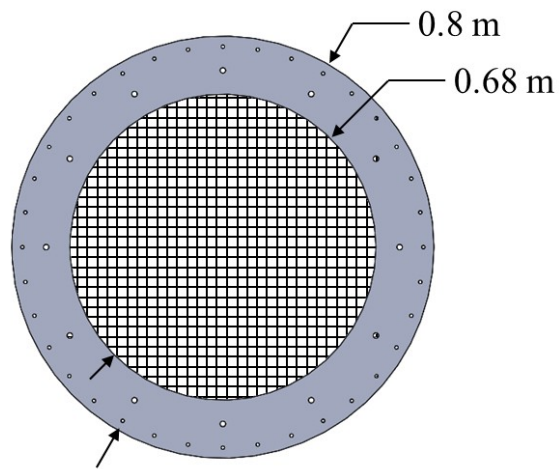
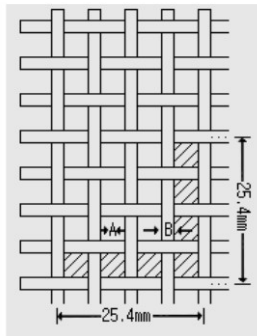


Figure 2.3. Axial flow fan system.

(a)



(b)



<b>Screen1</b>	<b>Screen2</b>
A: 1.19 mm	A: 2.68 mm
B: 0.4 mm	B: 0.5 mm
Open area (%): <b>56</b>	Open area (%): <b>71</b>

Figure 2.4. Schematic diagram of the screen.

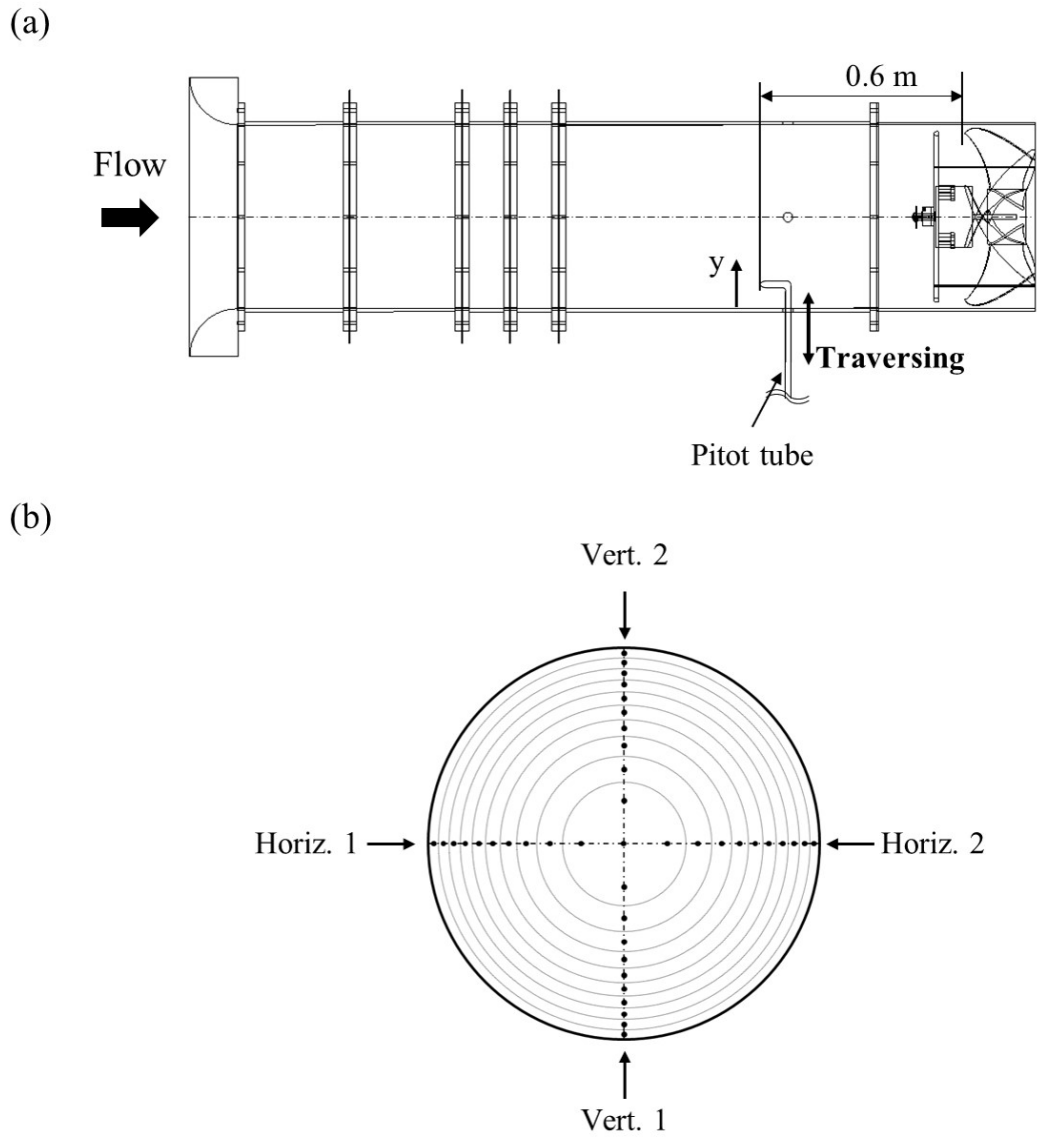


Figure 2.5. The experimental set-up for the velocity and pressure rise measurements: (a) schematic diagram of the pitot tube set-up; (b) the measurement locations of four radial directions.

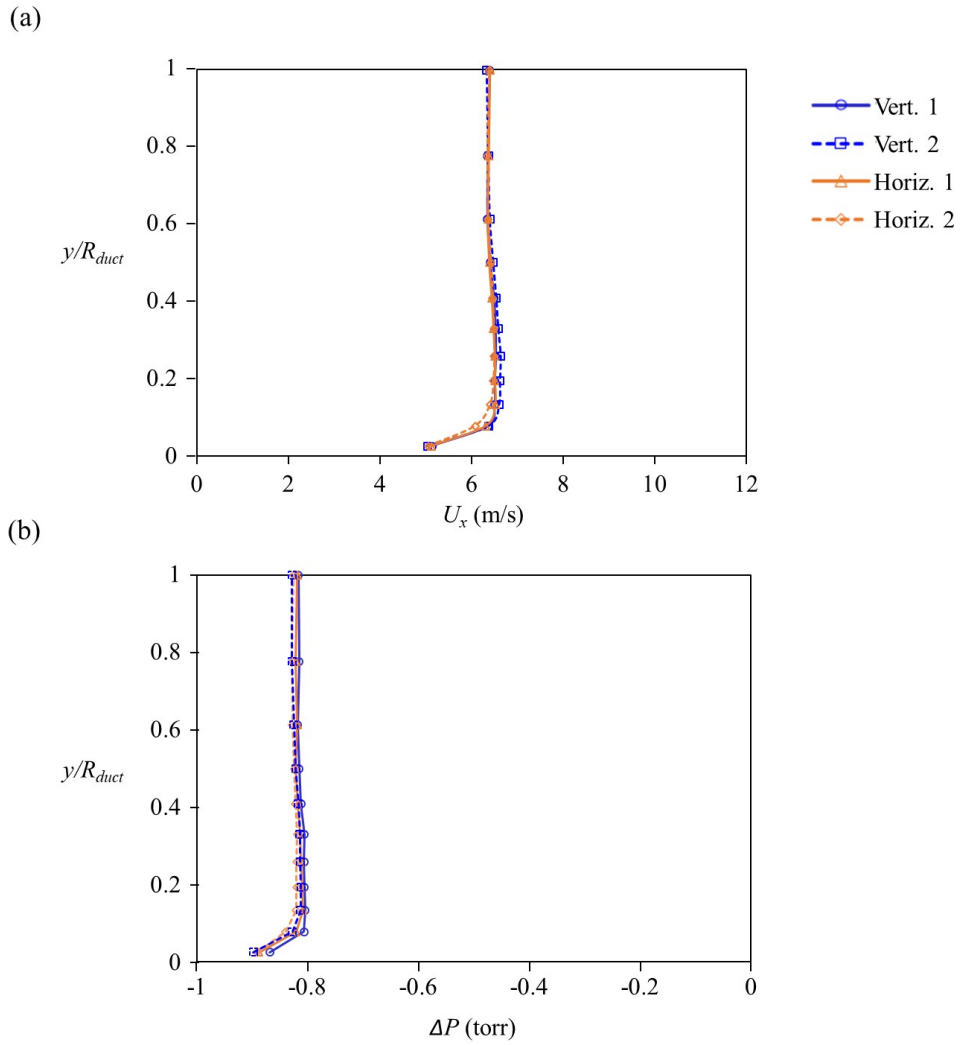


Figure 2.6. Results of the measurement for condition 1 (see Table 2.3): (a) velocity profile for the volume flow rate; (b) static pressure profile for the total-to-static pressure rise.



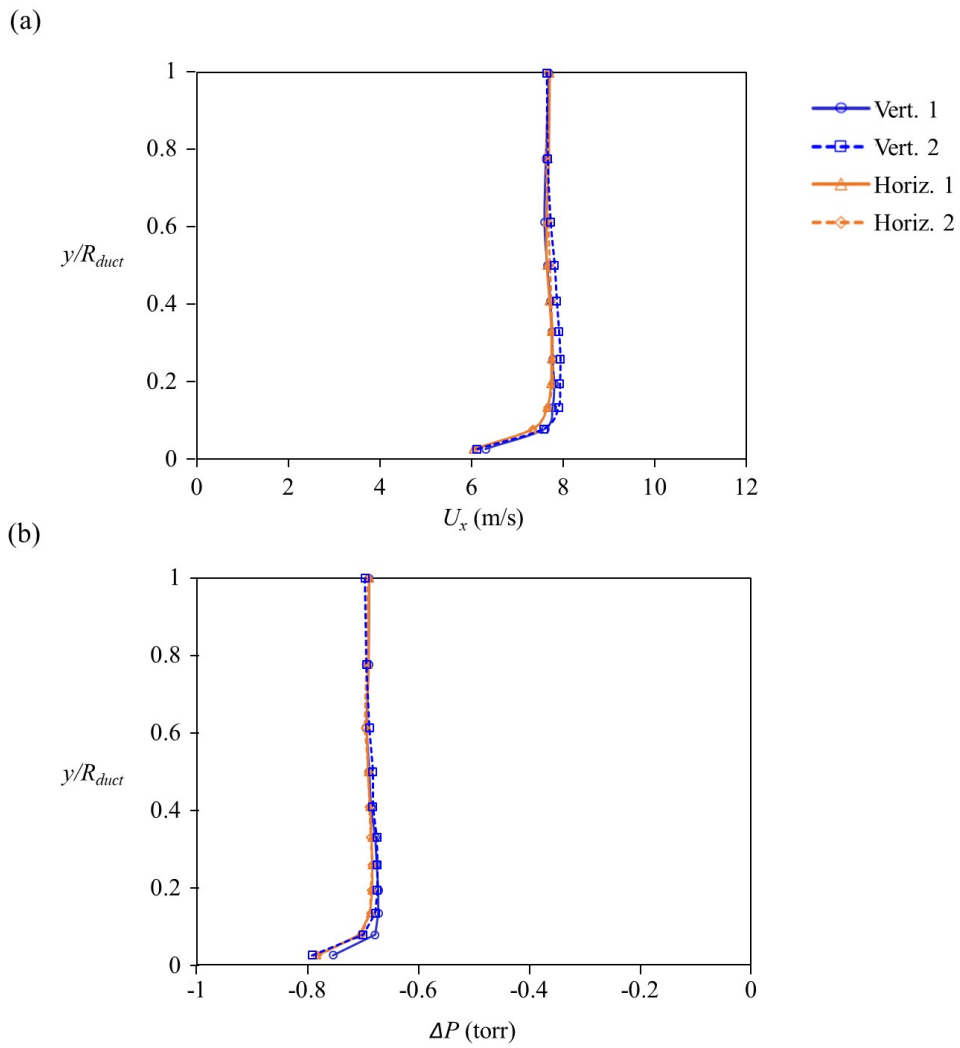


Figure 2.7. Results of the measurement for condition 2 (see Table 2.3): (a) velocity profile for the volume flow rate; (b) static pressure profile for the total-to-static pressure rise.

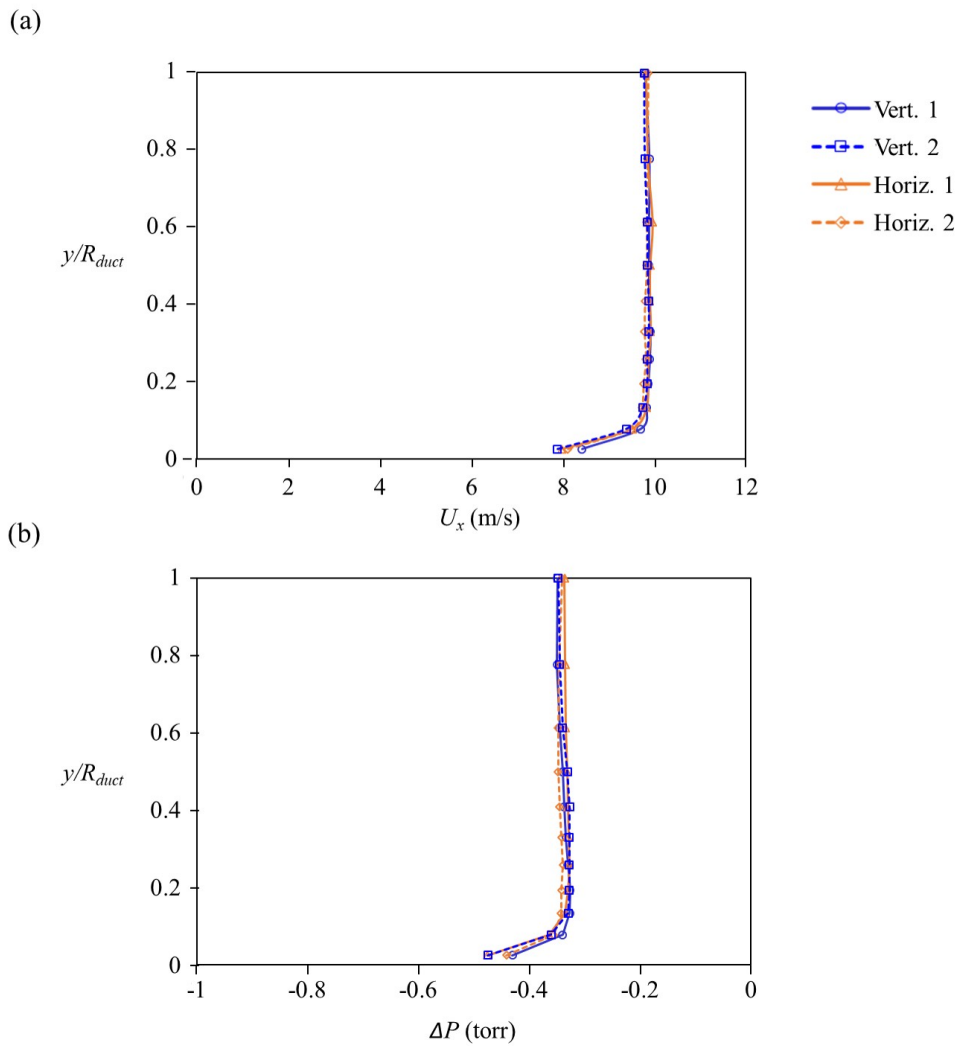


Figure 2.8. Results of the measurement for condition 3 (see Table 2.3): (a) velocity profile for the volume flow rate; (b) static pressure profile for the total-to-static pressure rise.

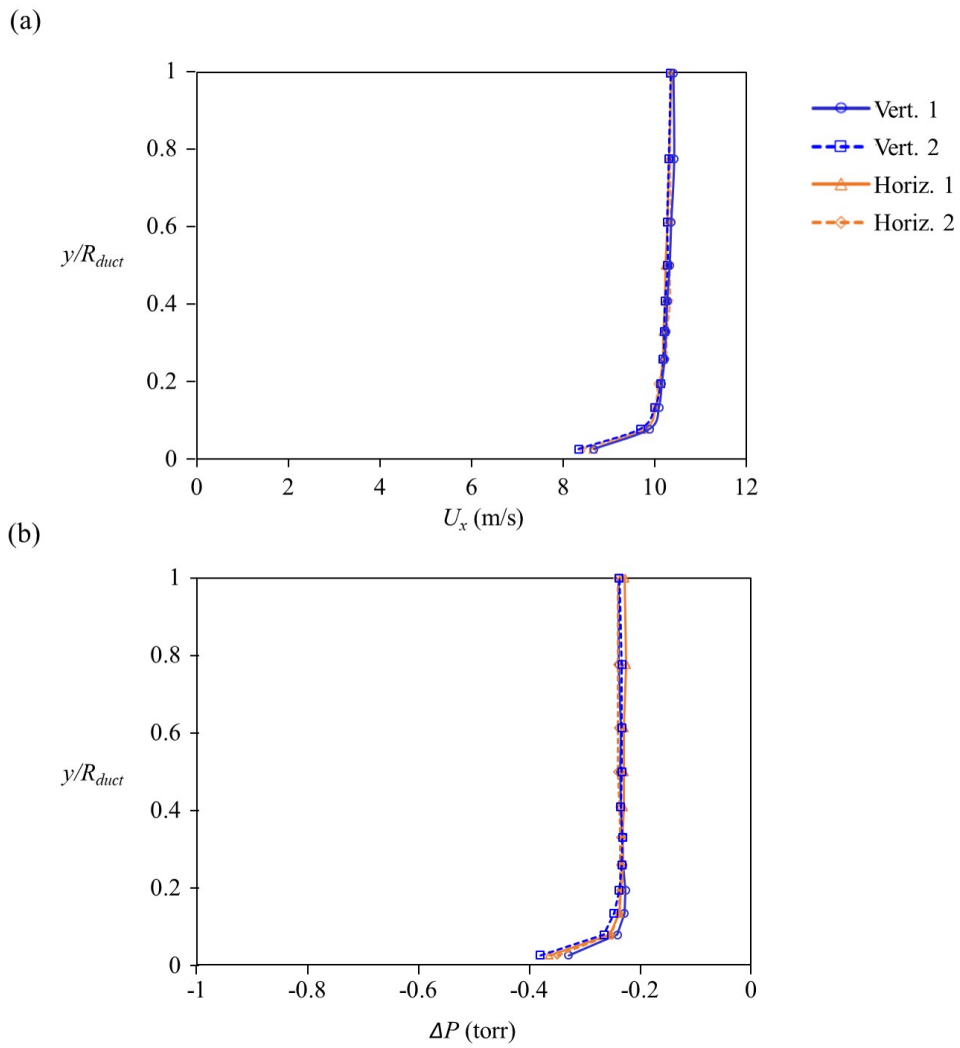


Figure 2.9. Results of the measurement for condition 4 (see Table 2.3): (a) velocity profile for the volume flow rate; (b) static pressure profile for the total-to-static pressure rise.

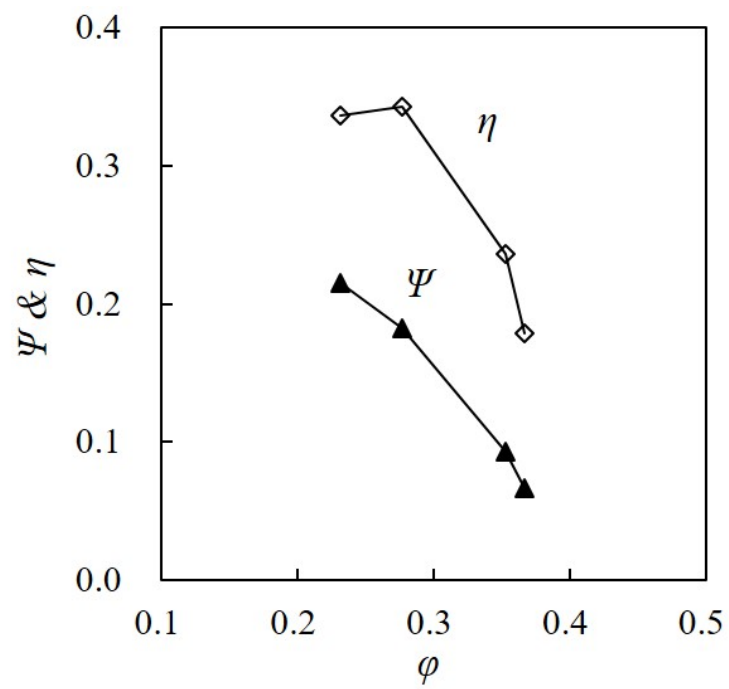


Figure 2.10. Performance curves of the fan: pressure coefficient ( $\psi$ ) and efficiency ( $\eta$ ) versus flow coefficient ( $\phi$ ).

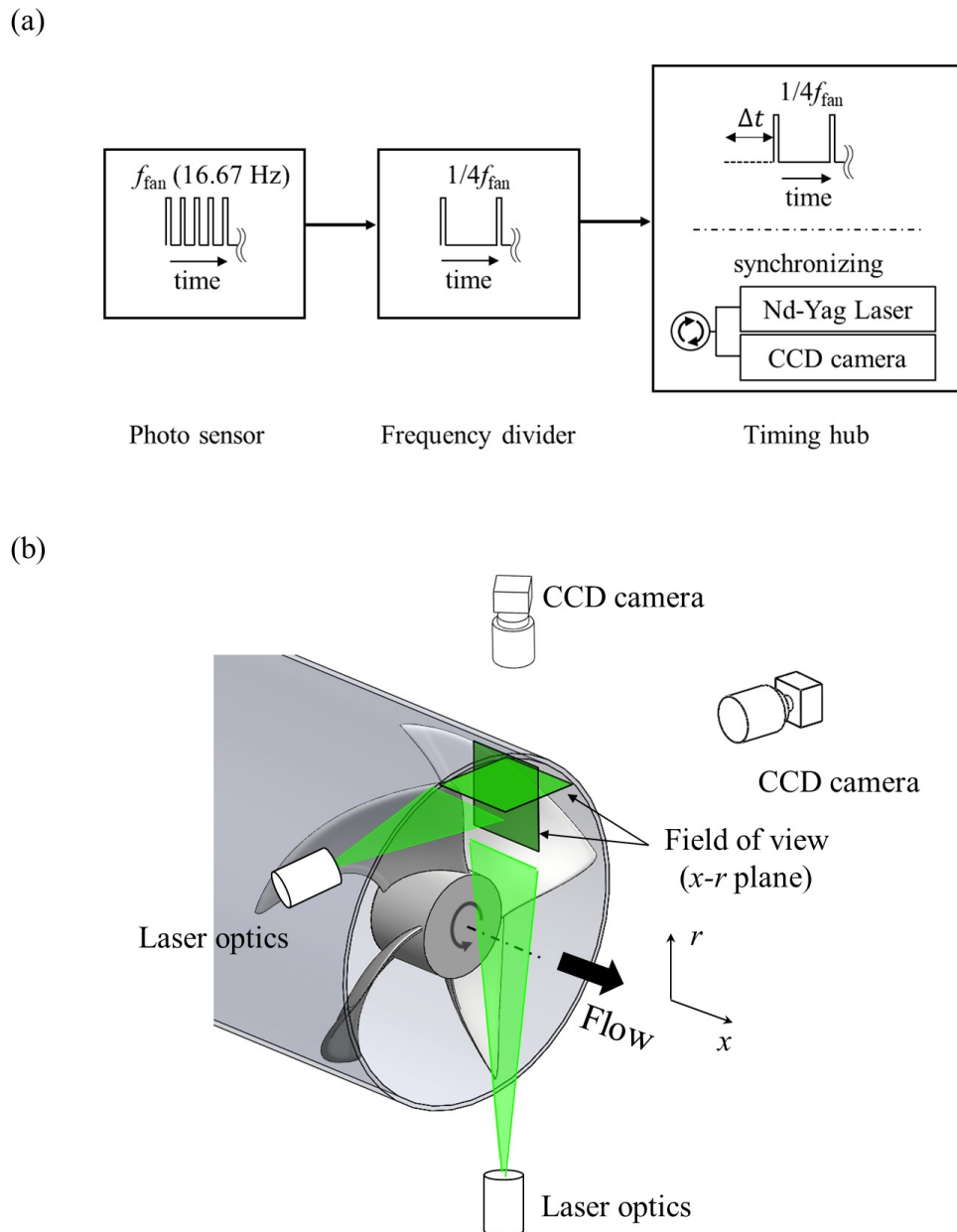


Figure 2.11. Experimental set-up for digital PIV measurements:(a) signal processing for triggering the laser and camera simultaneously; (b) PIV planes for the blade wake. In (a),  $f_{fan}$  is the fan rotating frequency.

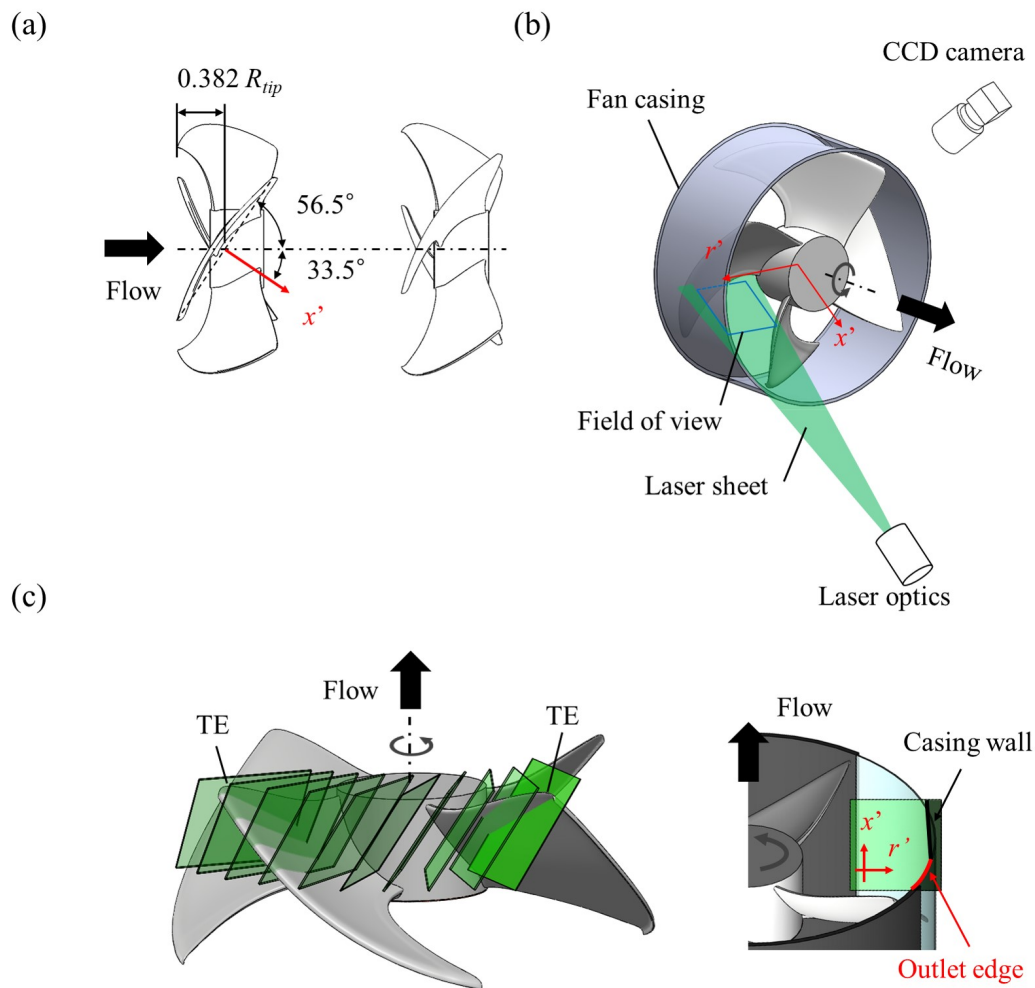


Figure 2.12. Experimental set-up for digital PIV measurements for the blade passage flow:(a) side view; (b) perspective view; (c) PIV planes (green colored planes). In (a), the angle from the centerline to the chord line is  $56.5^\circ$ , and the laser sheet (red arrow) is tilted downward by  $33.5^\circ$  from the centerline.

## Chapter 3

### Results and Discussion

We conducted PIV at four flow conditions ( $\varphi = 0.231, 0.76, 0.353,$  and  $0.366$ ) to measure the velocity field within the blade passage. To obtain particle images at intervals of 10 degrees between the TE of the blade and the TE of the neighboring blade (see Figure 2.12 (c)) according to flow conditions, the blade loading was controlled using the screens. The TLV developed from the TLF is present near the SS of the blade and migrates downstream. In the PIV plane near the TE, shadowing occurs on the SS due to the optical interference of the blades, so the existence of TLV cannot be confirmed (Figure 3.1). Since the laser sheet is not parallel to the axis of rotation, the boundary due to the casing wall is tilted in the flow fields. We also performed PIV in various directions to investigate the flow characteristics of the TLV in the wake (see Figure 2.11 (b)).

#### 3.1 Stall condition of $\varphi = 0.231$

Figure 3.2-3.4 shows the instantaneous flow fields at a few azimuthal PIV planes at different time instants for  $\varphi = 0.231$ . The TLV already broke into small-scale vortices at ① spreads to a wider area from ② to ⑥. As the flow rate decreases (increasing blade loading), the TLV tilts further toward the circumferential direction (Myung & Baek, 1999; Jang, *et al.*, 2005; Lee *et al.*, 2005), and at the stall condition, the vortex breaks up on the PS of neighboring blade

before developing downstream of the TE. Liu *et al.* (2003) reported that the TLV at near stall condition breaks down earlier and interacts more violently with mainstream, which cause large blockage and much loss. The TLV cannot be found in the phase-averaged flow field because there is no distinct TLV in the instantaneous velocity field (Figure 3.5-3.7). Only the TLF is found near the TE and the casing wall at ① and ②.

### 3.2 Peak efficiency condition of $\varphi = 0.276$

At the peak efficiency condition of  $\varphi = 0.276$ , the TLV broken into smaller vortices spreads to an area narrower than that for  $\varphi = 0.231$ , which results in the highest efficiency for  $\varphi = 0.276$  (Figure 3.8-3.10). From ① to ⑤, the debris of the broken TLV moves downstream. Figure 3.11-3.13 shows the phase-averaged flow fields at a few azimuthal PIV planes for  $\varphi = 0.231$ . At the peak efficiency condition, the phase-averaged vortex quickly diffuses away down-stream due to the TLV breakup.

### 3.3 Over flow conditions of $\varphi = 0.353, 0.366$

For  $\varphi = 0.366$  (Figure 3.11-3.13), a strong TLV rotating in the clockwise direction is observed at ① and travels down-stream but losing its strength at ③ and ⑥. For  $\varphi = 0.353$  (Figure 3.17-3.19), a similar phenomenon is observed, but the TLV sometimes breaks up at ⑥. At higher flow rates of  $\varphi = 0.353$  and  $0.366$  (Figure 3.14-3.16 and 3.20-3.21), the TLV migrates downstream, but its strength decays slowly. As the flow rate increases, the TLV locates farther downstream, but its migration speed in the axial direction is almost the same for  $\varphi = 0.353$  and  $0.366$  (see Figure 3.45).



### 3.4 Instantaneous Tip-leakage vortex

To investigate the characteristic strength and size of individual TLV and their effects on turbulence, it is necessary to determine the boundary of instantaneous TLV. We define the TLV center by the instantaneous location of maximum vorticity in the direction normal to the PIV planes (Wu *et al.*, 2012; Yu & Liu, 2007), and the boundary of the phase-averaged TLV based on the locations of the vorticity trough between neighboring peaks, provided that the magnitude of vorticity there is at least  $e^{-1}$  time the level at the vortex center (Wu *et al.*, 2012). If the vorticity drops below this threshold, the threshold defines the vortex boundary. For the peak efficiency condition ( $\varphi = 0.276$ ), the PIV plane at ⑥, the TLV breaks up so the TLV center could not be defined. Corresponding average values for radius at each locations from 990 instantaneous fields are summarized in Table 3.1. The radius of the phase-averaged TLV could not be defined because part of the boundary of the TLV is out of the PIV plane from ① to ④ for  $\varphi = 0.276$ . The size of the TLV increases up to ③ and remains almost the same up to ⑥ for  $\varphi = 0.353$ . For  $\varphi = 0.366$ , the radius of the phase-averaged TLV increases up to ③, maintains its size up to ⑤, and then increases again.

Figure 3.26 shows a magnified view of Figure 3.15 at ③ for  $\varphi = 0.353$ , and the contours of 2D turbulent kinetic energy  $k_{2D}$ , where  $k_{2D} = (\overline{u'_r u'_r} + \overline{u'_x u'_x}) / 2$ , and  $(\overline{\quad})$  and prime denote the phase averaging and fluctuations, respectively (Wu *et al.*, 2011). Along the region of "A", the main flow circles around the TLV and a number of discrete positive vorticity peaks are observed. The 2D turbulent kinetic energy is also high from the center region of TLV to its boundary. On the other hand, the main flow is accelerated on the left of the TLV due to its induced motion as well as the blockage effect, and then the accelerated

PIV plane	$R_{TLV}/R_{tip}$ ( $\varphi = 0.276$ )	$R_{TLV}/R_{tip}$ ( $\varphi = 0.353$ )	$R_{TLV}/R_{tip}$ ( $\varphi = 0.366$ )
①	-	0.038	0.041
②	-	0.048	0.045
③	-	0.050	0.052
④	-	0.048	0.051
⑤	0.067	0.050	0.051
⑥	0.072	0.050	0.056

Table 3.1. Radius of the phase-averaged TLV for three flow rates.

flow follows the rotating direction of the TLV. Consequently, negative vorticity peaks are generated there, as shown in Figure 3.26.

Figure 3.27-3.33 shows the contours of the 2D turbulent kinetic energy ( $k_{2D}$ ) and the phase-averaged velocity vectors on the PIV planes. As shown in this figure and also in instantaneous flow fields (Figure 3.2-3.4, 3.8-3.10, and 3.14-3.16), the mean location of the TLV center is highly correlated with the location of peak  $k_{2D}$ . The main flow area has a very low  $k_{2D}$ , and the area around the TLV and where the small debris of the TLV is present has a relatively high  $k_{2D}$  compared to the main flow. For  $\varphi = 0.231$ , the high  $k_{2D}$  region exists widely because the TLV is broken in all PIV plane. There is also a high  $k_{2D}$  on the blade PS at ① and ② (Figure 3.27). For  $\varphi = 0.276$ , the TLV is already broken at ① and is present as a small debris (Figure 3.8). However, until ④, the vortices is not scattered to a large area (Figure 3.9), and there is a high TKE region. From ④ to ⑥, the debris of the TLV is scattered widely so that the high TKE area gradually widens and the peak  $k_{2D}$  area disappears (Figure 3.28-3.29). For the high flow rates ( $\varphi = 0.353, 0.366$ ), there is a peak TKE

region because the TLV from ① to ⑥ is present without bursting, and it moves downstream together with the TLV as mentioned above (Figure 3.30-3.33).

If a vortex stayed at one position without any oscillation, its center would have zero kinetic energy (see Figure 3.34 in the below). The fact that the TLV center contains high  $k_{2D}$  indicates that the TLV wanders in time (Heyes, *et al.*, 2004). The TLV diffuses while migrating in the azimuthal direction, and thus a region of relatively high  $k_{2D}$  increases down-stream. However, the peak values of  $k_{2D}$  decrease and increase for  $\varphi = 0.276$  and  $0.353$ , respectively, because the TLV breaks up for  $\varphi = 0.276$  but sustains for  $\varphi = 0.353$  (see also Figure 3.8-3.9, 3.16).

As mentioned above, when a vortex stays at one position without any oscillation, the  $k_{2D}$  is zero. To confirm this, we perform an approach similar to what was done for a wandering wingtip vortex by Heyes *et al.* (2004): 1) for each instantaneous flow field obtained by PIV measurements, a TLV is identified, its center is moved to an origin, and neighboring velocity field is stored; 2) the same procedure is conducted for about 1,000 instantaneous flow fields; 3) the resulting flow fields are averaged, and 2D turbulent kinetic energy is obtained. Figure 3.34 shows the contours of the 2D  $k_{2D}$  from this approach at ③ for  $\varphi = 0.353$ . The  $k_{2D}$  at the re-centered TLV center is significantly reduced, and its value is only 20 % of the original  $k_{2D}$  value in Figure 3.30-3.31. With this re-centered data, the  $k_{2D}$  is largest at the upstream location due to the swirl motion of the TLV and its interaction with the main flow. These results together with those in Figure 3.27-3.33 clearly demonstrate that the TLV wanders around its mean center and wandering motion contributes to a large portion of the turbulent kinetic energy at the TLV center.

Figure 3.35 shows the axial position of the phase-averaged TLV center for three flow conditions ( $\varphi = 0.276$ ,  $0.353$ , and  $0.366$ ) as it moves downstream.

Although the in-stantaneous TLV breaks up at all PIV planes for  $\varphi = 0.276$  (see Figure 3.8-3.10), the phase-averaged TLV center can be still defined (see Figure 3.11-3.13). As the flow rate decreases, the TLV locates further upstream. For  $\varphi = 0.353$  and  $0.366$ , the migration speeds of the TLV in the axial direction are almost the same from each other. For the peak efficiency condition of  $\varphi = 0.276$ , the migration speed is faster than those for  $\varphi = 0.353$  and  $0.366$ . This is because the fragmented vortices after the breakup are swept away by the main flow.

The wandering motion of the TLV is commonly observed in compressors (Tan *et al.*, 2015), pumps (Wu *et al.*, 2011), as well as in axial fans (Jin, *et al.*, 2011; Park *et al.*, 2017). To identify the wandering motion, we provide scatter plots of the TLV center at ① - ⑥ for higher flow rates ( $\varphi = 0.353, 0.366$ ) and at ④ - ⑤ for peak efficiency condition ( $\varphi = 0.276$ ) in Figure 3.36-3.37, where the origin  $(0, 0)$  is the mean center location of the TLV. In these figure, each TLV center is defined by the instantaneous location of maximum vorticity in the direction normal to the PIV planes (Wu *et al.*, 2012; Yu & Liu, 2007). Black circles in this figure denote approximate shapes of the TLV, identified by the vorticity magnitude of  $e^{-1}$  times that of the phase-averaged TLV center as mentioned above. For the peak efficiency condition ( $\varphi = 0.276$ ), the fragments of the broken TLV is scattered widely at ④ and ⑤ positions, and the wandering motion of the peak vorticity is considerable. It can be confirmed that the magnitude of the vortex wandering is significantly out of the boundary of the phase-averaged TLV for  $\varphi = 0.276$  (Figure 3.36). For  $\varphi = 0.353$  and  $0.366$ , the mean radius of the phase-averaged TLV at ① - ⑥ are about  $0.05 R_{tip}$ . The TLV center scatters more in the axial direction than in the radial direction. As shown, as the TLV migrates downstream, the area covered by the wandering motion becomes broader. At ③ and ④, this area is even larger than the mean

size of the TLV (Figure 3.37-3.40).

### 3.5 Tip-leakage vortex at the blade wake

In order to investigate the characteristics of the TLV moving after the blade TE, PIV is performed on the  $r - \vartheta$  plane (at  $x/R_{tip} = 0.05, 0.25, \text{ and } 0.45$ ) and the  $x-r$  plane ( $0 < x/R_{tip} < 0.5, 0.7 < r/R_{tip} < 1.18$ ) near the TE for  $\varphi = 0.276$  and  $0.353$ , Respectively (see Figure 2.12). Figure 3.41 shows the phase-averaged axial vorticity and velocity vectors of four  $r - \vartheta$  PIV planes (FoV  $150 \times 150$ ) at  $x/R_{tip} = 0.05$  for  $\varphi = 0.353$ . In this location, the TLV still exists between the blade and the casing wall (blue dashed closed curve) and a blade wake with strong positive vorticity behind the blade TE is observed (red dashed closed curve). Since the wandering of the TLV is still present at  $x/R_{tip} = 0.05$  and the wandering of the blade wake is relatively small (Figure 3.43), the high  $k_{2D}$  is at the core of the TLV, and wake even though the strong positive vorticity exists in the wake, the low  $k_{2D}$  exists near the blade wake (Figure 3.42). For  $\varphi = 0.353$ , the TLV decays rapidly as it moves in the  $x$ -direction, and moves in the opposite direction of the blade rotation. The azimuthal migration speed of the TLV is faster than that of blade wake, and horizontal position of TLV and blade wake are similar between  $x/R_{tip} = 0.05$  and  $0.25$  (Figure 3.44, 3.46). For  $\varphi = 0.276$ , the TLV core does not exist in the  $x - r$  PIV plane at  $x/R_{tip} = 0.05$  (Figure 3.45) because the TLV is already broken in the blade passage. Instead, there is a high TKE due to the effect of broken TLV in areas outside the fan casing. The region of the Blade wake is almost the same as For  $\varphi = 0.353$  but its strength is weak (Figure 3.47). Figure 3.48-3.49 shows the phase-averaged velocity vectors and circumferential vorticity contour for  $\varphi = 0.353$  and  $0.276$ , respectively. At these two flow rates, a strong negative vorticity region exists

after the blade TE due to the blade wake. For  $\varphi = 0.353$ , the TLV existing near the tip gap gradually moves radially inward ( $-r$  direction).

Figure 3.50-3.51 shows the phase-averaged axial velocity ( $u_x$  profiles for various phase for  $\varphi = 0.353, 0.276$ , respectively. The solid black line is the averaged velocity profile calculated at 2,000 instantaneous flow fields measured without phase-rocking. In the region where the TLV is present ( $0.7 < x/R_{tip} < 1.0$  from -20 to 0), the main flow interferes with the course and the velocity decreases ( $0.3 < x/R_{tip} < 0.7$  from 10 to 30). The main flow velocity is also reduced in the blade wake region.

To investigate the interaction between the TLV and the blade wake, PIV is performed on the  $x - r$  plane from  $r/R_{tip} = 0.75$  to 1.0 for  $\varphi = 0.353, 0.276$  (Figure 3.52-3.55). From the instantaneous flow field and the mean flow field, a shear with positive and negative velocities, respectively developed in the PS and SS of the blade, is found just downstream of the blade TE. For  $\varphi = 0.353$ , the TLV is near the shear layer of the blade PS and has a vorticity with opposite signs.

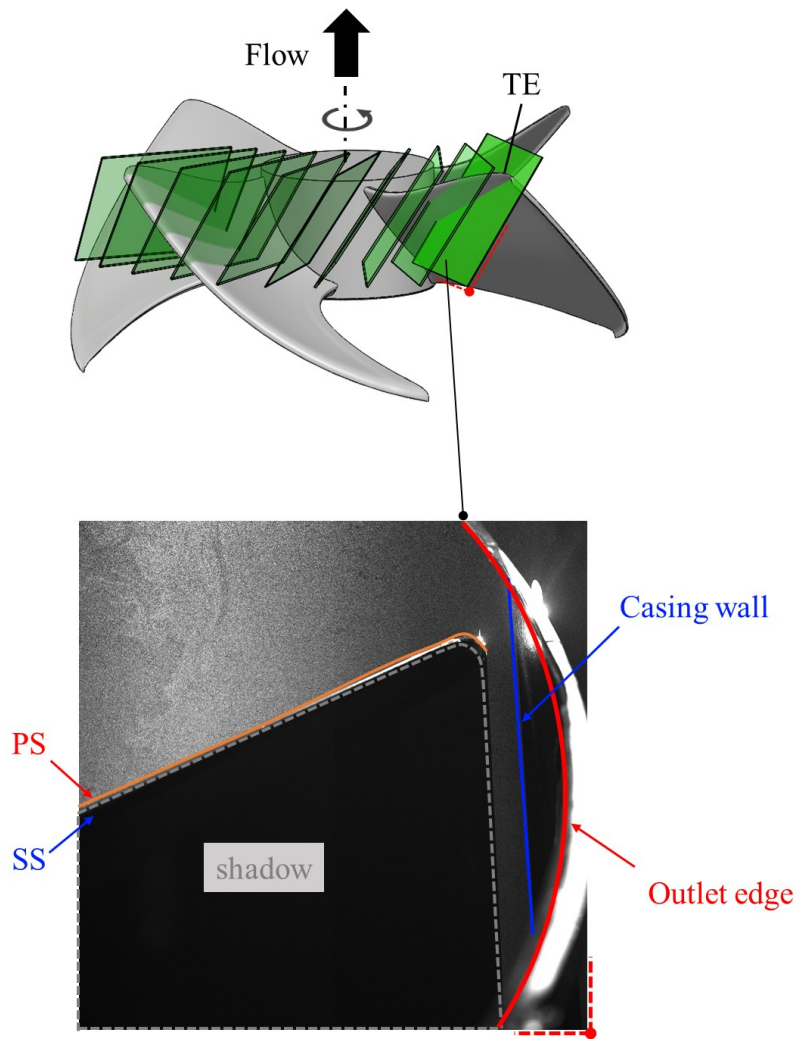


Figure 3.1. The particle image of the PIV plane near the trailing edge.

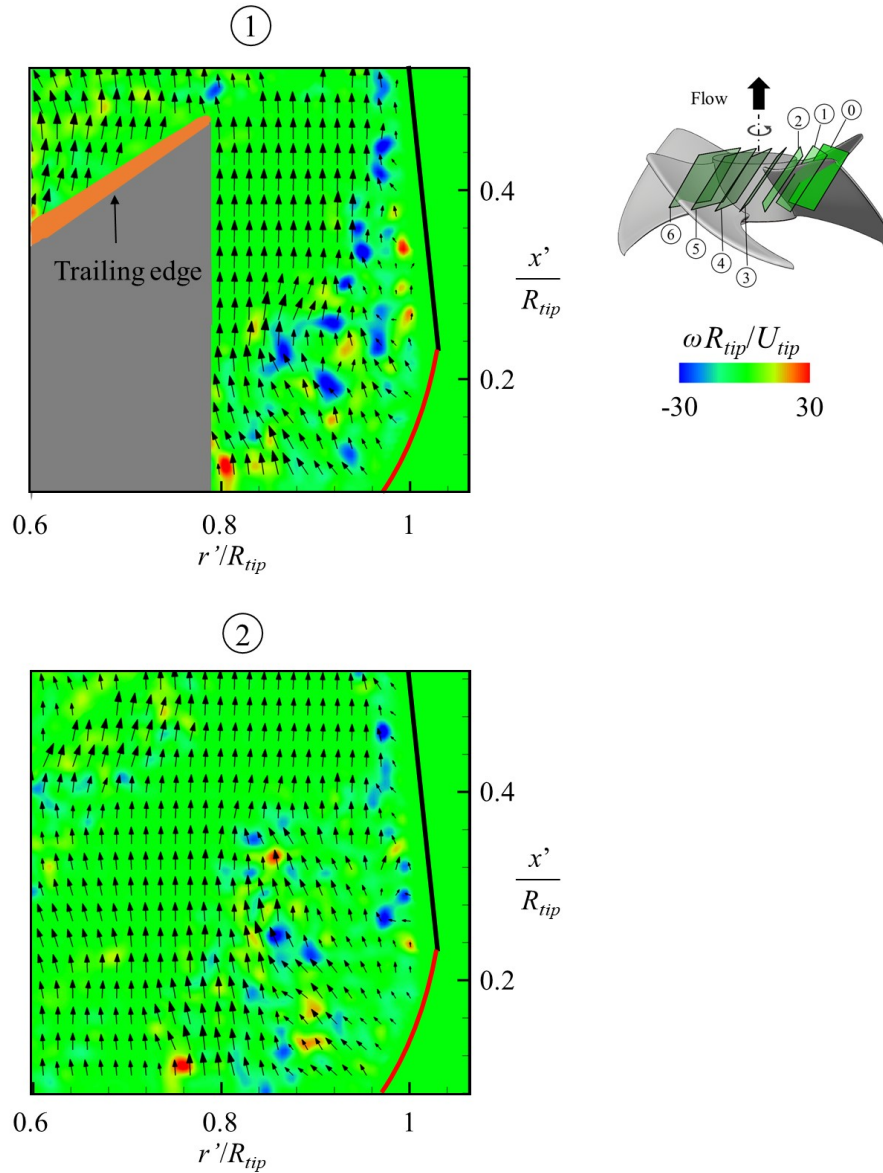


Figure 3.2. Instantaneous velocity vectors and contours of the instantaneous vorticity in the direction normal to the PIV planes for  $\varphi = 0.231$ . The grey area at the location of ① indicates the shadow caused by the blade. The thick black and red lines in these figures denote the locations of internal casing wall and outlet edge of the casing, respectively (see Figure 3.1).



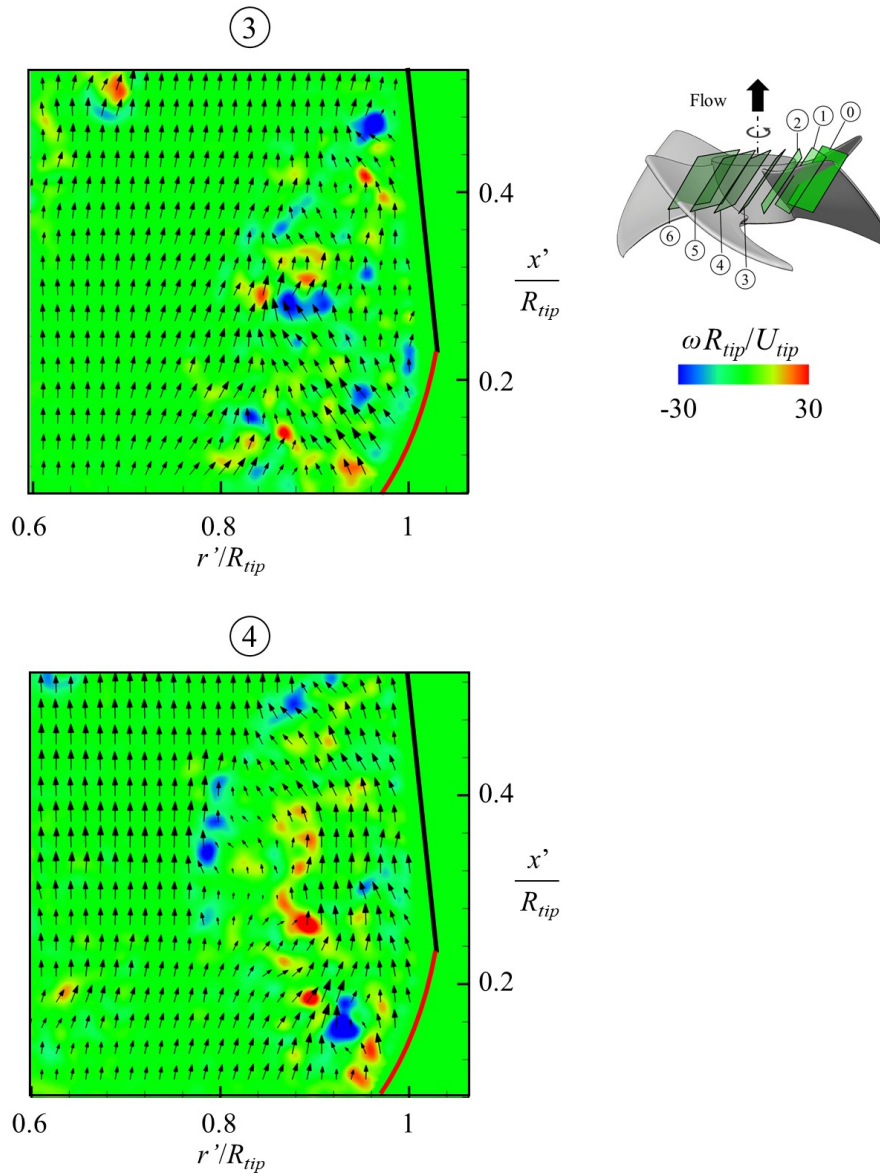


Figure 3.3. Instantaneous velocity vectors and contours of the instantaneous vorticity in the direction normal to the PIV planes for  $\varphi = 0.231$ . The thick black and red lines in these figures denote the locations of internal casing wall and outlet edge of the casing, respectively (see Figure 3.1).

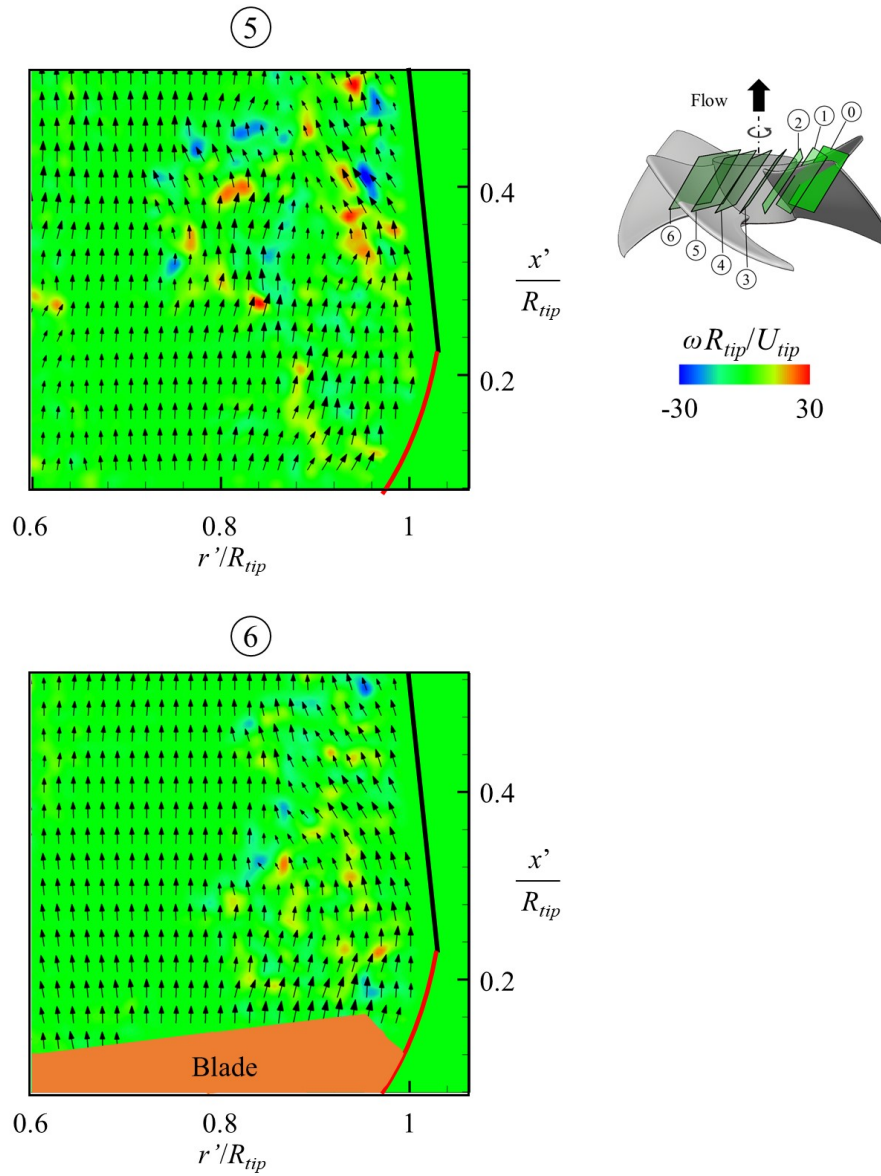


Figure 3.4. Instantaneous velocity vectors and contours of the instantaneous vorticity in the direction normal to the PIV planes for  $\varphi = 0.231$ . The thick black and red lines in these figures denote the locations of internal casing wall and outlet edge of the casing, respectively (see Figure 3.1).

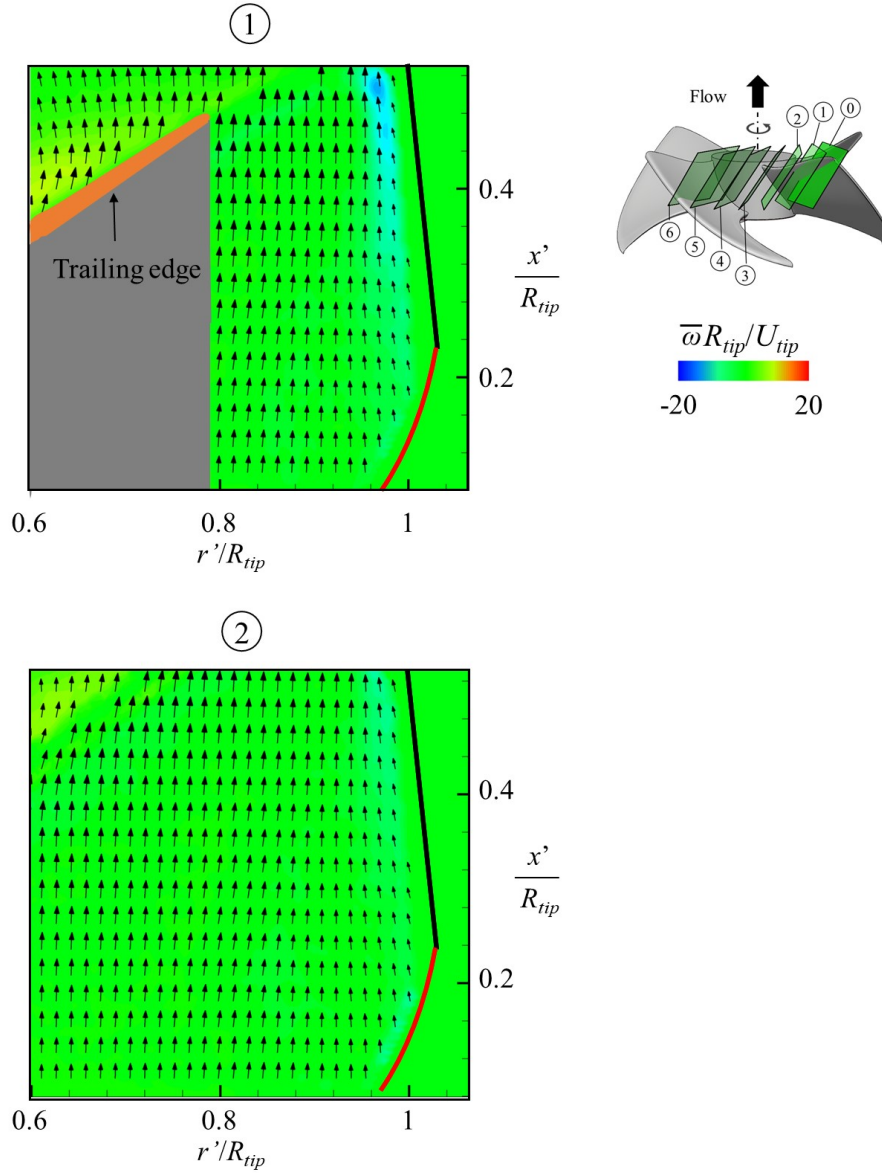


Figure 3.5. Contours of the phase-averaged vorticity in the direction normal to the PIV planes, together with the phase-averaged velocity vectors for  $\varphi = 0.231$ . The grey area at the location of ① indicates the shadow caused by the blade. The thick black and red lines in these figures denote the locations of internal casing wall and outlet edge of the casing, respectively (see Figure 3.1).

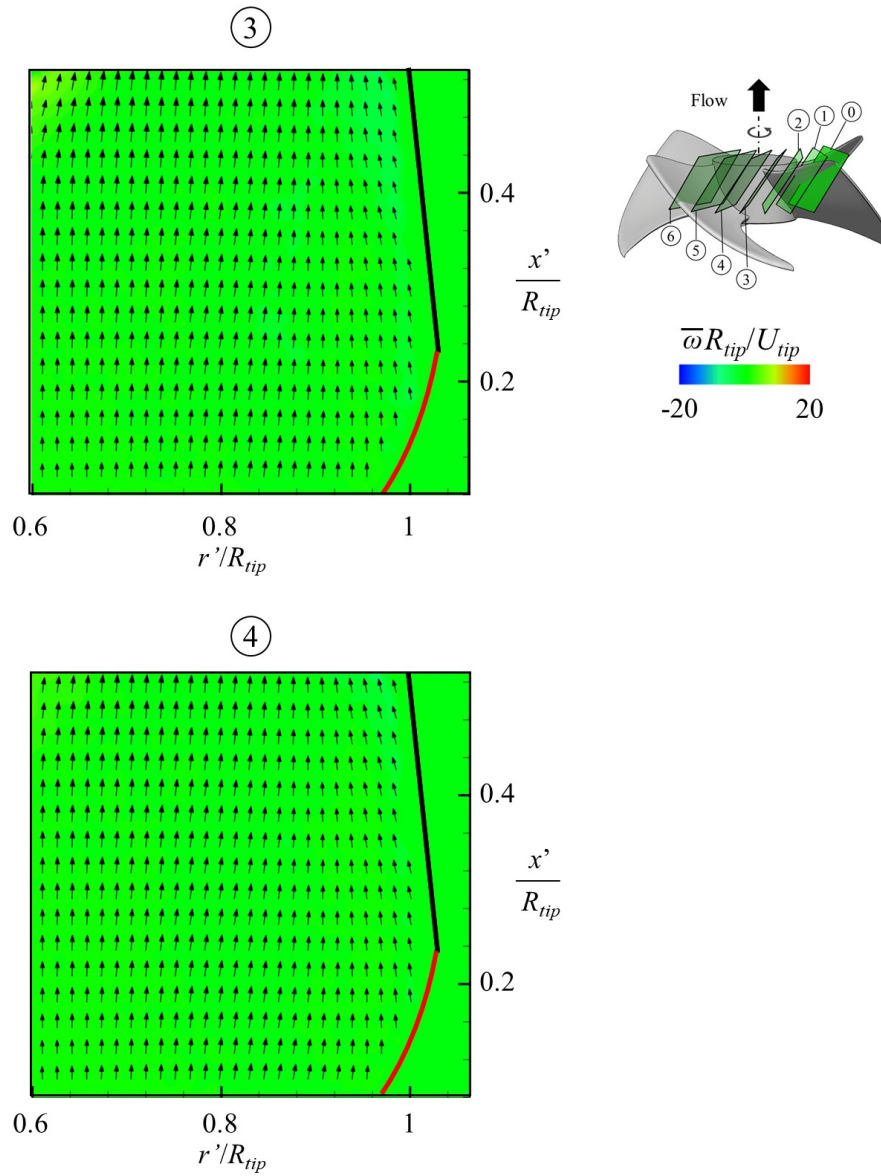


Figure 3.6. Contours of the phase-averaged vorticity in the direction normal to the PIV planes, together with the phase-averaged velocity vectors for  $\varphi = 0.231$ . The thick black and red lines in these figures denote the locations of internal casing wall and outlet edge of the casing, respectively (see Figure 3.1).

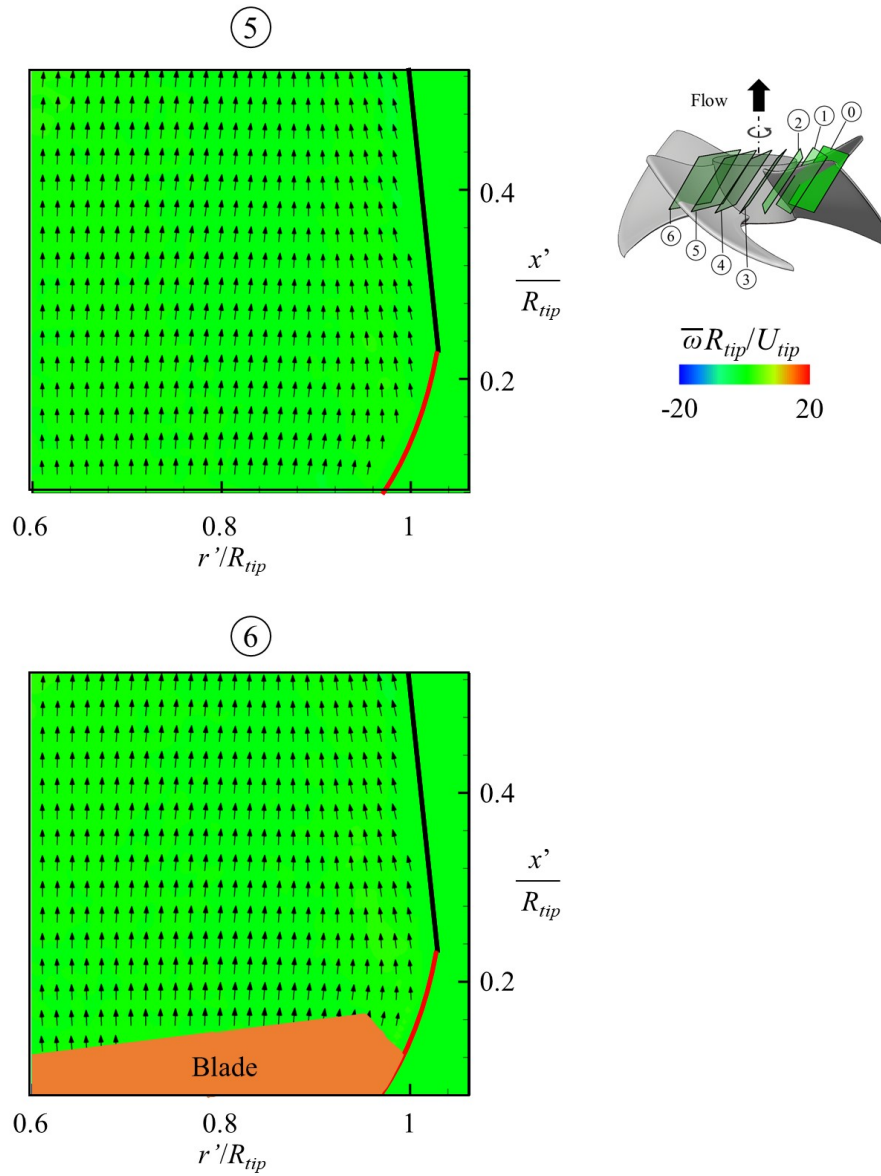


Figure 3.7. Contours of the phase-averaged vorticity in the direction normal to the PIV planes, together with the phase-averaged velocity vectors for  $\varphi = 0.231$ . The thick black and red lines in these figures denote the locations of internal casing wall and outlet edge of the casing, respectively (see Figure 3.1).

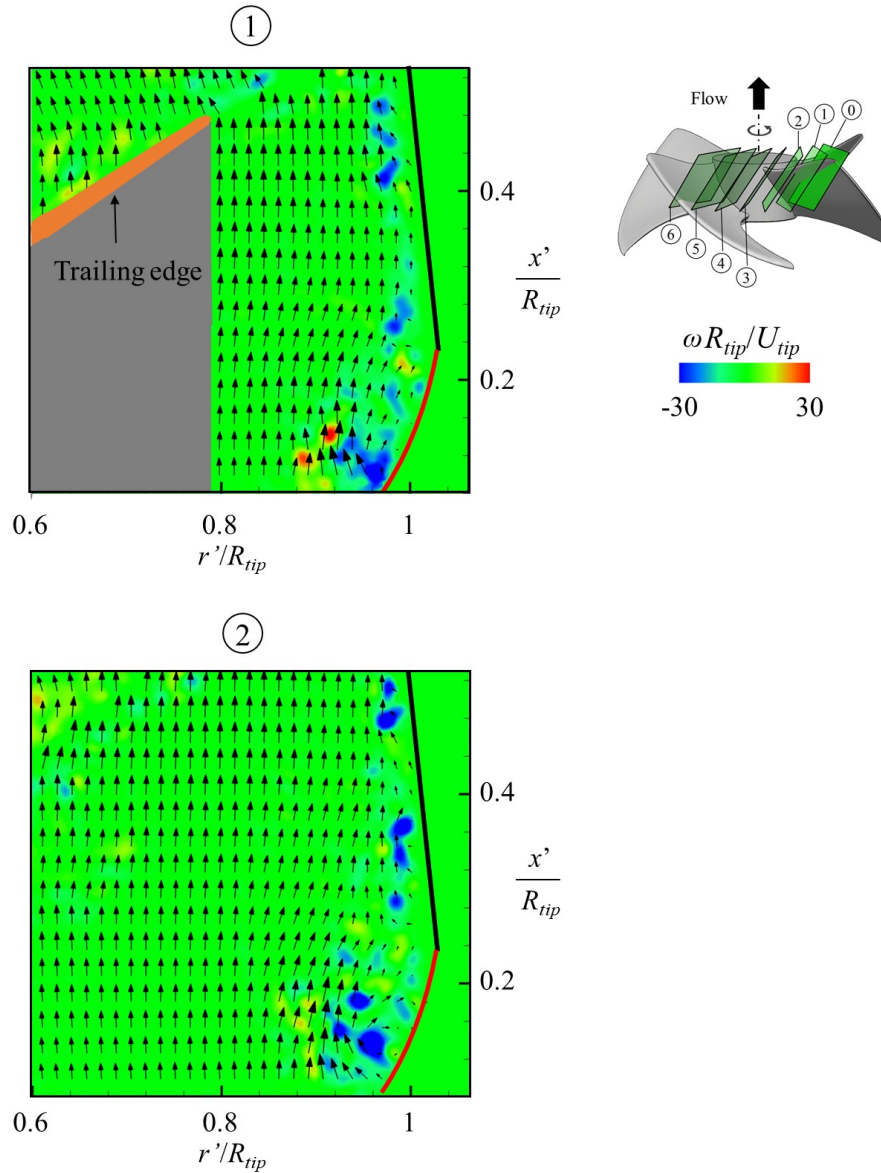


Figure 3.8. Instantaneous velocity vectors and contours of the instantaneous vorticity in the direction normal to the PIV planes for  $\varphi = 0.276$ . The grey area at the location of ① indicates the shadow caused by the blade. The thick black and red lines in these figures denote the locations of internal casing wall and outlet edge of the casing, respectively (see Figure 3.1).

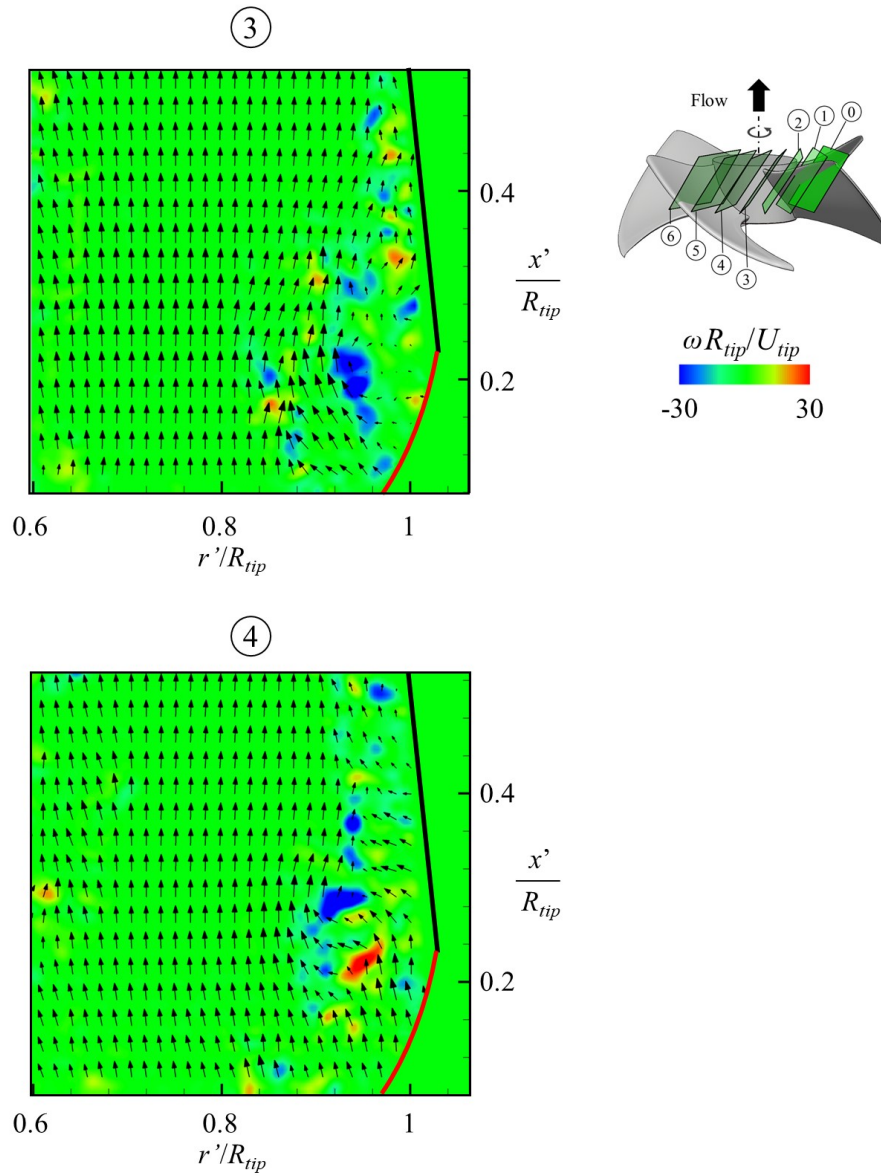


Figure 3.9. Instantaneous velocity vectors and contours of the instantaneous vorticity in the direction normal to the PIV planes for  $\varphi = 0.276$ . The thick black and red lines in these figures denote the locations of internal casing wall and outlet edge of the casing, respectively (see Figure 3.1).

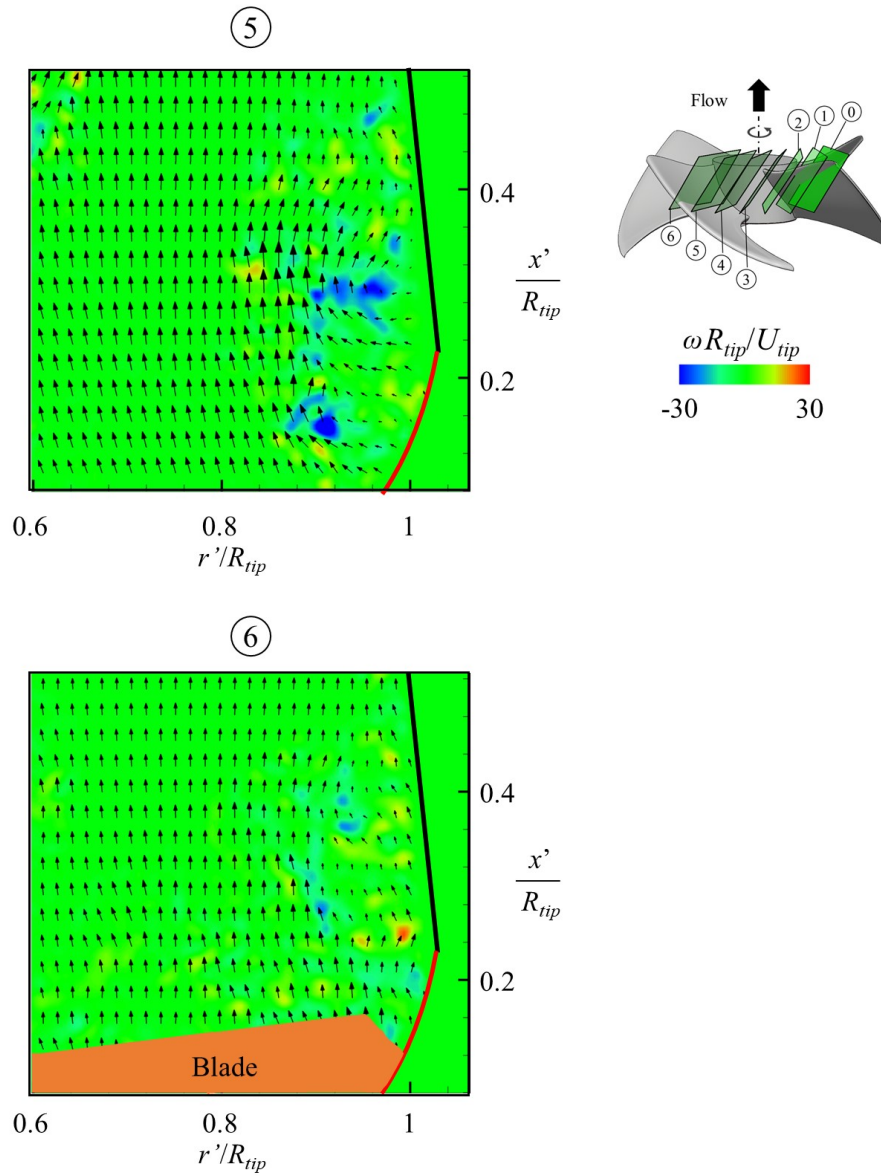


Figure 3.10. Instantaneous velocity vectors and contours of the instantaneous vorticity in the direction normal to the PIV planes for  $\varphi = 0.276$ . The thick black and red lines in these figures denote the locations of internal casing wall and outlet edge of the casing, respectively (see Figure 3.1).



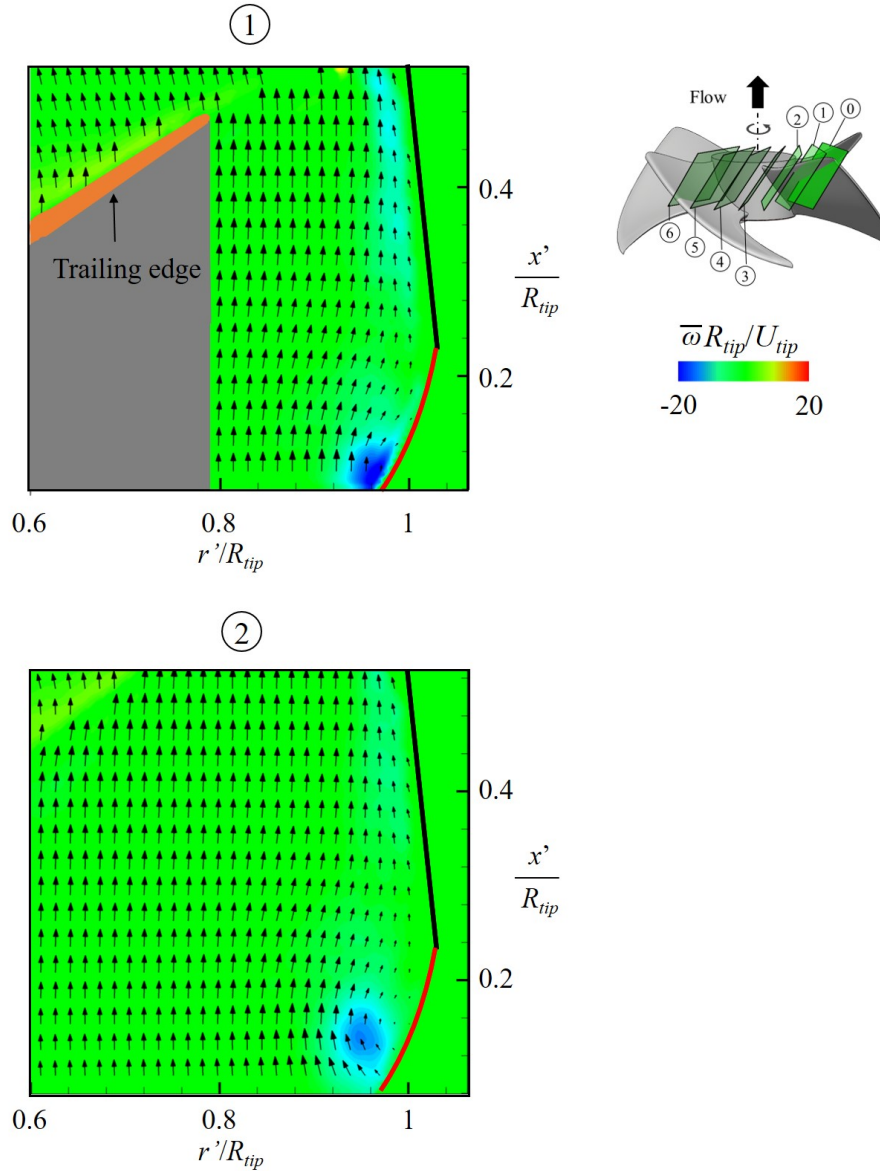


Figure 3.11. Contours of the phase-averaged vorticity in the direction normal to the PIV planes, together with the phase-averaged velocity vectors for  $\varphi = 0.276$ . The grey area at the location of ① indicates the shadow caused by the blade. The thick black and red lines in these figures denote the locations of internal casing wall and outlet edge of the casing, respectively (see Figure 3.1).

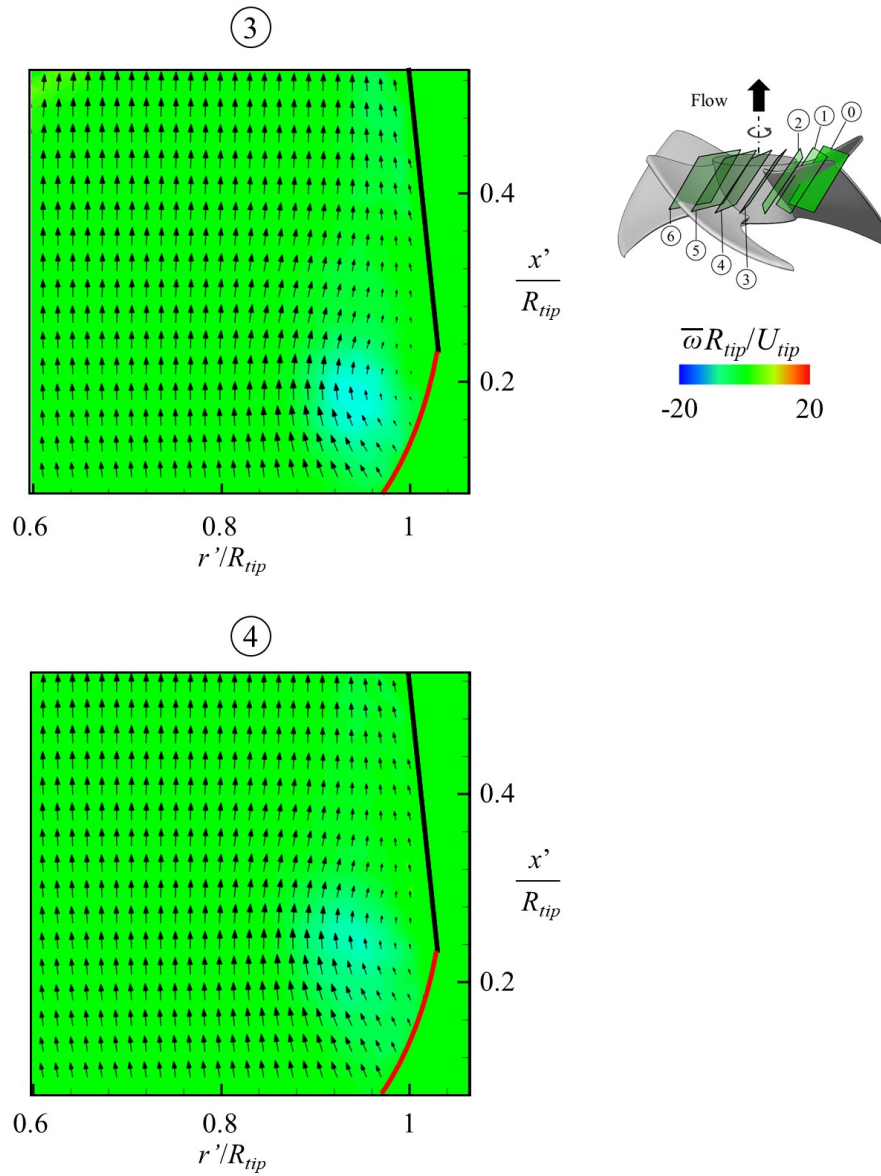


Figure 3.12. Contours of the phase-averaged vorticity in the direction normal to the PIV planes, together with the phase-averaged velocity vectors for  $\varphi = 0.276$ . The thick black and red lines in these figures denote the locations of internal casing wall and outlet edge of the casing, respectively (see Figure 3.1).

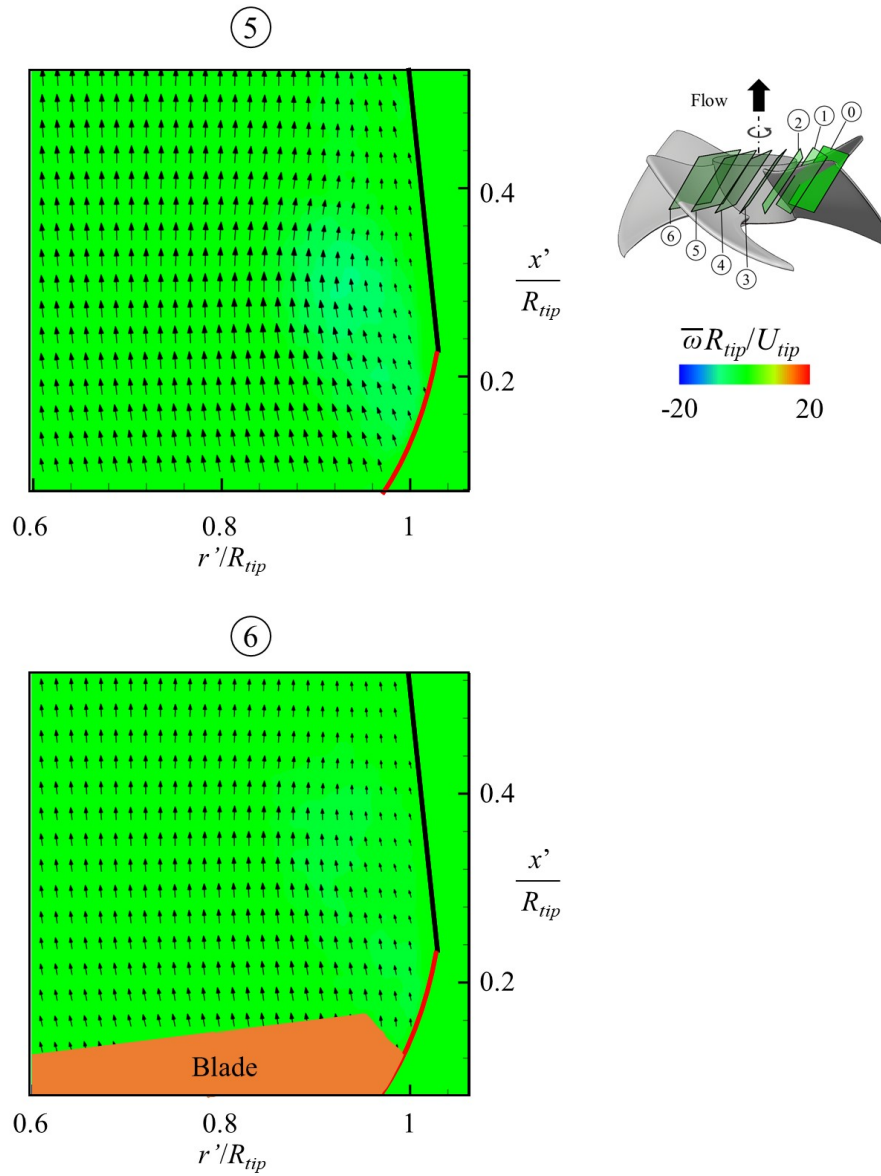


Figure 3.13. Contours of the phase-averaged vorticity in the direction normal to the PIV planes, together with the phase-averaged velocity vectors for  $\varphi = 0.276$ . The thick black and red lines in these figures denote the locations of internal casing wall and outlet edge of the casing, respectively (see Figure 3.1).

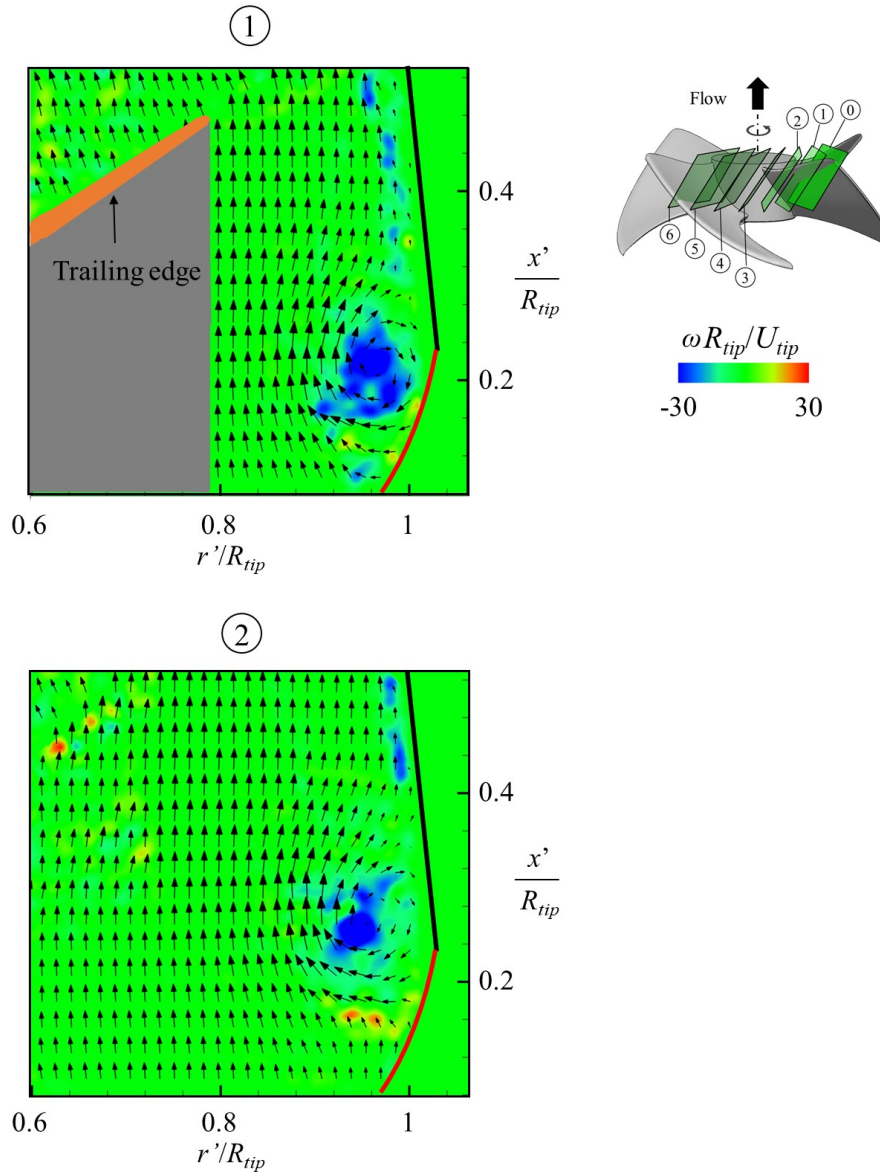


Figure 3.14. Instantaneous velocity vectors and contours of the instantaneous vorticity in the direction normal to the PIV planes for  $\varphi = 0.353$ . The grey area at the location of ① indicates the shadow caused by the blade. The thick black and red lines in these figures denote the locations of internal casing wall and outlet edge of the casing, respectively (see Figure 3.1).

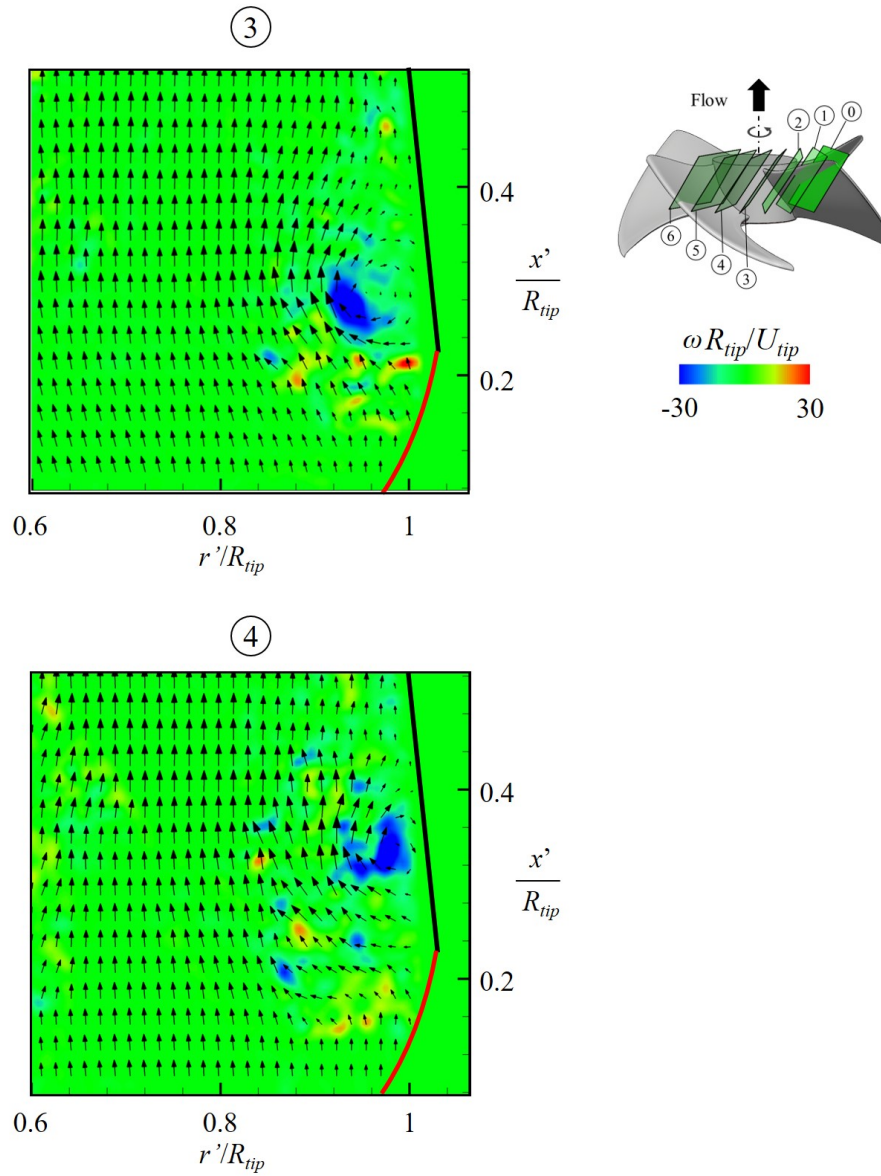


Figure 3.15. Instantaneous velocity vectors and contours of the instantaneous vorticity in the direction normal to the PIV planes for  $\varphi = 0.353$ . The thick black and red lines in these figures denote the locations of internal casing wall and outlet edge of the casing, respectively (see Figure 3.1).

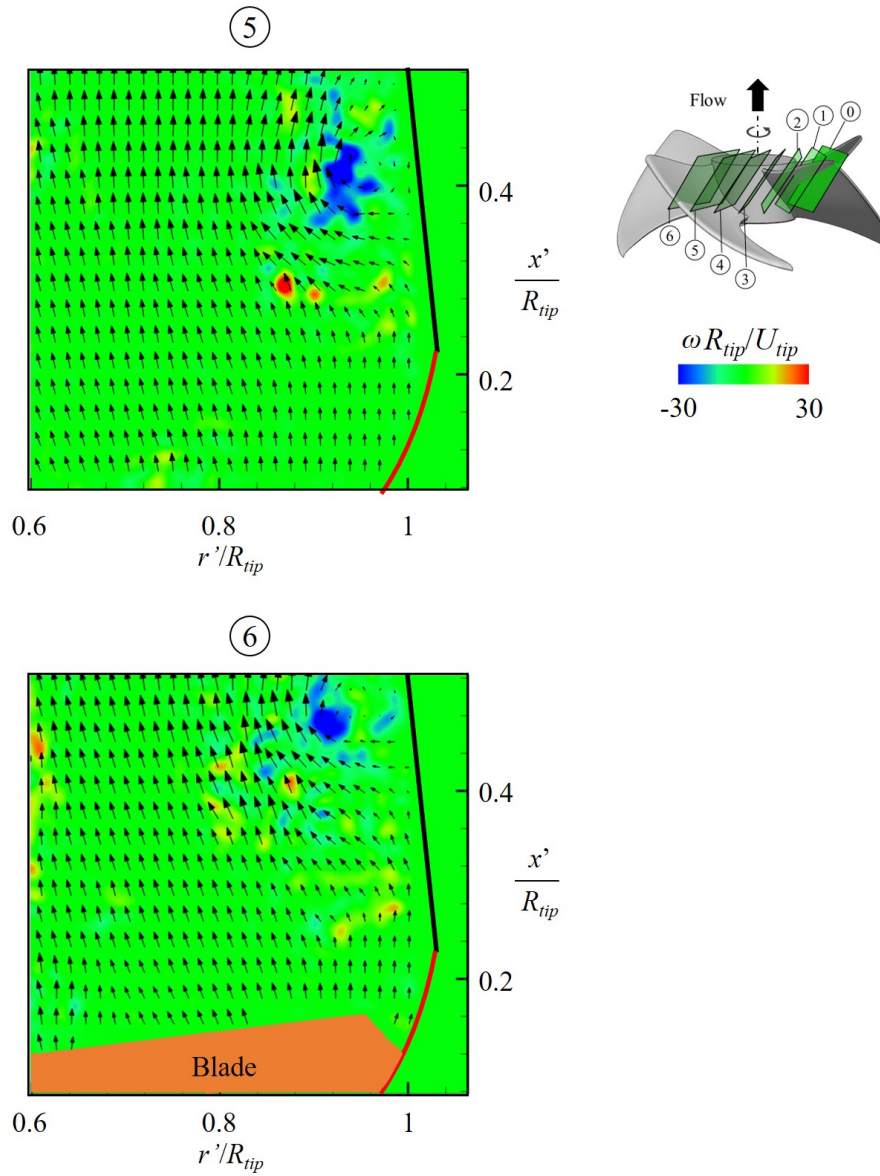


Figure 3.16. Instantaneous velocity vectors and contours of the instantaneous vorticity in the direction normal to the PIV planes for  $\varphi = 0.353$ . The thick black and red lines in these figures denote the locations of internal casing wall and outlet edge of the casing, respectively (see Figure 3.1).

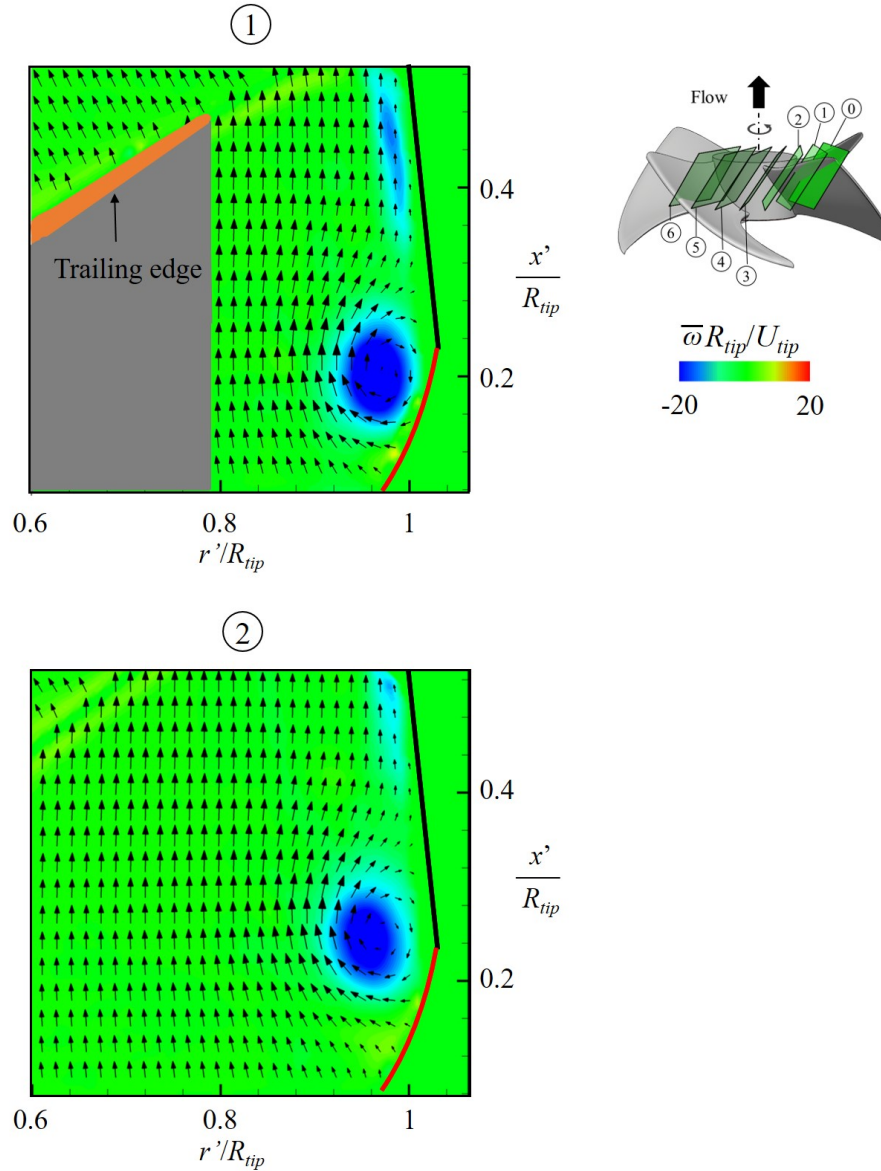


Figure 3.17. Contours of the phase-averaged vorticity in the direction normal to the PIV planes, together with the phase-averaged velocity vectors for  $\varphi = 0.353$ . The grey area at the location of ① indicates the shadow caused by the blade. The thick black and red lines in these figures denote the locations of internal casing wall and outlet edge of the casing, respectively (see Figure 3.1).

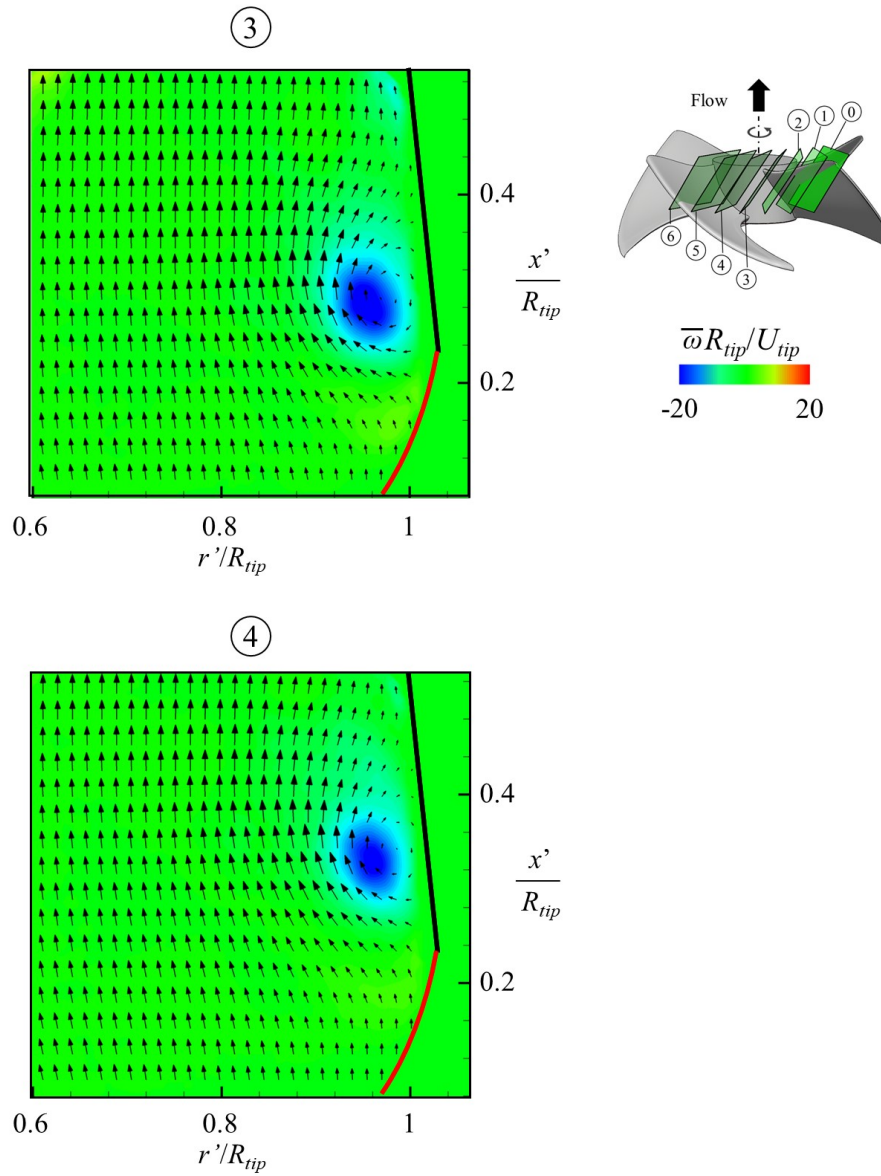


Figure 3.18. Contours of the phase-averaged vorticity in the direction normal to the PIV planes, together with the phase-averaged velocity vectors for  $\varphi = 0.353$ . The thick black and red lines in these figures denote the locations of internal casing wall and outlet edge of the casing, respectively (see Figure 3.1).



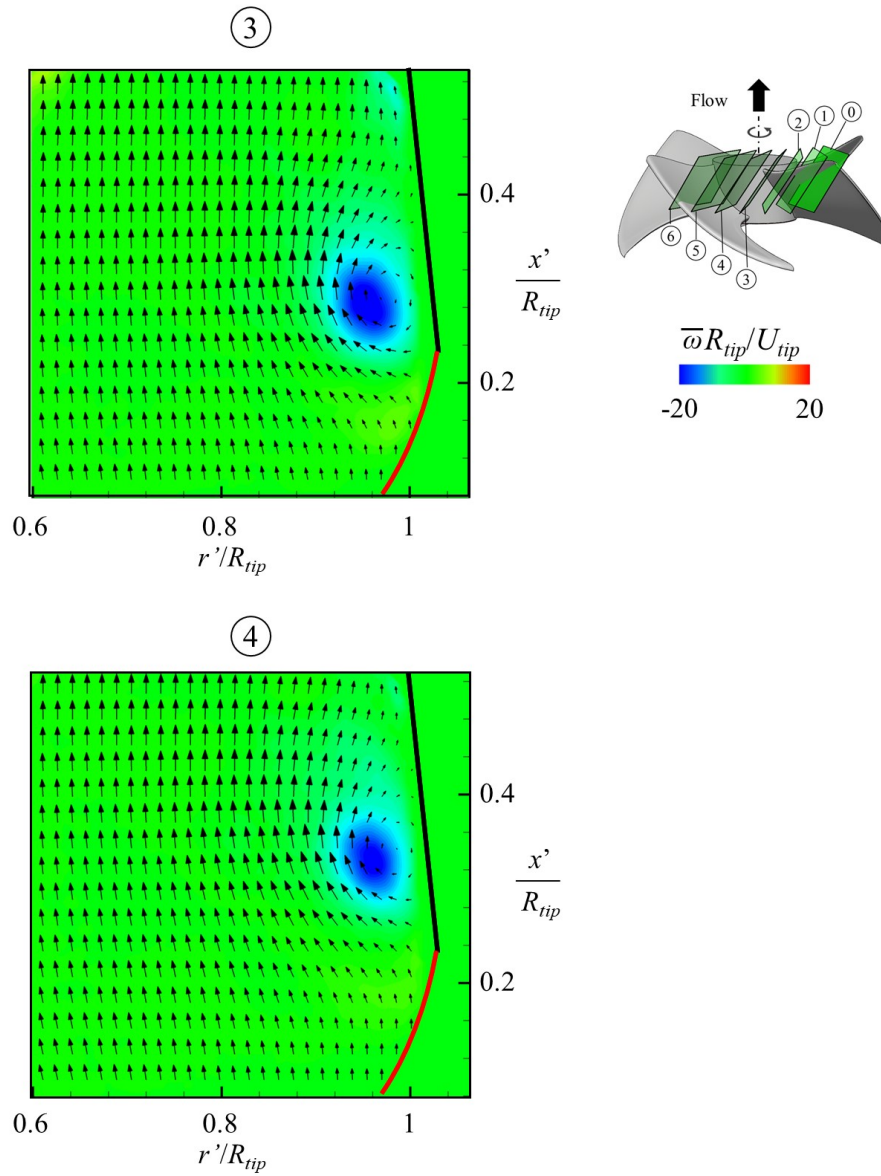


Figure 3.19. Contours of the phase-averaged vorticity in the direction normal to the PIV planes, together with the phase-averaged velocity vectors for  $\varphi = 0.353$ . The thick black and red lines in these figures denote the locations of internal casing wall and outlet edge of the casing, respectively (see Figure 3.1).

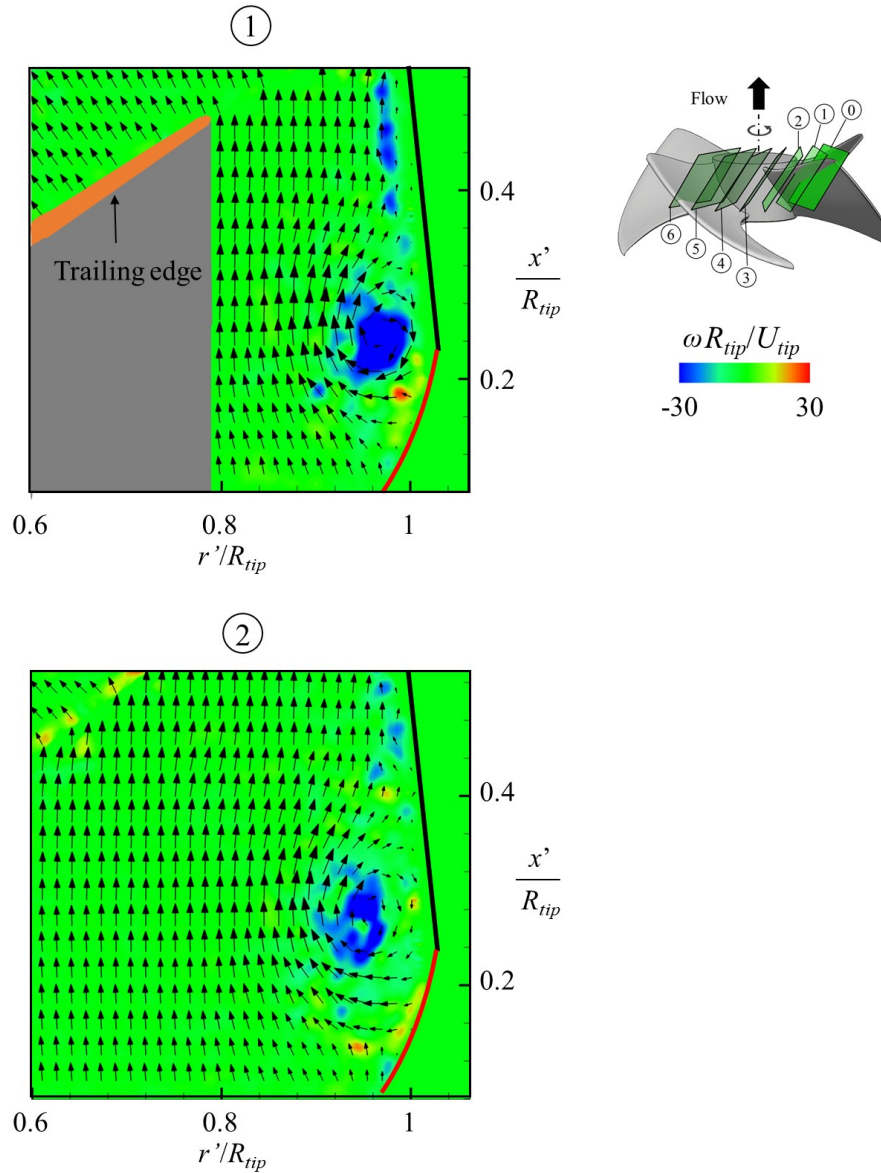


Figure 3.20. Instantaneous velocity vectors and contours of the instantaneous vorticity in the direction normal to the PIV planes for  $\varphi = 0.366$ . The grey area at the location of ① indicates the shadow caused by the blade. The thick black and red lines in these figures denote the locations of internal casing wall and outlet edge of the casing, respectively (see Figure 3.1).

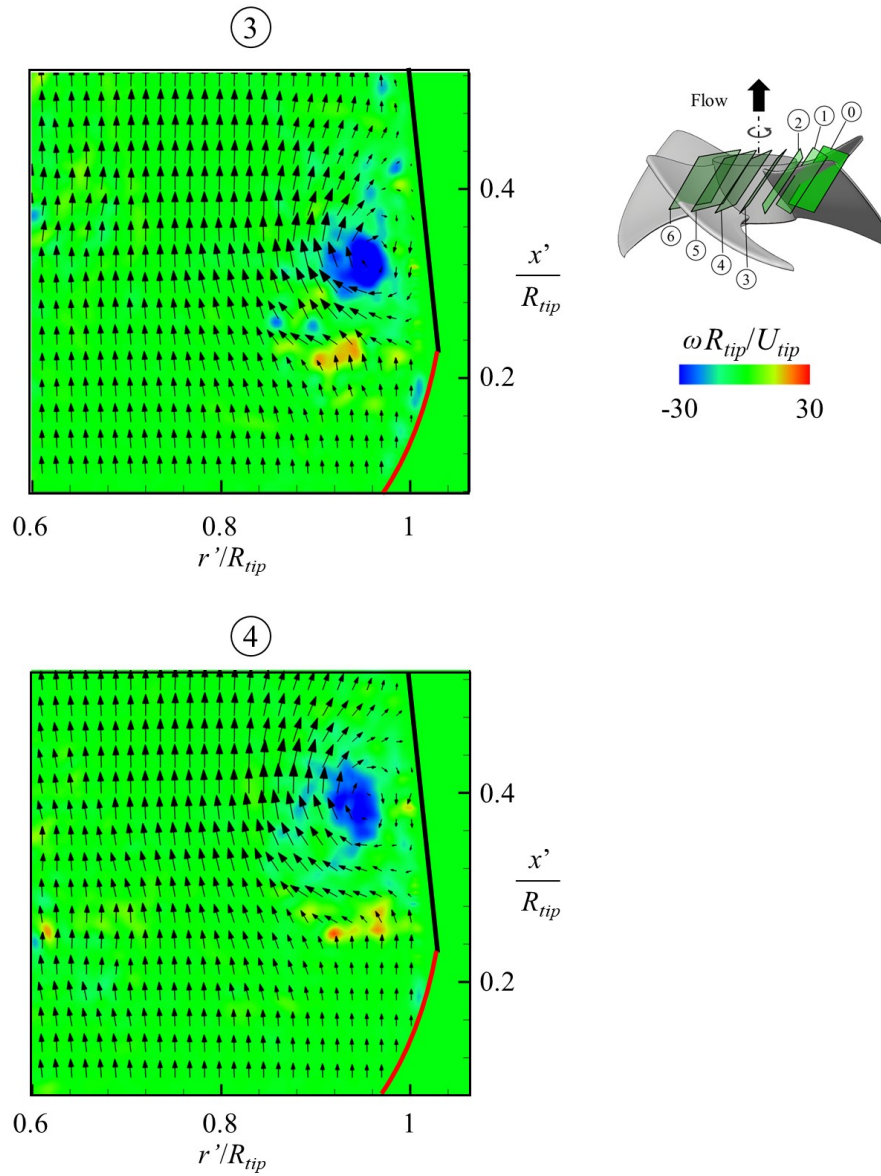


Figure 3.21. Instantaneous velocity vectors and contours of the instantaneous vorticity in the direction normal to the PIV planes for  $\varphi = 0.366$ . The thick black and red lines in these figures denote the locations of internal casing wall and outlet edge of the casing, respectively (see Figure 3.1).



Figure 3.22. Instantaneous velocity vectors and contours of the instantaneous vorticity in the direction normal to the PIV planes for  $\varphi = 0.366$ . The thick black and red lines in these figures denote the locations of internal casing wall and outlet edge of the casing, respectively (see Figure 3.1).

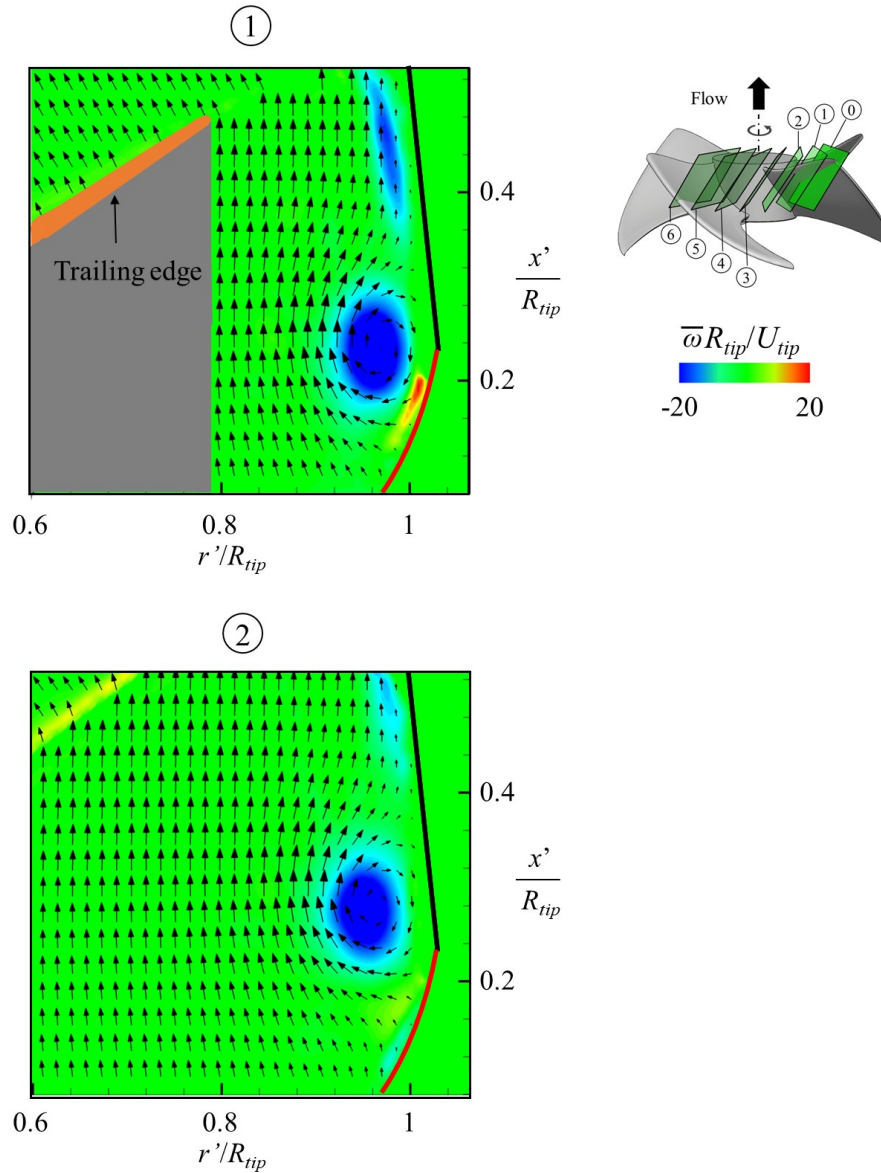


Figure 3.23. Contours of the phase-averaged vorticity in the direction normal to the PIV planes, together with the phase-averaged velocity vectors for  $\varphi = 0.366$ . The grey area at the location of ① indicates the shadow caused by the blade. The thick black and red lines in these figures denote the locations of internal casing wall and outlet edge of the casing, respectively (see Figure 3.1).

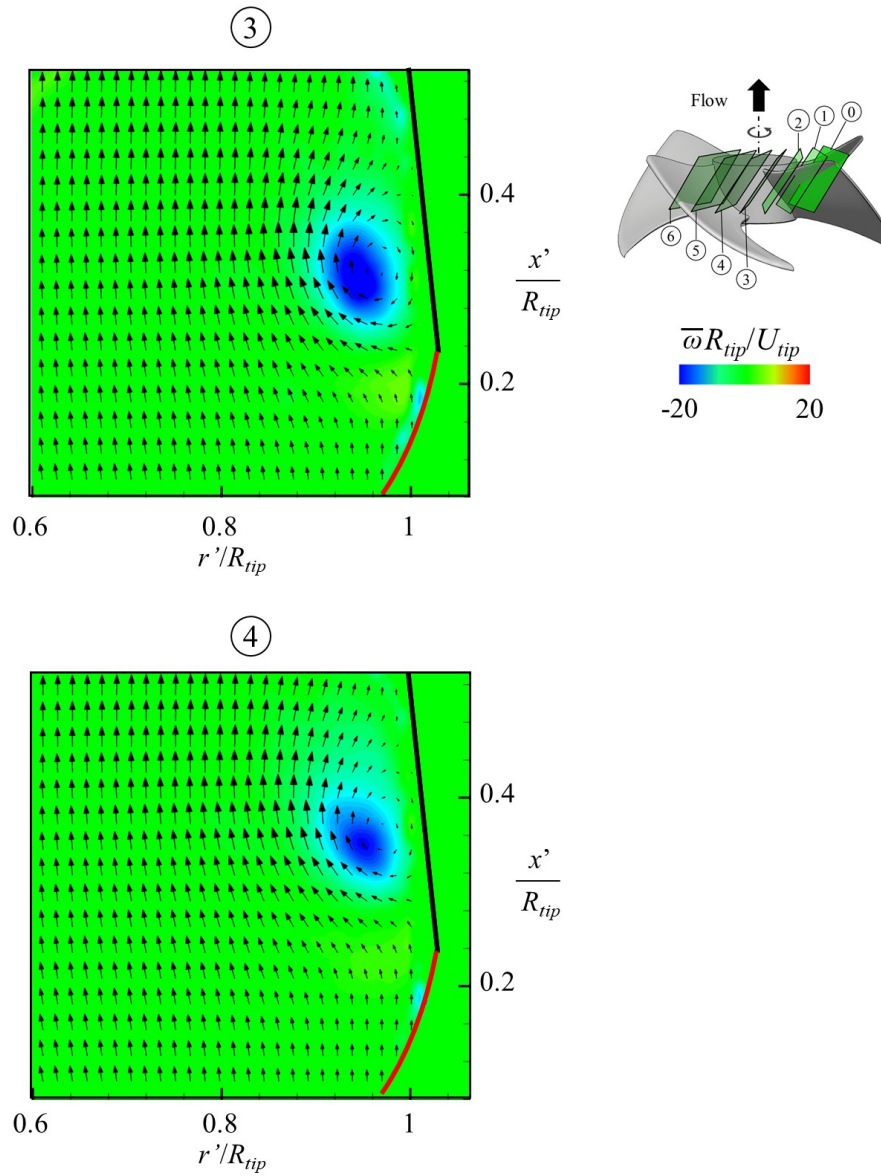


Figure 3.24. Contours of the phase-averaged vorticity in the direction normal to the PIV planes, together with the phase-averaged velocity vectors for  $\varphi = 0.366$ . The thick black and red lines in these figures denote the locations of internal casing wall and outlet edge of the casing, respectively (see Figure 3.1).

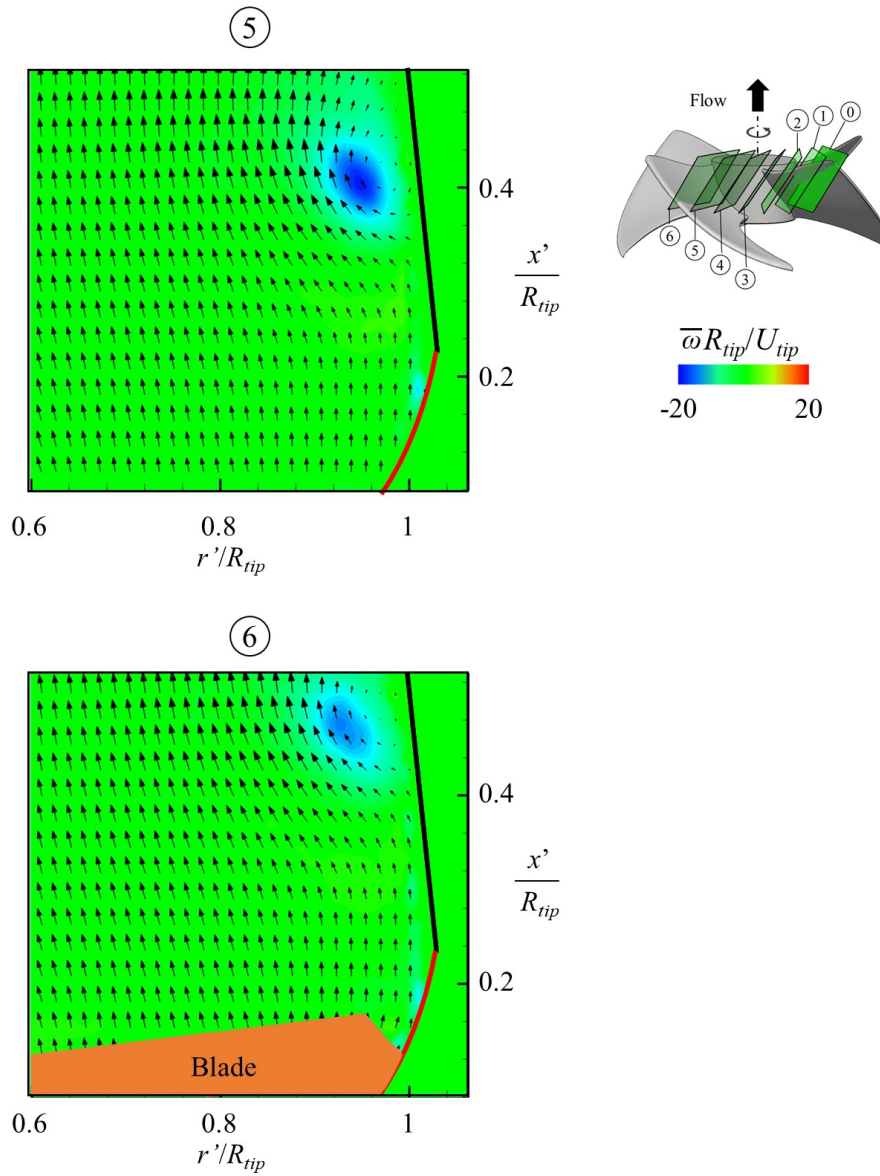


Figure 3.25. Contours of the phase-averaged vorticity in the direction normal to the PIV planes, together with the phase-averaged velocity vectors for  $\varphi = 0.366$ . The thick black and red lines in these figures denote the locations of internal casing wall and outlet edge of the casing, respectively (see Figure 3.1).

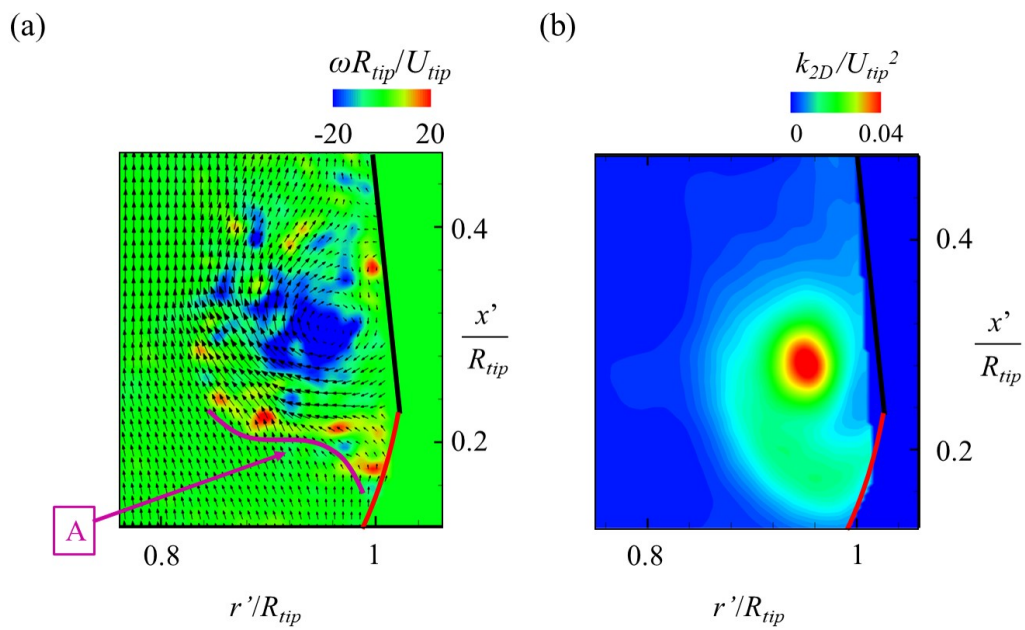


Figure 3.26. Magnified view of Figure 3.15 at ③: (a) instantaneous velocity vectors and contours of the instantaneous vorticity in the direction normal to the PIV plane; (b) contours of the 2D turbulent kinetic energy. In (a), A denotes an approximate region where the mean flow encounters the TLV.



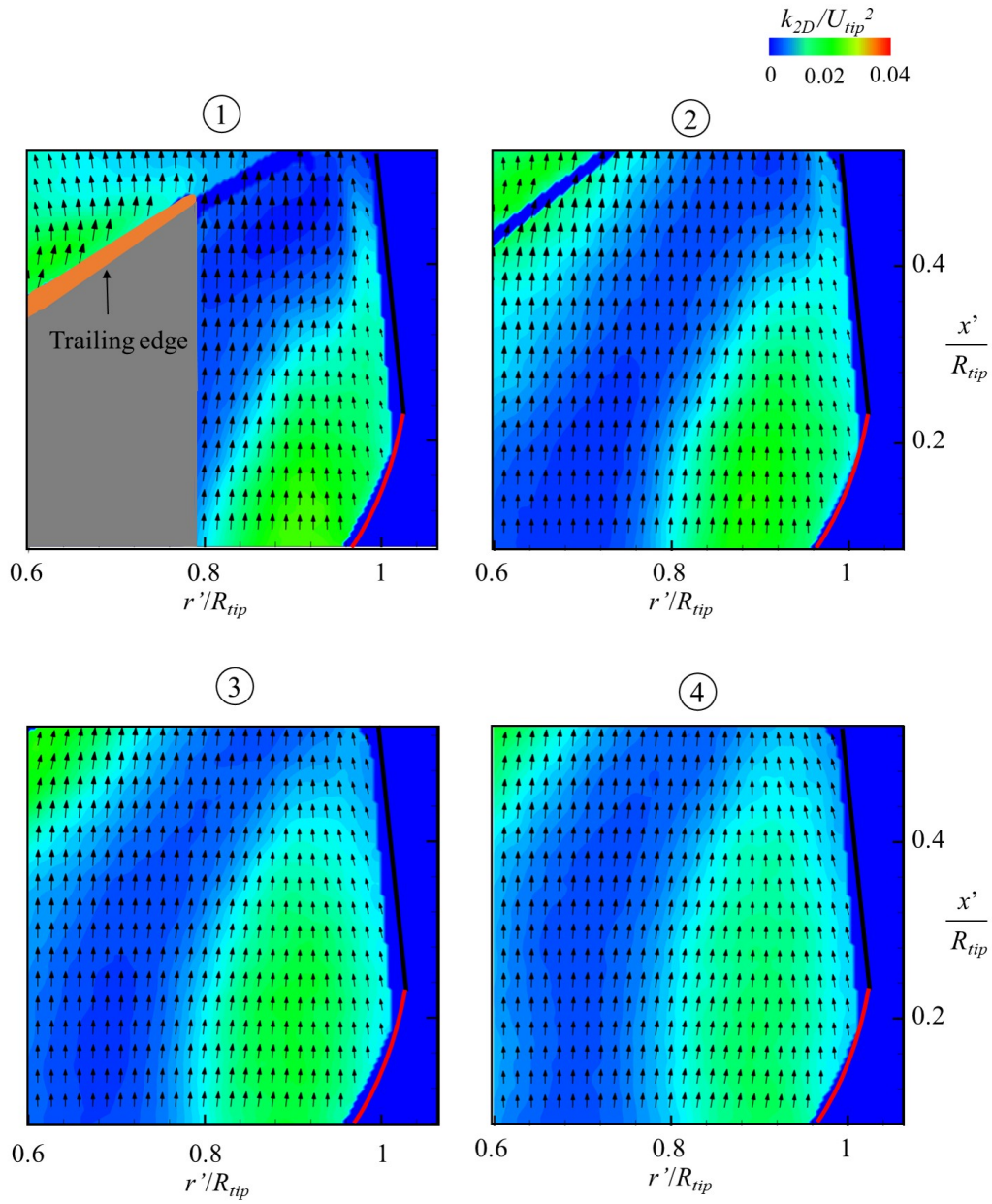


Figure 3.27. Contours of the 2D turbulent kinetic energy and phase-averaged velocity vectors on the PIV planes for  $\varphi = 0.231$ . The number on the top of each figure denotes the measurement location shown in Figure 3.31.

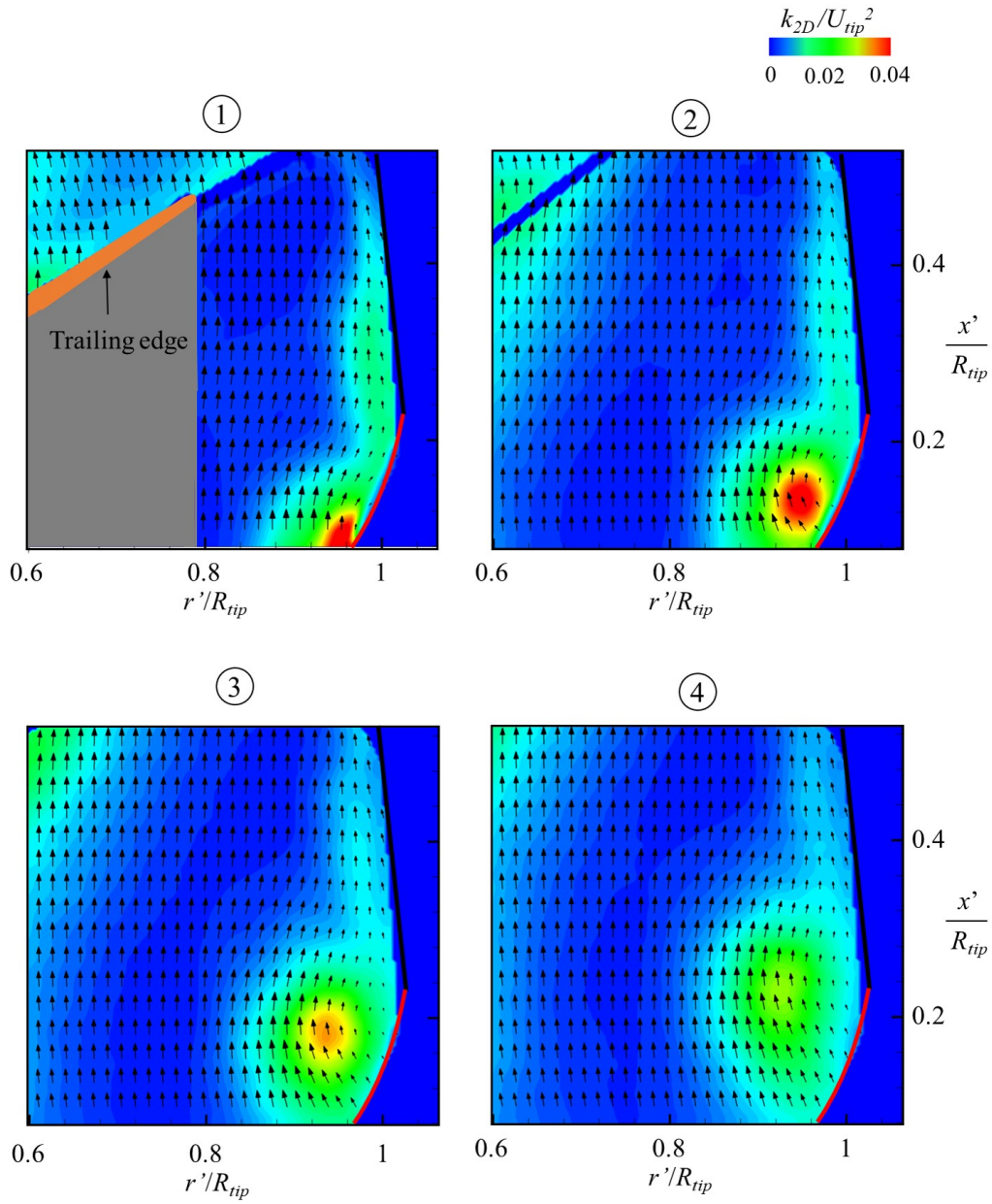


Figure 3.28. Contours of the 2D turbulent kinetic energy and phase-averaged velocity vectors on the PIV planes for  $\varphi = 0.276$ . The number on the top of each figure denotes the measurement location shown in Figure 3.31.

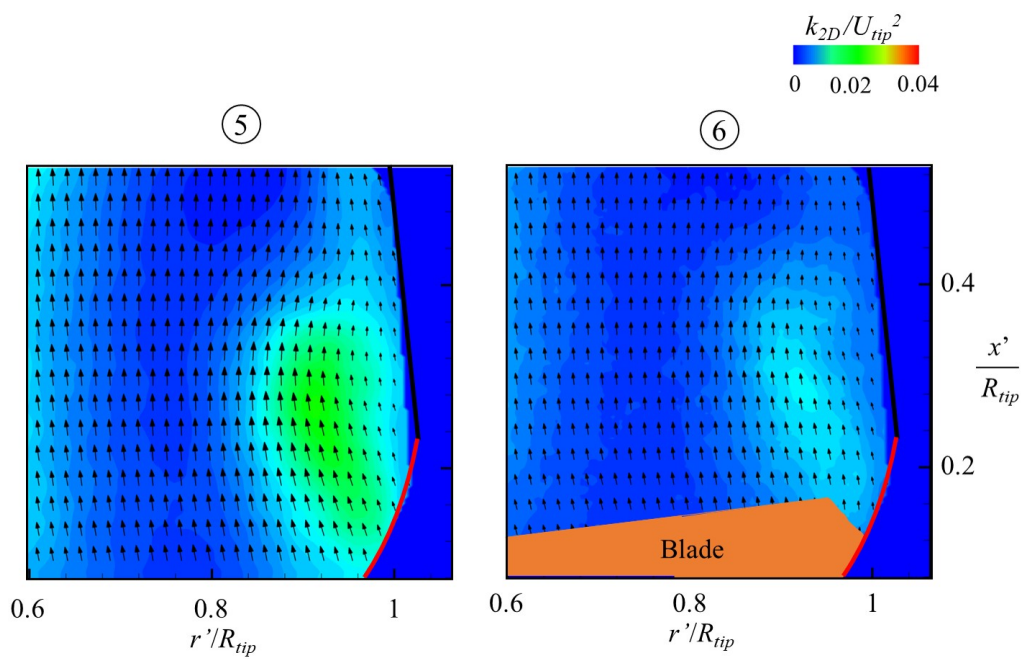


Figure 3.29. Contours of the 2D turbulent kinetic energy and phase-averaged velocity vectors on the PIV planes for  $\varphi = 0.276$ . The number on the top of each figure denotes the measurement location shown in Figure 3.31.

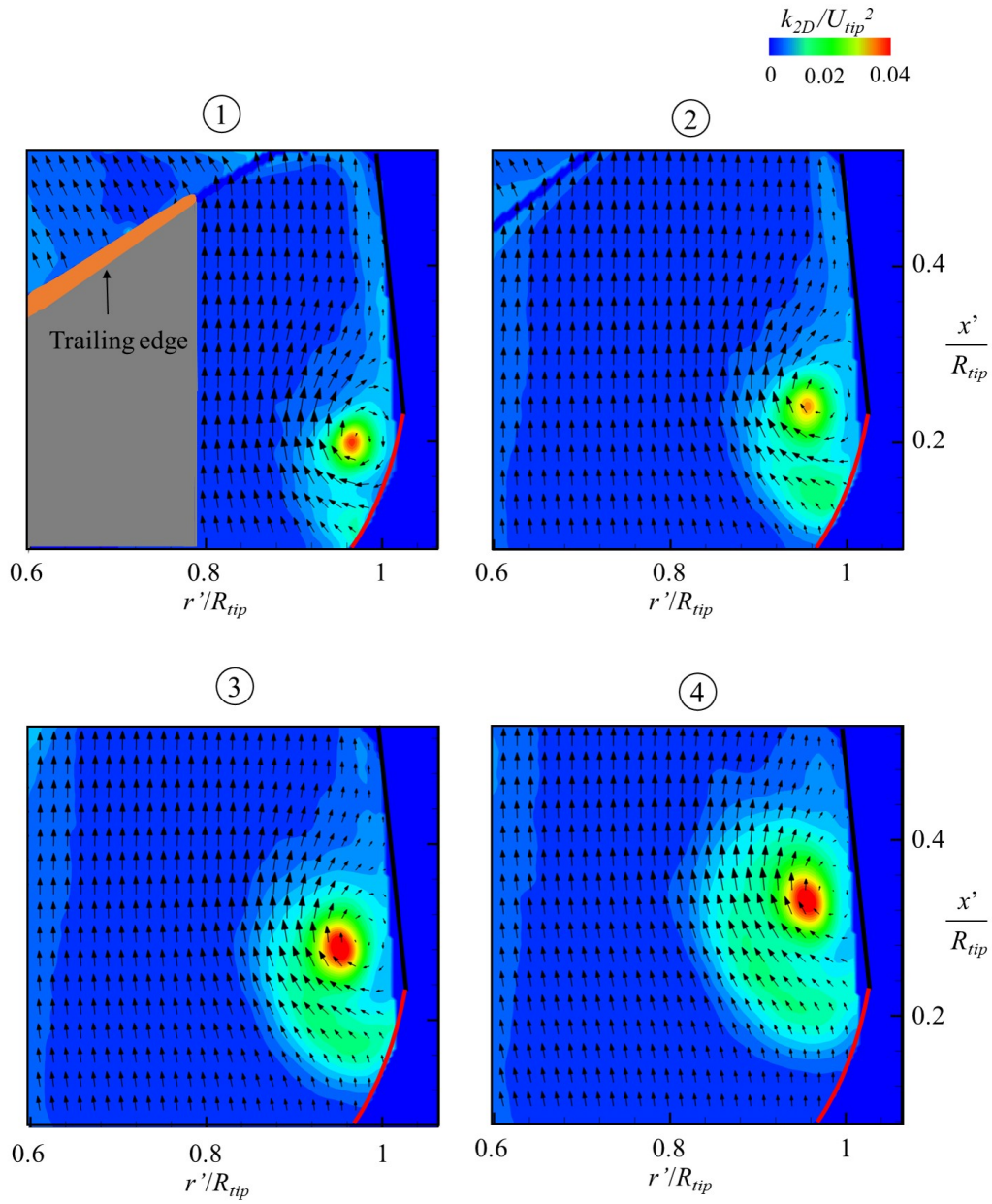


Figure 3.30. Contours of the 2D turbulent kinetic energy and phase-averaged velocity vectors on the PIV planes for  $\varphi = 0.353$ . The number on the top of each figure denotes the measurement location shown in Figure 3.31.

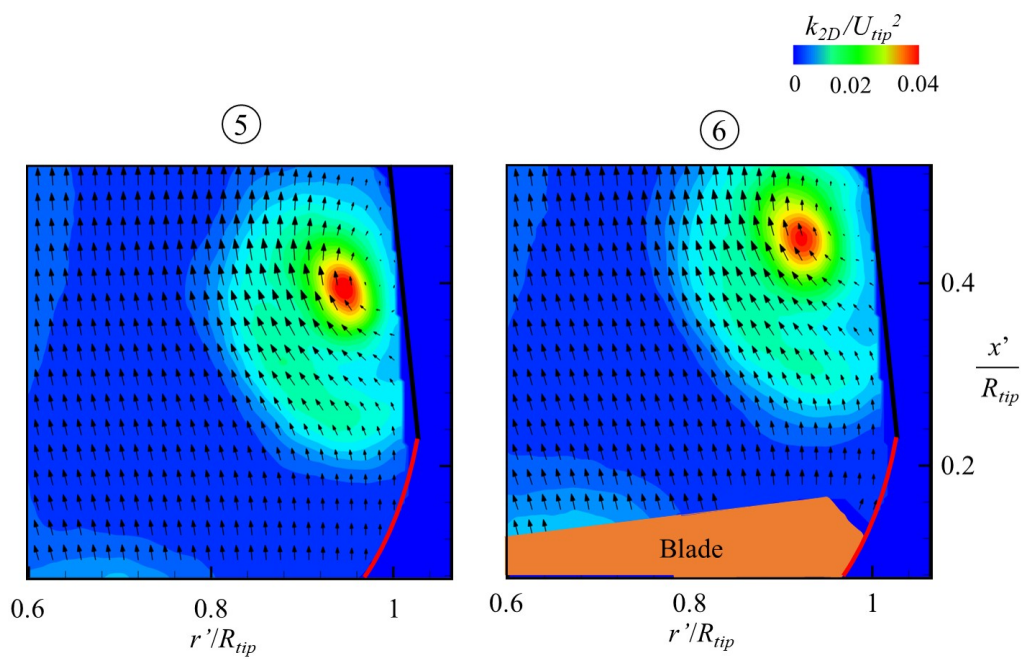


Figure 3.31. Contours of the 2D turbulent kinetic energy and phase-averaged velocity vectors on the PIV planes for  $\varphi = 0.353$ . The number on the top of each figure denotes the measurement location shown in Figure 3.31.

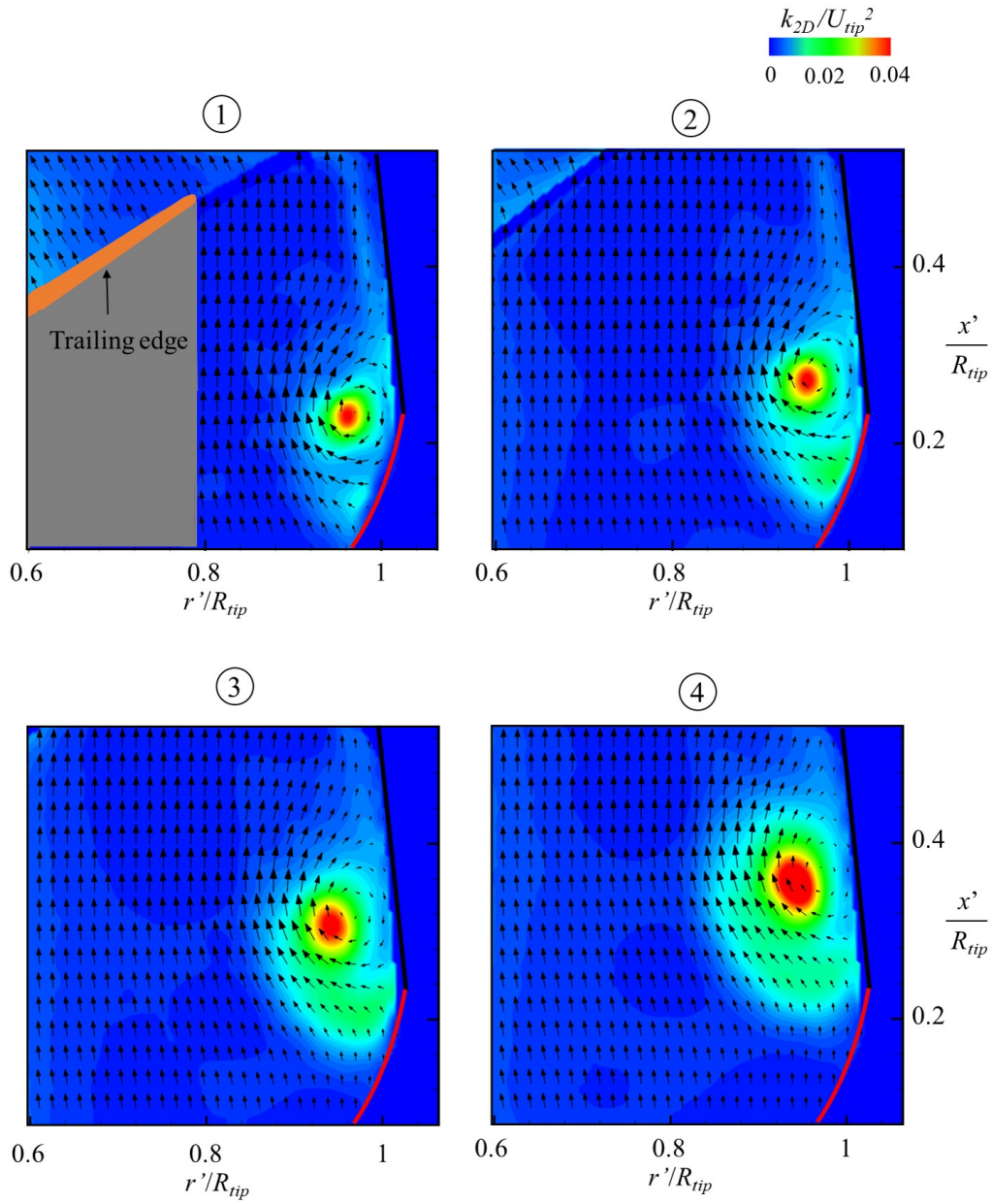


Figure 3.32. Contours of the 2D turbulent kinetic energy and phase-averaged velocity vectors on the PIV planes for  $\varphi = 0.366$ . The number on the top of each figure denotes the measurement location shown in Figure 3.31.

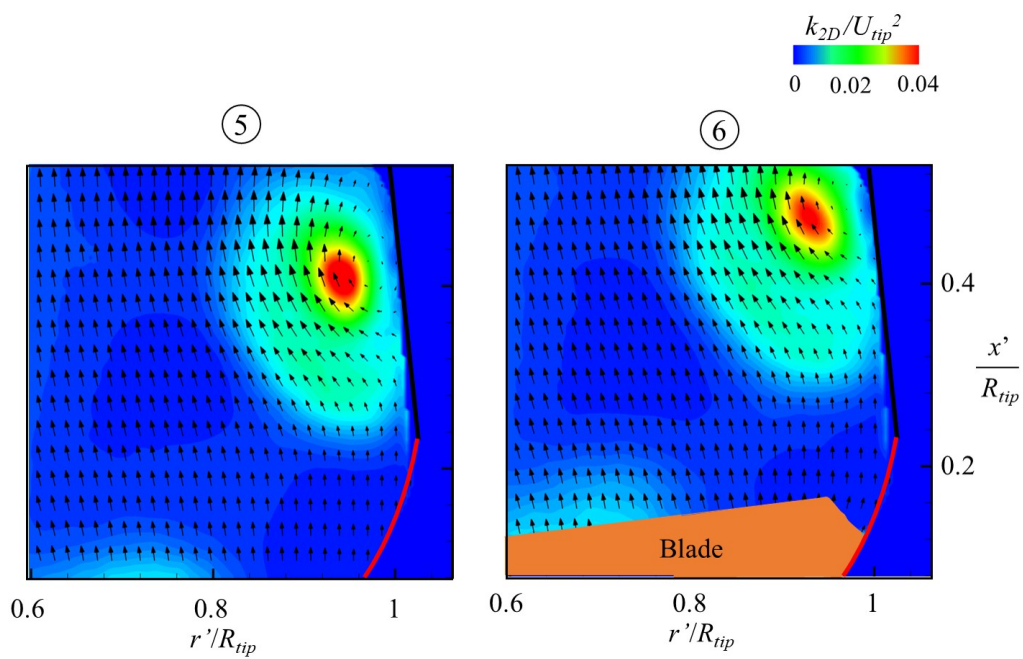


Figure 3.33. Contours of the 2D turbulent kinetic energy and phase-averaged velocity vectors on the PIV planes for  $\varphi = 0.366$ . The number on the top of each figure denotes the measurement location shown in Figure 3.31.

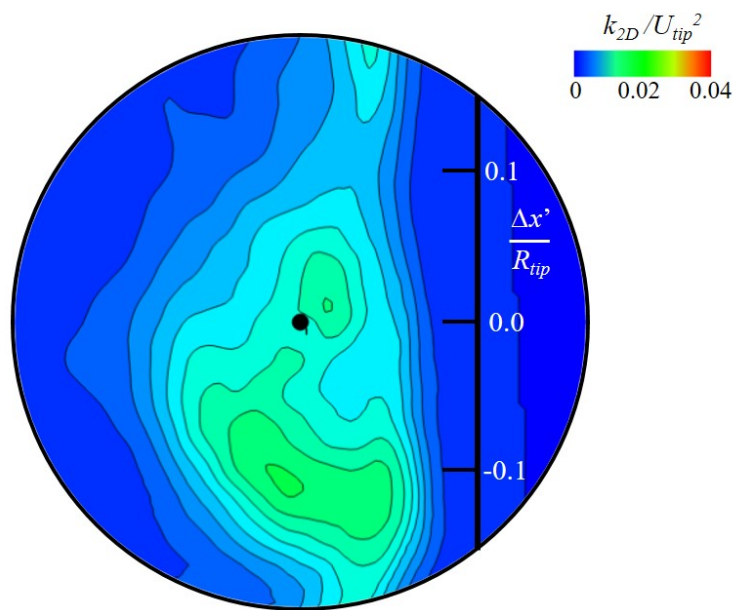


Figure 3.34. Contour of the 2D turbulent kinetic energy from re-centered data of the PIV plane at for  $\varphi = 0.353$ . A solid circle in this figure denotes the location of the phase-averaged TLV center.



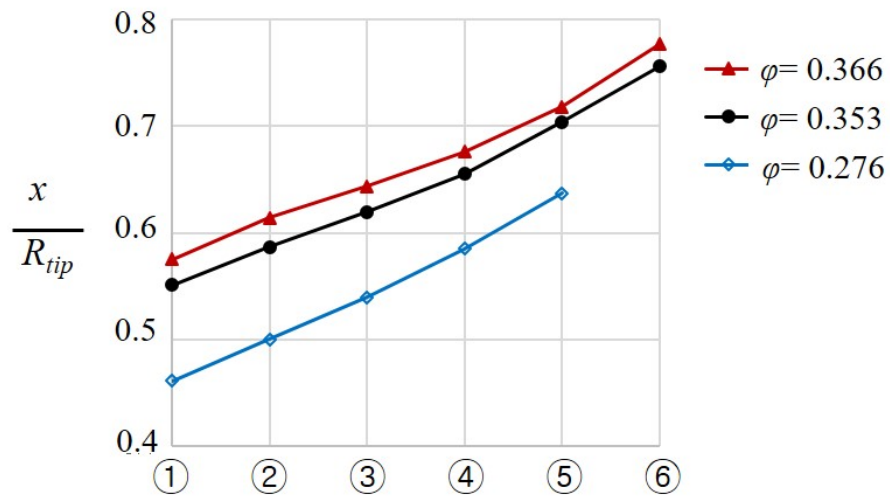


Figure 3.35. Locations of the phase-averaged TLV center in the axial direction for three flow rates. Here,  $x$  is the axial position from the blade LE.

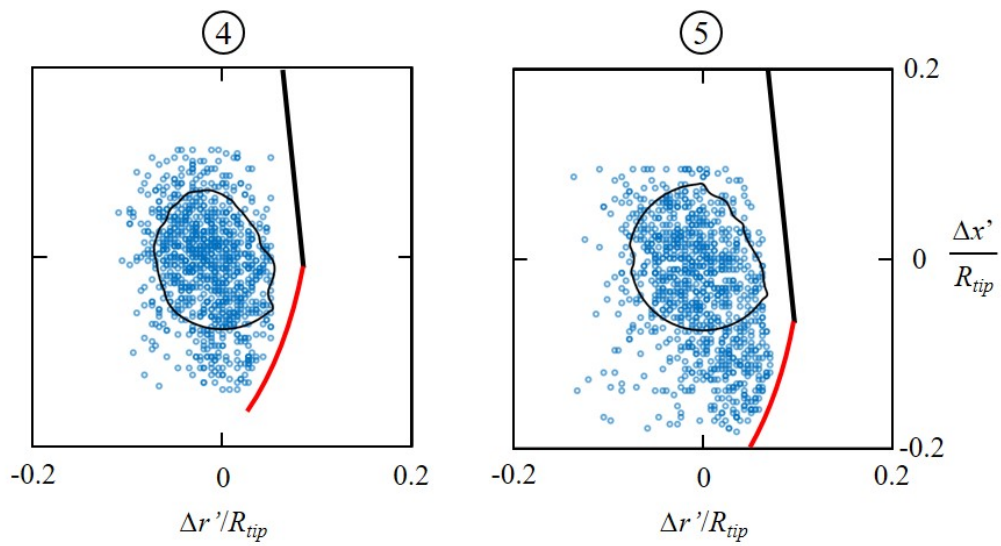


Figure 3.36. Scatter plot of the location of the TLV center for  $\varphi = 0.276$ . These scatter plots are obtained from 950 – 1,000 instantaneous flow fields. The number on the top of each figure denotes the measurement location shown in Figure 3.31.

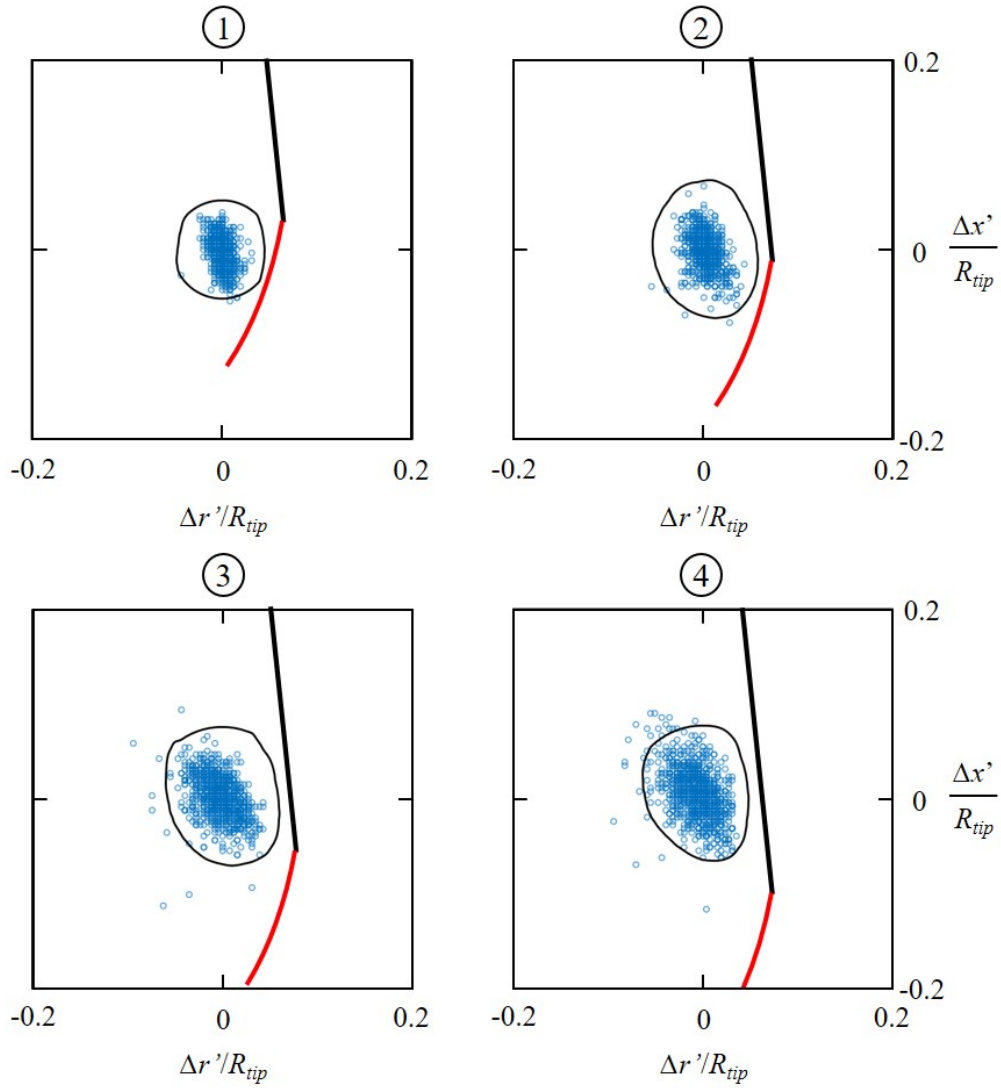


Figure 3.37. Scatter plot of the location of the TLV center for  $\varphi = 0.353$ . These scatter plots are obtained from 950 – 1,000 instantaneous flow fields. The number on the top of each figure denotes the measurement location shown in Figure 3.31.

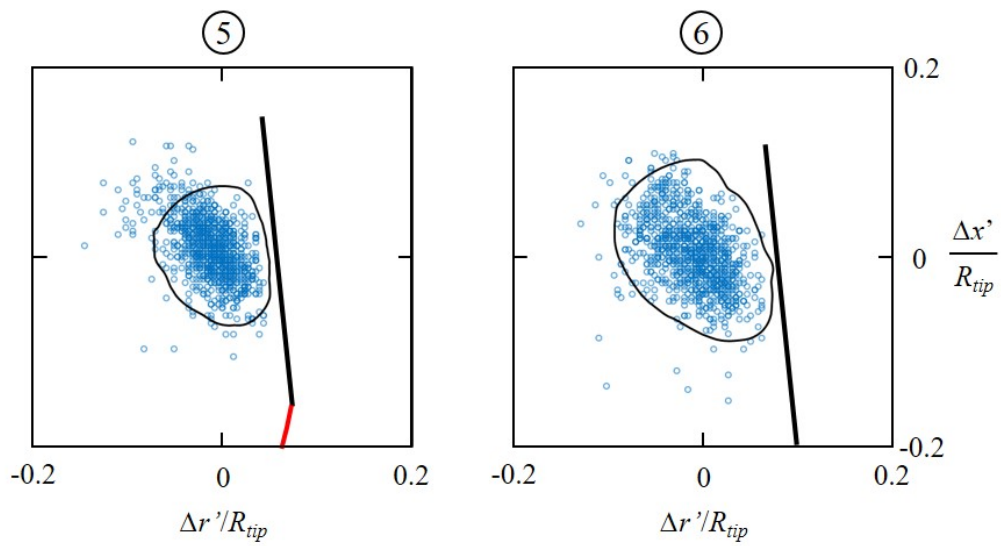


Figure 3.38. Scatter plot of the location of the TLV center for  $\varphi = 0.353$ . These scatter plots are obtained from 950 – 1,000 instantaneous flow fields. The number on the top of each figure denotes the measurement location shown in Figure 3.31.

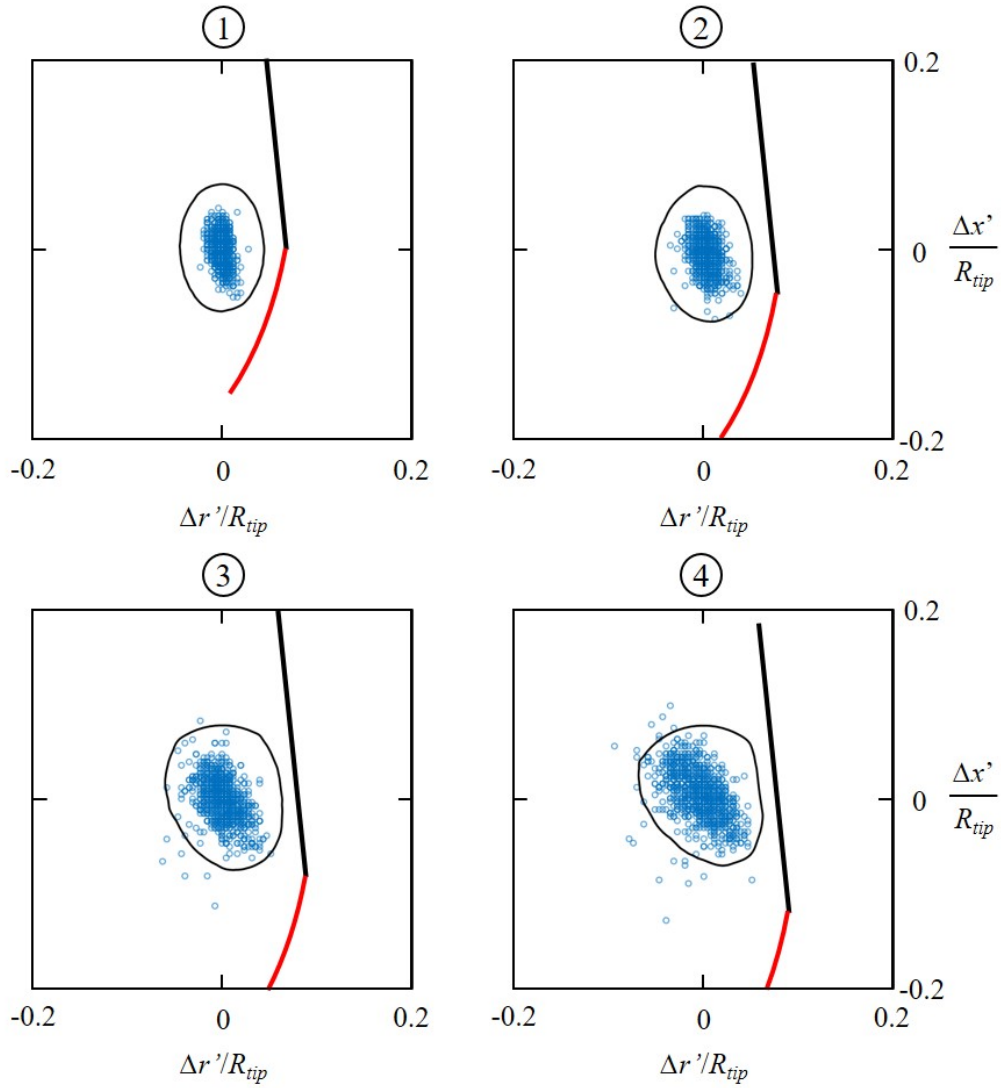


Figure 3.39. Scatter plot of the location of the TLV center for  $\varphi = 0.366$ . These scatter plots are obtained from 950 – 1,000 instantaneous flow fields. The number on the top of each figure denotes the measurement location shown in Figure 3.31.

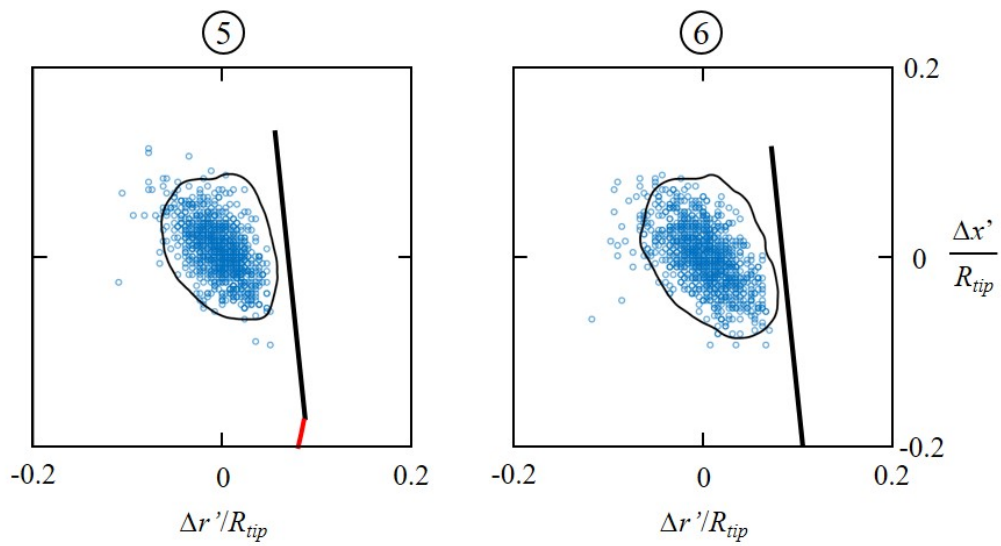


Figure 3.40. Scatter plot of the location of the TLV center for  $\varphi = 0.366$ . These scatter plots are obtained from 950–1,000 instantaneous flow fields. The number on the top of each figure denotes the measurement location shown in Figure 3.31.

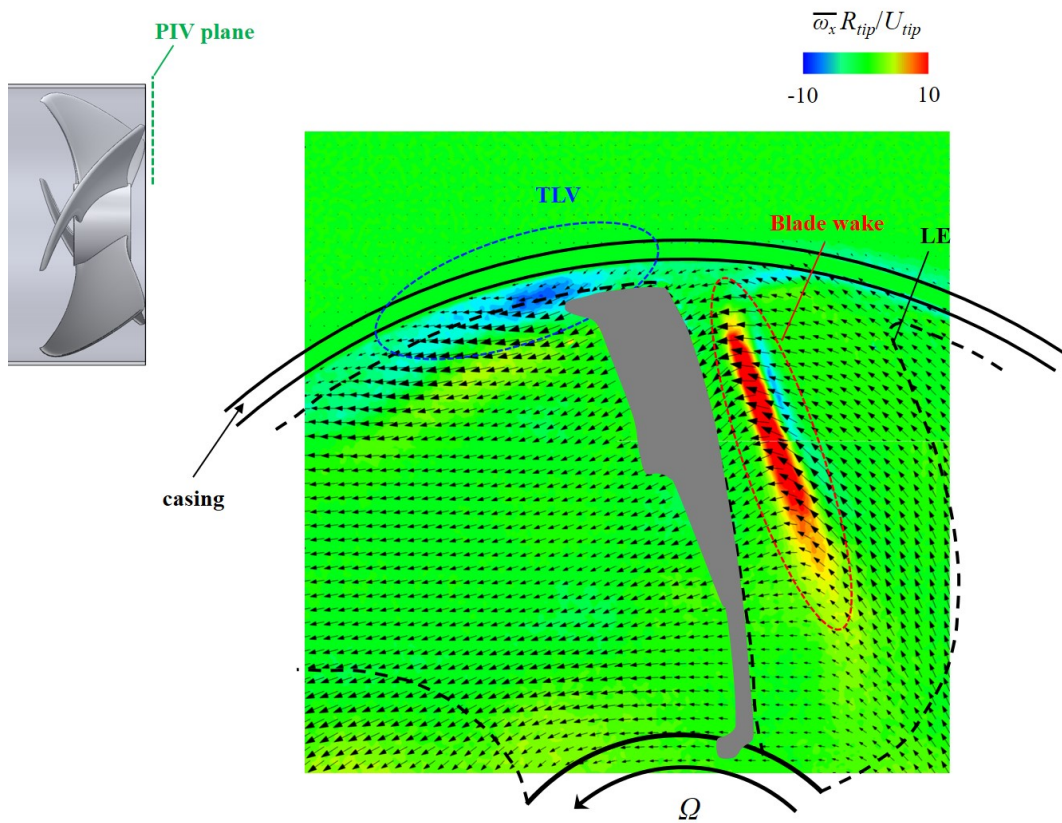


Figure 3.41. Contours of the phase-averaged axial vorticity, together with the phase-averaged velocity at  $x/R_{tip} = 0.05$  for  $\varphi = 0.353$ . The gray area indicates where PIV is not performed due to excessive exposure by laser light reflected from the blade.

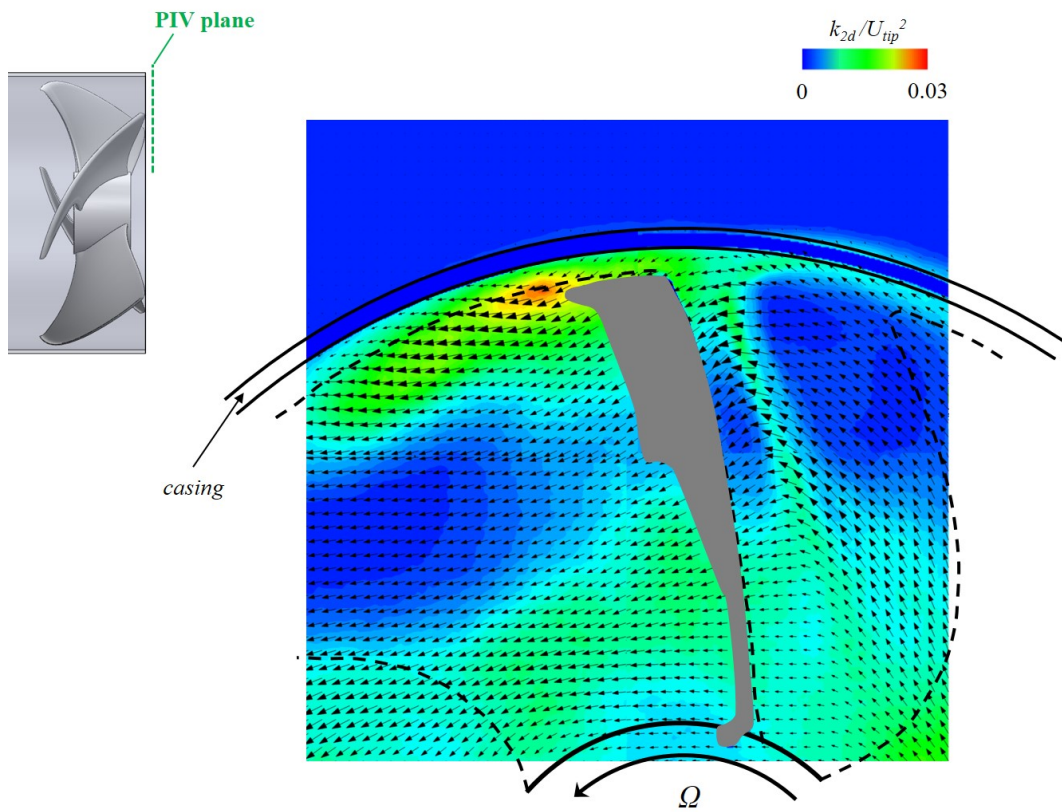


Figure 3.42. Contours of the 2D turbulent kinetic energy and phase-averaged velocity vectors on the  $r - \vartheta$  PIV plane at  $x/R_{tip} = 0.05$  for  $\varphi = 0.353$ . The gray area indicates where PIV is not performed due to excessive exposure by laser light reflected from the blade.



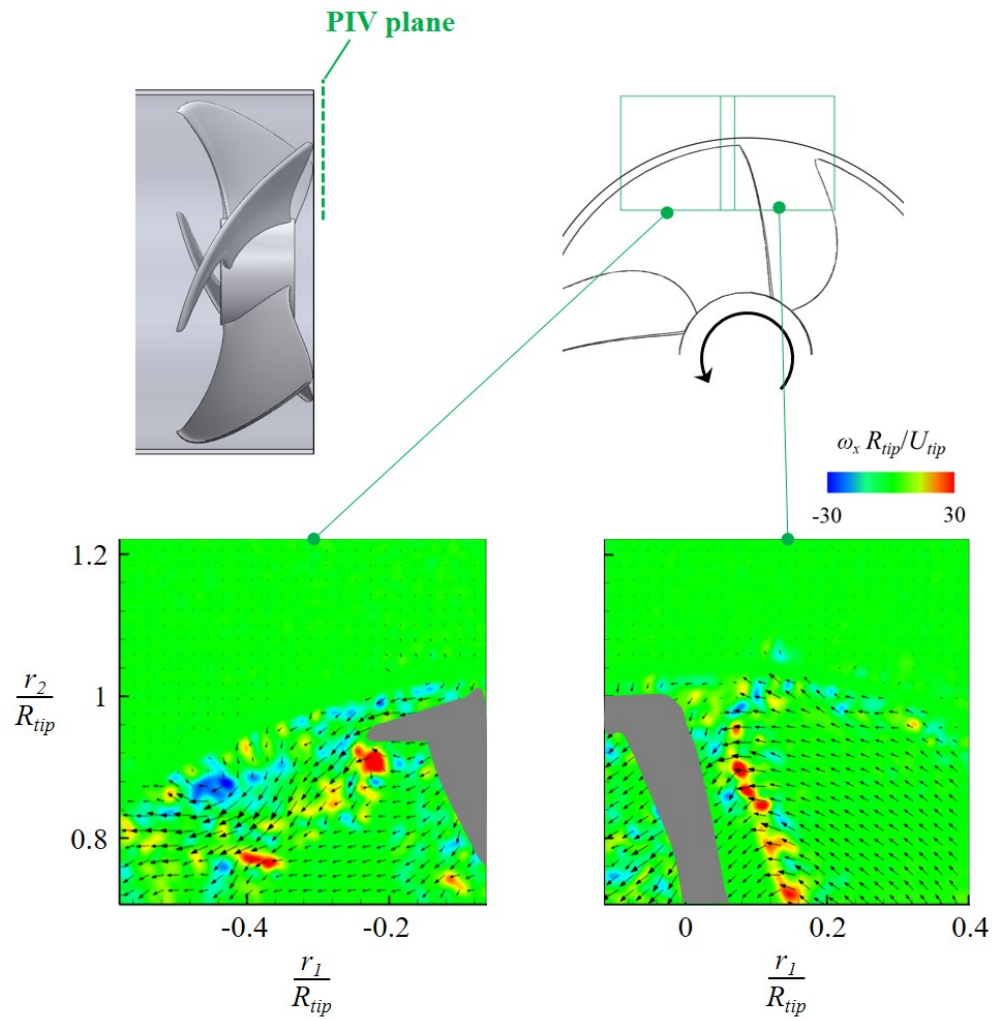


Figure 3.43. Instantaneous velocity vectors and contours of the instantaneous axial vorticity at  $x/R_{tip} = 0.05$  for  $\varphi = 0.353$ . The gray area indicates where PIV is not performed due to excessive exposure by laser light reflected from the blade.

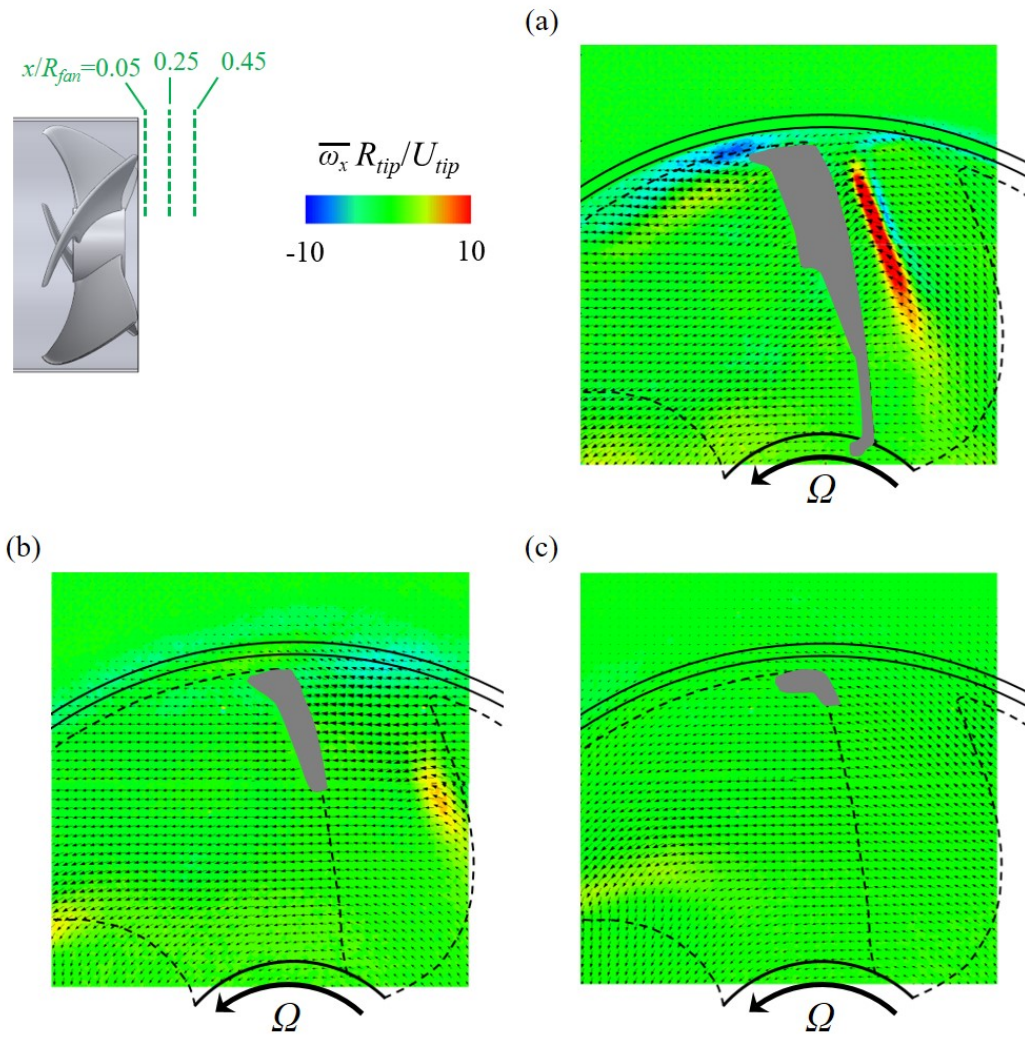


Figure 3.44. Contours of the phase-averaged axial vorticity, together with the phase-averaged velocity at various positions for  $\varphi = 0.353$ : (a)  $x/R_{tip} = 0.05$ ; (b)  $x/R_{tip} = 0.25$ ; (c)  $x/R_{tip} = 0.45$ . The gray area indicates where PIV is not performed due to excessive exposure by laser light reflected from the blade.

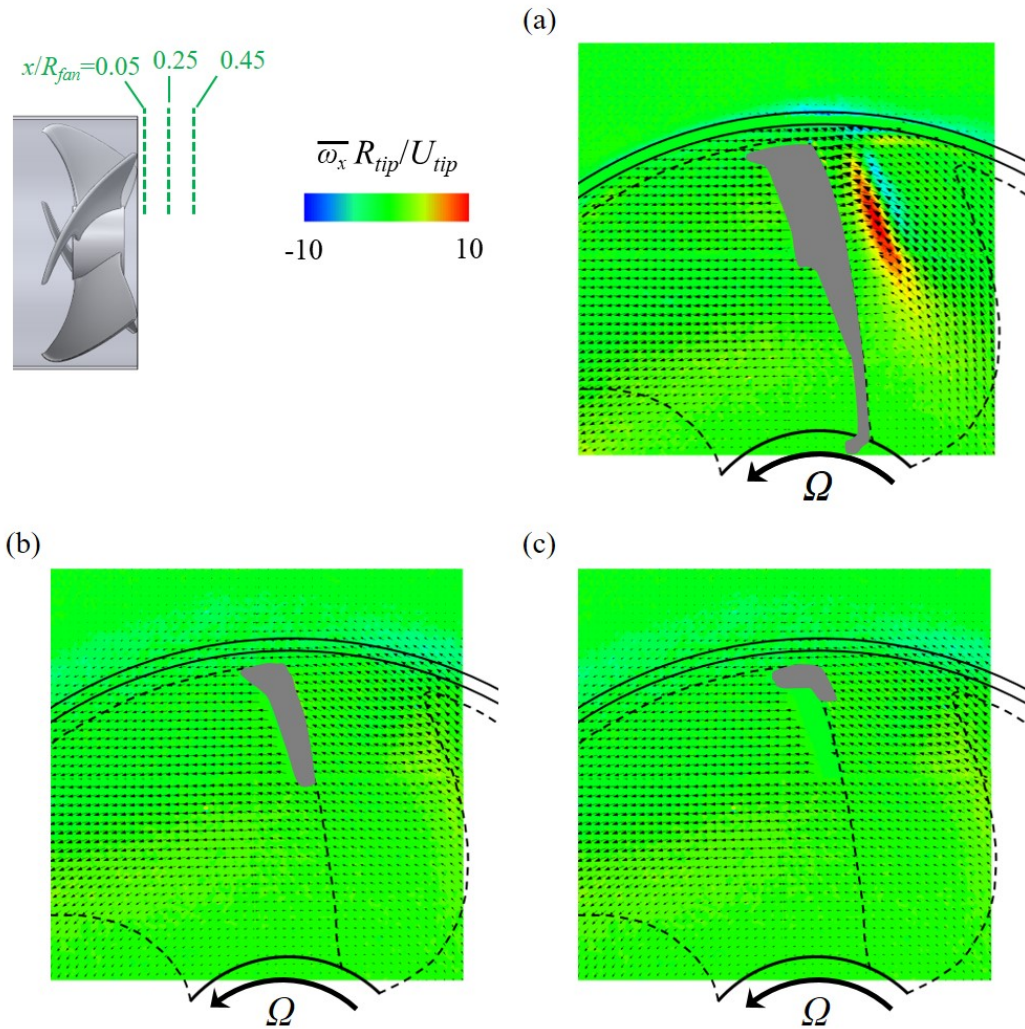


Figure 3.45. Contours of the phase-averaged axial vorticity, together with the phase-averaged velocity at various positions for  $\varphi = 0.276$ : (a)  $x/R_{tip} = 0.05$ ; (b)  $x/R_{tip} = 0.25$ ; (c)  $x/R_{tip} = 0.45$ . The gray area indicates where PIV is not performed due to excessive exposure by laser light reflected from the blade.

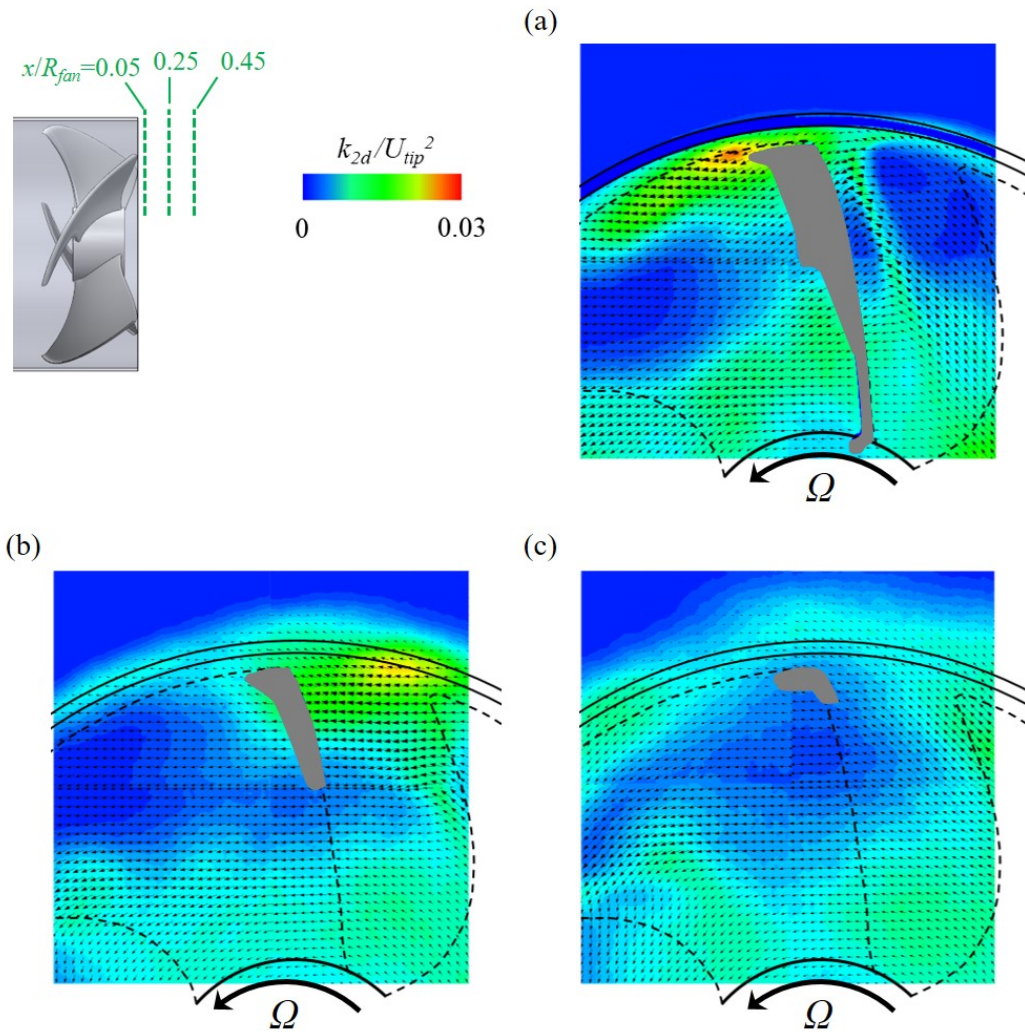


Figure 3.46. Contours of the 2D turbulent kinetic energy and phase-averaged velocity vectors on the  $r - \vartheta$  PIV plane at various positions for  $\varphi = 0.353$ : (a)  $x/R_{tip} = 0.05$ ; (b)  $x/R_{tip} = 0.25$ ; (c)  $x/R_{tip} = 0.45$ . The gray area indicates where PIV is not performed due to excessive exposure by laser light reflected from the blade.

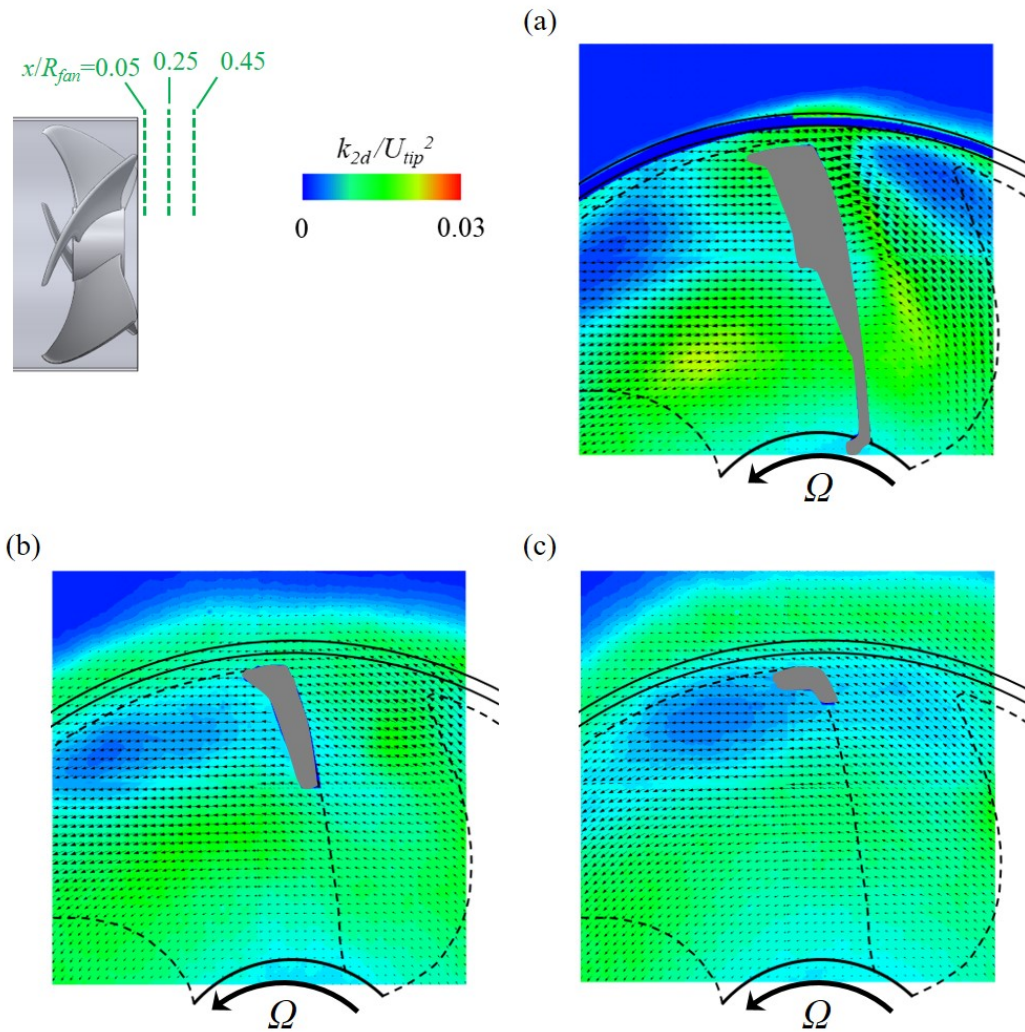


Figure 3.47. Contours of the 2D turbulent kinetic energy and phase-averaged velocity vectors on the  $r - \vartheta$  PIV plane at various positions for  $\varphi = 0.276$ : (a)  $x/R_{tip} = 0.05$ ; (b)  $x/R_{tip} = 0.25$ ; (c)  $x/R_{tip} = 0.45$ . The gray area indicates where PIV is not performed due to excessive exposure by laser light reflected from the blade.

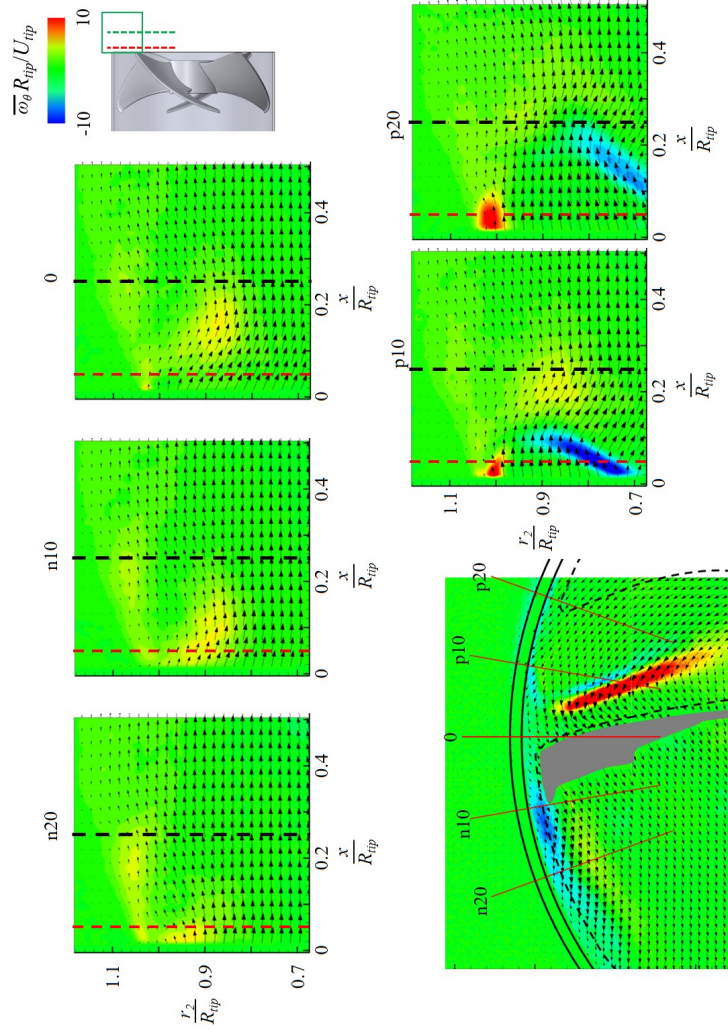


Figure 3.48. Contours of the phase-averaged circumferential vorticity and phase-averaged velocity vectors on the  $x-r$  PIV plane at various phases for  $\varphi = 0.353$ . The gray area indicates where PIV is not performed by excessive exposure due to laser light reflected from the blade.

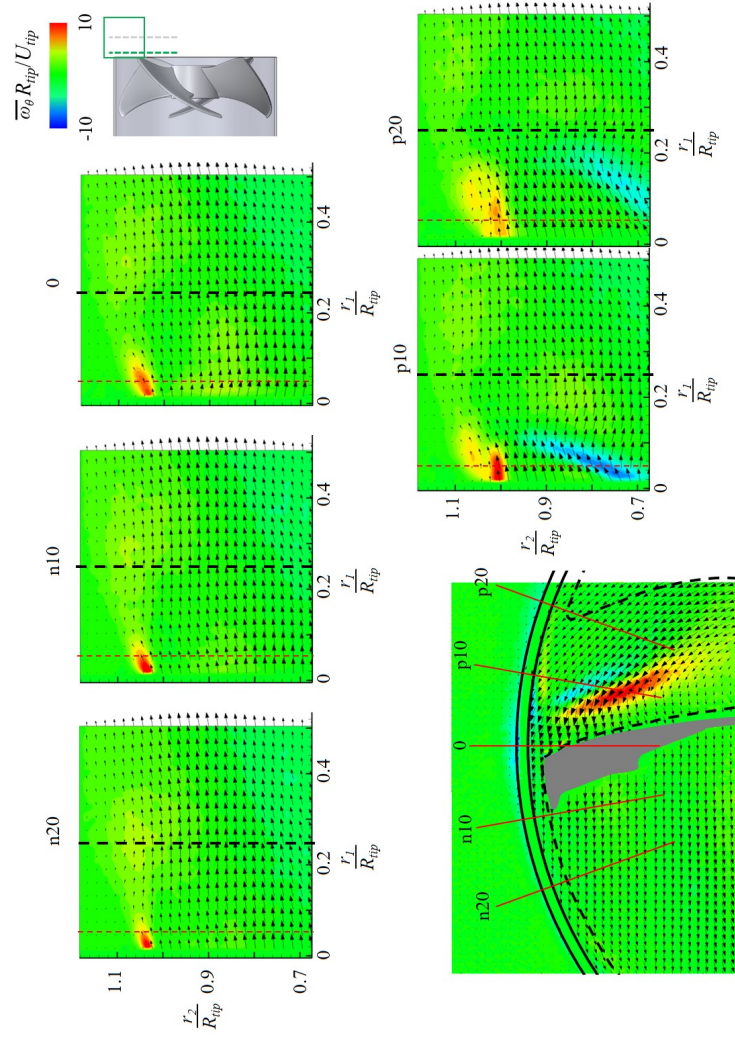


Figure 3.49. Contours of the phase-averaged circumferential vorticity and phase-averaged velocity vectors on the  $x-r$  PIV plane at various phases for  $\varphi = 0.276$ . The gray area indicates where PIV is not performed by excessive exposure due to laser light reflected from the blade.

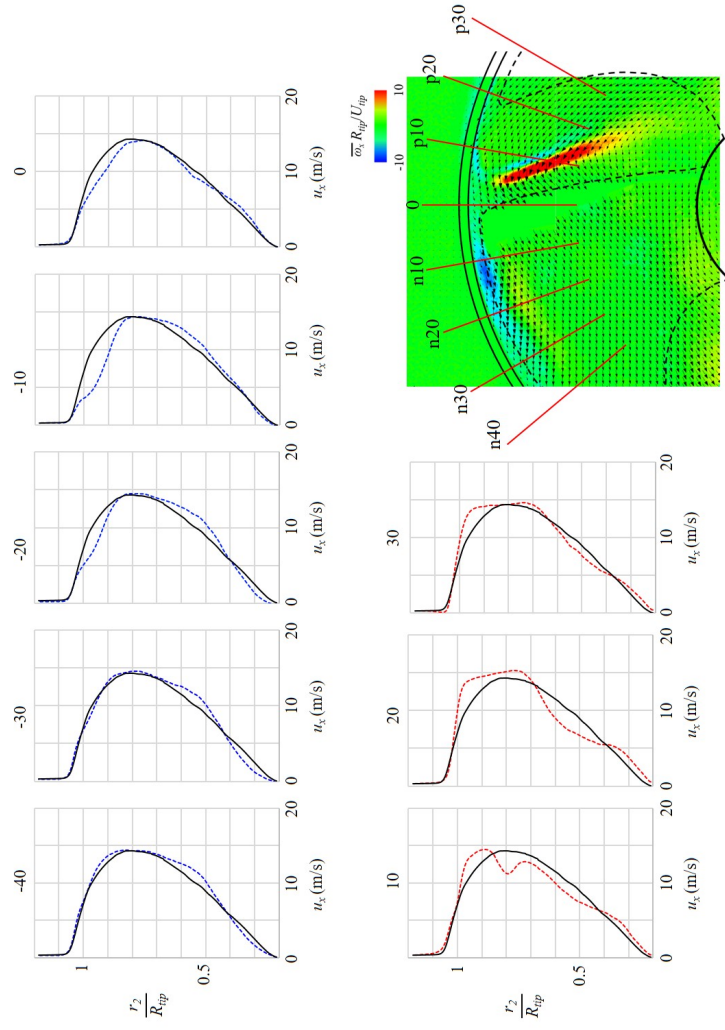


Figure 3.50. The phase-averaged axial velocity profiles for various phase and unconditionally averaged axial velocity profile at  $x/R_{tip} = 0.05$  for  $\varphi = 0.353$ .



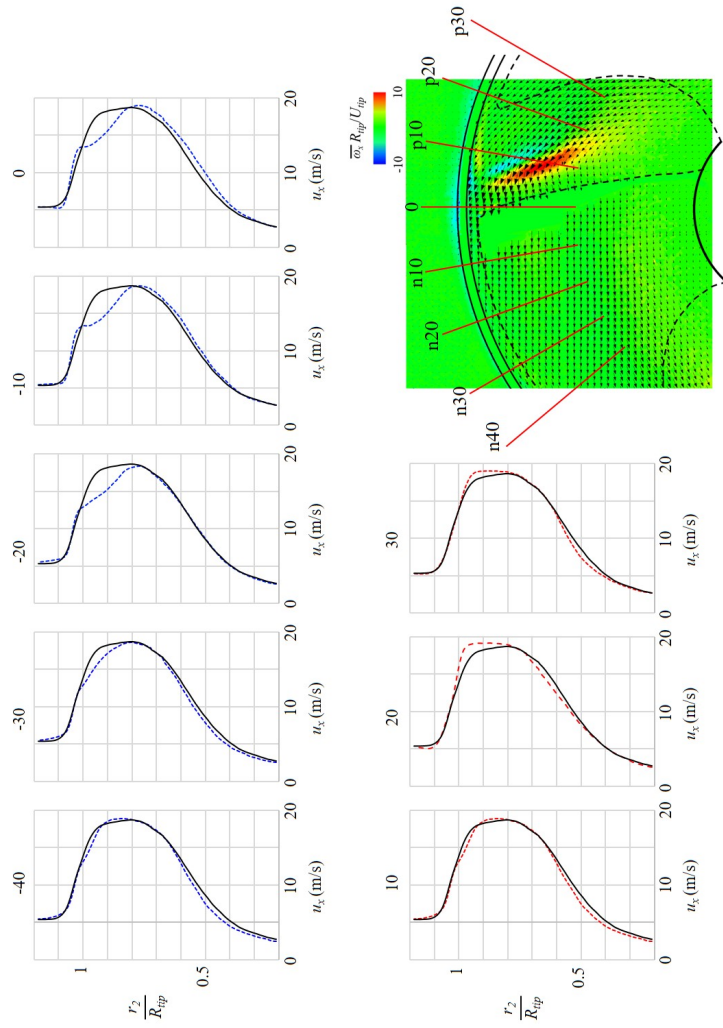


Figure 3.51. The phase-averaged axial velocity profiles for various phase and unconditionally averaged axial velocity profile at  $x/R_{tip} = 0.05$  for  $\varphi = 0.276$ .

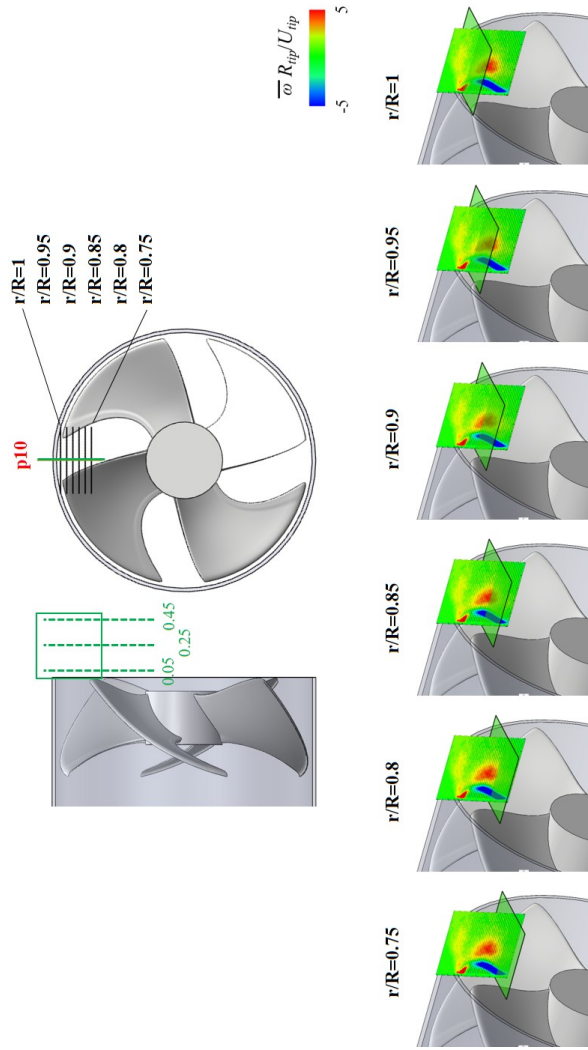


Figure 3.52. Contours of the phase-averaged circumferential vorticity and the phase-averaged velocity vectors for  $\varphi = 0.353$  with  $x - r'$  PIV planes.

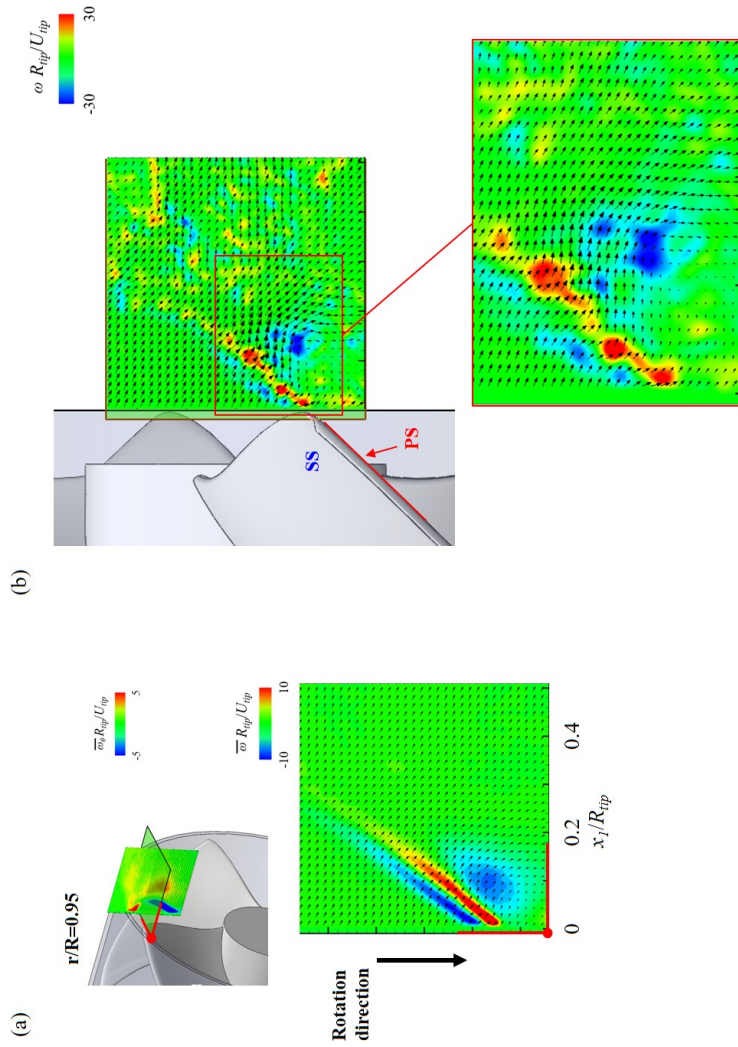


Figure 3.53. The phase-averaged and instantaneous vorticity in the direction normal to the PIV planes, together with velocity vectors at  $r/R_{tip} = 0.95$  for  $\varphi = 0.353$ .

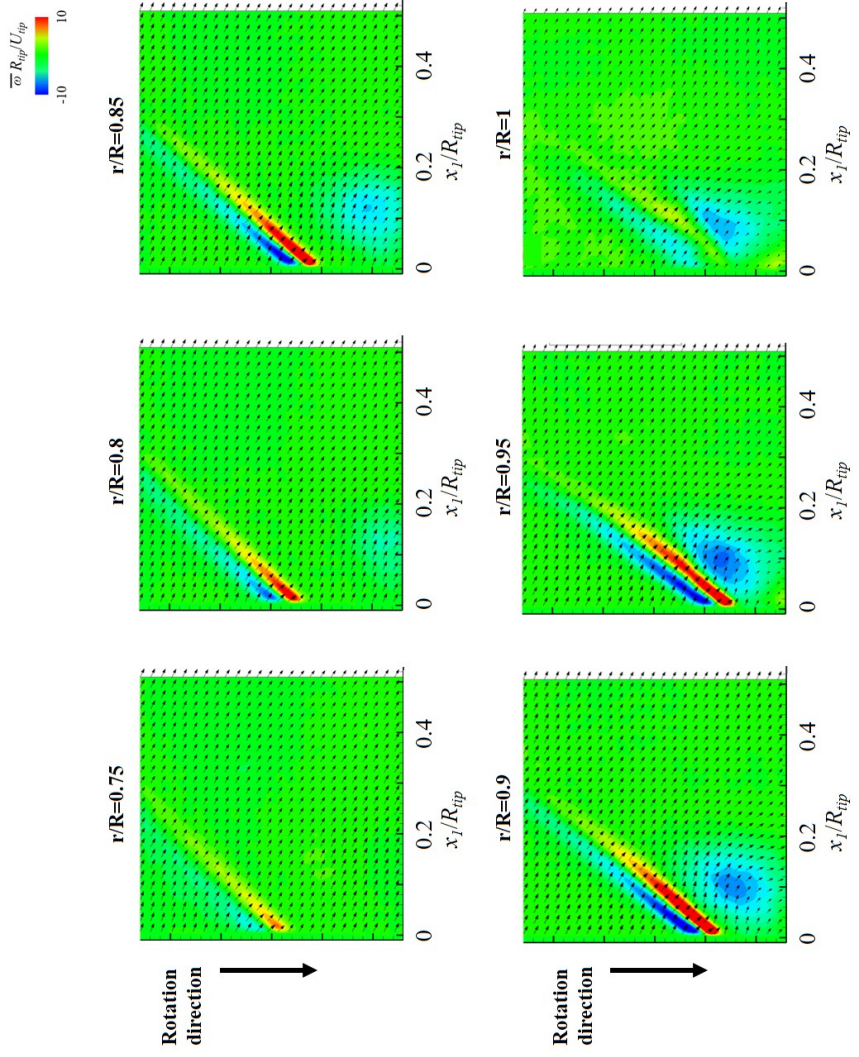


Figure 3.54. Contours of the phase-averaged vorticity in the direction normal to the PIV planes, together with the phase-averaged velocity vectors for  $\varphi = 0.353$ .

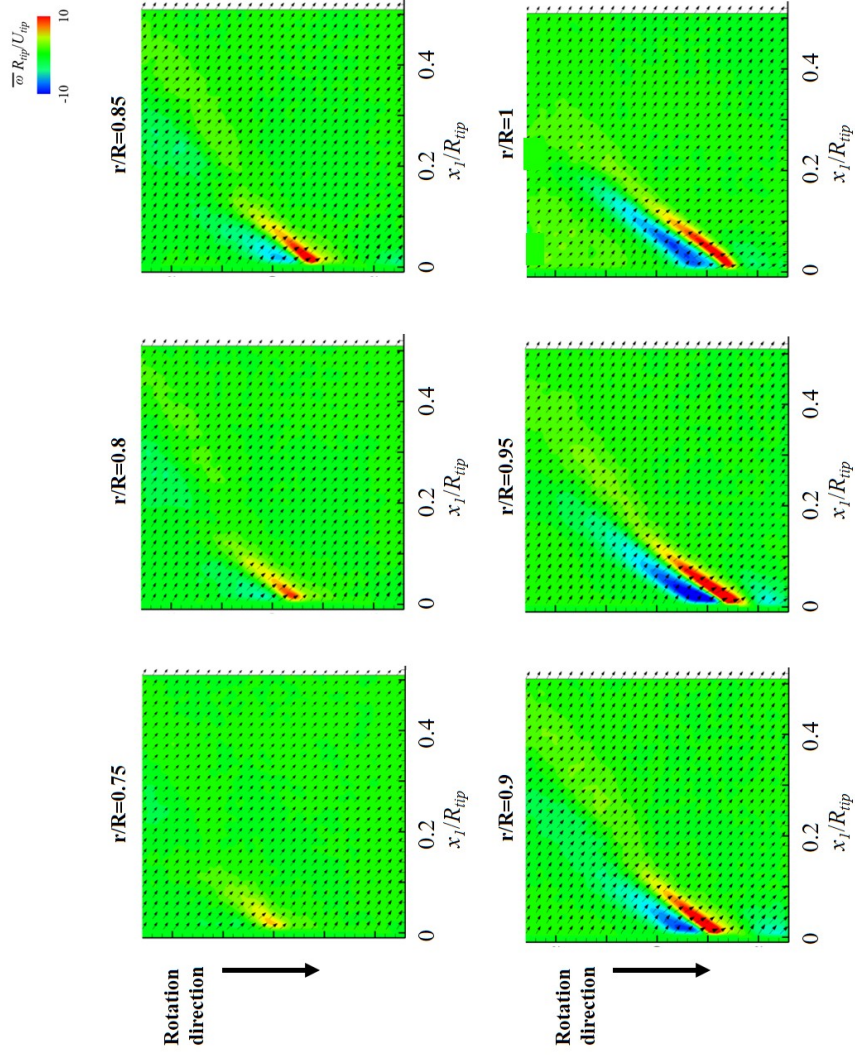


Figure 3.55. Contours of the phase-averaged vorticity in the direction normal to the PIV planes, together with the phase-averaged velocity vectors for  $\varphi = 0.276$ .

## Chapter 4

### Summary and Concluding Remarks

In the present study, we measured the velocity fields inside the passage of rotating blades in a low-pressure axial flow fan operating at  $Re = 547,000$  using a digital particle image velocimetry (PIV), to investigate the evolution of the tip-leakage vortex (TLV). The rotational speed was fixed at 1,000 rpm for four different flow rates (i.e., stall, peak efficiency, and two higher flow rates). The evolution of TLV in the downstream was highly influenced by the incoming flow rate. For higher flow rates, the TLV traveled downstream while losing its strength, but the TLV breakup did not happen. As the TLV interacted with the main flow, discrete positive and negative vorticity peaks were generated upstream and on the left side of the TLV. At the peak efficiency and lower flow rates, the TLV broke into several pieces of small-scale vortices. Due to the TLV breakup at the peak efficiency condition, the phase-averaged TLV quickly diffused away downstream. The migration speed of the TLV at the peak efficiency condition was faster than those at higher flow rates. The mean location of the TLV center was highly correlated with that of the peak 2D turbulent kinetic energy ( $k_{2D}$ ), but the  $k_{2D}$  at the re-centered TLV center was significantly reduced up to 20 % of the original  $k_{2D}$  value. These results indicated that the TLV wanders around and this wandering motion contributes to a large portion of the turbulent kinetic energy at the TLV center. The wandering motion of the TLV was also confirmed from the scatter plots of

the instantaneous TLV center. The area swept by the wandering motion was larger than the size of the phase-averaged TLV, and increased as the TLV migrated downstream. The wandering motion of the TLV has been known to be a significant loss (Oweis & Ceccio, 2005). Therefore, to improve the performance of the axial flow fan, it is necessary to weaken the TLV wandering motion.

## References

- AKTURK, A. & CAMCI, C. 2014 Tip Clearance Investigation of a Ducted Fan Used in VTOL Unmanned Aerial Vehicles-Part II: Novel Treatments Via Computational Design and Their Experimental Verification. *J. Turbomach. Trans. ASME* **136**, 021005.
- CAI, W. X., SHIOMI, N., SASAKI, K., KANEKO, K. & SETOGUCHI, T. 2002 Visualization of tip vortex flow, in an open axial fan by EFD. *J. Visualization* **5**, 293–300.
- COLEMAN, H. W. & STEELE, W. G. 2009 Experimentation, validation, and uncertainty analysis for engineers. John Wiley & Sons, New York.
- CORSINI, A., RISPOLI, F. & SHEARD, A. G. 2007 Development of improved blade tip endplate concepts for low-noise operation in industrial fans. *Proc. Inst. Mech. Eng. Part A-J. Power Energy* **221**, 669–681.
- DENTON, J. D. 1993 The 1993 IGTI scholar lecture - loss mechanisms in turbomachines. *J. Turbomach. Trans. ASME* **115**, 621–656.
- FIKE, M., BOMBEEK, G., HRIBERSEK, M. & HRIBERNIK, A. 2014 Visualisation of rotating stall in an axial flow fan. *Exp. Therm. Fluid Sci.* **53**, 269–276.
- FISCHER, A., BUTTNER, L., CZARSKE, J., GOTTSCHALL, M., VOGELER, K. & MAILACH, R. 2012 Investigation of the tip clearance flow in a compressor cascade using a novel laser measurement technique with high temporal resolution. *J. Turbomachinery* **134**, 051004.
- FUKANO, T. & JANG, C. M. 2004 Tip clearance noise of axial flow fans



- operating at design and off-design condition. *J. Sound Vibr.* **275**, 1027–1050.
- HAH, C., HATHAWAY, M., KATZ, J. & TAN, D. 2015 Investigation of unsteady tip clearance flow in a low-speed one and half stage axial compressor with LES and PIV. *Proc. of ASME/JSME/KSME 2015 Joint Fluids Eng. Conference.*
- HANSEN, K. L., ROSTAMZADEH, N., KELSO, R. M. & DALY, B. B. 2016 Evolution of the streamwise vortices generated between leading edge tubercles. *J. Fluid Mech.* **788**, 730–766.
- HEO, S., HA, M., KIM, T. H. & CHEONG, C. 2015 Development of high-performance and low-noise axial-flow fan units in their local operating region. *J. Mech. Sci. Technol.* **29**, 3653–3662.
- HEYES, A., JONES, R. & SMITH, D. 2004 Wandering of wing-tip vortices. *Proc. 12th Int. Symp. App. Laser Techniq. Fluid Mech.* .
- INOUE, M., KUROUNARU, M. & FUKUHARA, M. 1986 Behavior of tip leakage flow behind an axial compressor rotor. *J. Eng. Gas Turbines Power-Trans. ASME* **108**, 7–14.
- JANG, CM, FURUKAWA, M. & INOUE, M. 2001 Analysis of vortical flow field in a propeller fan by LDV measurements and LES - Part I: Three-dimensional vortical flow structures. *J. Fluid Eng.-Trans. ASME* **123**, 748–754.
- JANG, CM, FURUKAWA, M. & INOUE, M. 2001 Analysis of vortical flow field in a propeller fan by LDV measurements and LES - Part II: Unsteady nature of vortical flow structures due to tip vortex breakdown. *J. Fluid Eng.-Trans. ASME* **123**, 755–761.
- JANG, CM, SATO, D. & FUKANO, T. 2005 Experimental analysis on tip

- leakage and wake flow in an axial flow fan according to flow rates. *J. Fluid Eng.* **127**, 322–329.
- JIN, G. Y., OUYANG, H., WU, Y. D. & DU, Z. H. 2011 An experimental study of the unsteady characteristics of tip-leakage flow of axial fans with circumferential skewed blades at off-design conditions. *Proc. Inst. Mech. Eng. Part A-J. Power Energy* **225**, 802–816.
- JUNG, J. H. & JOO, W. G. 2018 Effect of tip clearance, winglets, and shroud height on the tip leakage in axial flow fans. *Int. J. Refrig.-Rev. Int. Froid* **93**, 195–204.
- KHALID, S. A., KHALSA, A. S., WAITZ, I. A., TAN, C. S., GREITZER, E. M., CUMPSTY, N. A., ADAMCZYK, J. J. & MARBLE, F. E. 1999 Endwall blockage in axial compressors. *J. Turbomach-Trans. ASME* **121**, 499–509.
- KIM, J., OVGOR, B., CHA, K., KIM, J., LEE, S. & KIM, K. 2014 Optimization of the Aerodynamic and Aeroacoustic Performance of an Axial-Flow Fan. *AIAA J.* **52**, 2032–2044.
- LAKSHMINARAYANA, B. 1996 Fluid dynamics and heat transfer of turbomachinery. John Wiley & Sons, New York.
- LEE, G., BAEK, J. & MYUNG, H. 2005 Effect of blade loading on the structure of tip leakage flow in a forward-swept axial-flow fan. *HVAC & R Research* **11**, 95–117.
- LEE, G., BAEK, J. & MYUNG, H. 2003 Structure of tip leakage flow in a forward-swept axial-flow fan. *Flow Turbul. Combust.* **70**, 241–265.
- LEE, S., CHOI, J. & LEE, I. 2001 Velocity Field Measurements of Swirl Flow around a Forward-swept Axial Fan Using a Phase-averaged PTV. *J. Visualization* **4**, 257–265.

- LEE, S., CHOI, J. & YOON, J. 2001 Phase-averaged velocity field measurements of flow around an isolated axial-fan model. *J. Fluid Eng.-Trans. ASME* **125**, 1067–1072.
- LI, Y., CHEN, H. & KATZ, J. 2017 Measurements and Characterization of Turbulence in the Tip Region of an Axial Compressor Rotor. *J. Turbomach.-Trans. ASME* **139**, 10.
- LIU, B., WANG, H., LIU, H., YU, H., JIANG, H. & CHEN, M. 2003 Experimental investigation of unsteady flow field in the tip region of an axial compressor rotor passage at near stall condition with SPIV. *ASME Turbo Expo* , 877–888.
- LIU, P., SHIOMI, N., KINOUE, Y., JIN, Y. & SETOGUCHI, T. 2012 Effect of Inlet Geometry on Fan Performance and Flow Field in a Half-Ducted Propeller Fan. *Int. J. Rotating Machinery* **2012**.
- MAILACH, R., LEHMANN, I. & VOGELER, K. 2001 Rotating instabilities in an axial compressor originating from the fluctuating blade tip vortex. *J. Turbomach.-Trans. ASME* **123**, 453–460.
- MIORINI, R., WU, H. & KATZ, J. 2012 The internal structure of the tip leakage vortex within the rotor of an axial waterjet pump. *J. Turbomachinery* **134**, 031018.
- MYUNG, H. & BAEK, J. 1999 Mean velocity characteristics behind a forward-swept axial-flow fan. *JSME Int. J. Series B Fluids Therm. Eng.* **42**, 472–488.
- NASHIMOTO, A., FUJISAWA, N., AKUTO, T. & NAGASE, Y. 2004 Measurements of aerodynamic noise and wake flow field in a cooling fan with winglets. *J. Visualization* **7**, 85–92.
- NASHIMOTO, A., FUJISAWA, N., NAKANO, T. & YODA, T. 2008 Visualiza-

- tion of aerodynamic noise source around a rotating fan blade. *J. Visualization* **11**, 365–373.
- OWEIS, G. & CECCIO, S. 2005 Instantaneous and time-averaged flow fields of multiple vortices in the tip region of a ducted propulsor. *Exp. Fluids* **38**, 615–636.
- PAIK, B., KIM, K., LEE, J. & LEE, S. 2010 Analysis of unstable vortical structure in a propeller wake affected by a simulated hull wake. *Exp. Fluids* **48**, 1121–1133.
- PARK, K., CHOI, H., CHOI, S., SA, Y. & KWON, O. 2017 Unsteady characteristics of tip-leakage flow in an axial flow fan. *10th Int. Symp. Turbulence Shear Flow Phenomena (TSFP)* .
- RAFFEL, M., WILLERT, C. & KOMPENHANS, JURGEN 2007 Particle image velocimetry: a practical guide. Springer Science & Business Media.
- TAN, D., LI, Y., WILKES, I., VAGNONI, E., MIORINI, R. & KATZ, J. 2015 Experimental Investigation of the Role of Large Scale Cavitating Vortical Structures in Performance Breakdown of an Axial Waterjet Pump. *J. Fluids Eng. - Trans. ASME* **137**, 14.
- WANG, H., TIAN, J., OUYANG, H., WU, Y. & DU, Z. 2014 Aerodynamic performance improvement of up-flow outdoor unit of air conditioner by redesigning the bell-mouth profile. *Int. J. Refrig-Rev. Int. Du Froid* **46**, 173–184.
- WILLERT, C. & GHARIB, M. 1991 Digital particle image velocimetry. *Exp. Fluids* **10**, 181–193.
- WU, H., MIORINI, R. & KATZ, J. 2011 Measurements of the tip leakage vortex structures and turbulence in the meridional plane of an axial waterjet pump. *Exp. Fluids* **50**, 989–1003.

- WU, H., MIORINI, R., TAN, D. & KATZ, J. 2012 Turbulence Within the Tip-Leakage Vortex of an Axial Waterjet Pump. *AIAA J.* **50**, 2574–2587.
- YU, X. & LIU, B. 2007 Stereoscopic PIV measurement of unsteady flows in an axial compressor stage. *Exp. Therm. Fluid Sci.* **31**, 1049–1060.
- ZHANG, D., SHI, W., VAN ESCH, BPM, SHI, L. & DUBUISSON, M. 2015 Numerical and experimental investigation of tip leakage vortex trajectory and dynamics in an axial flow pump. *Compt. Fluids* **112**, 61–71.

# 축류팬에서 익단 누설 유동의 방랑 운동에 대한 실험적 연구

서울대학교 대학원

기계항공공학부

이 홍 권

## 요 약

저압 축류 팬에서 익단 누설 와류의 특성을 디지털 입자 영상 유속계를 이용하여 분석하였다. 팬 날개의 회전 속도를 1,000 rpm으로 고정하여, 날개 반경 길이와 날개 끝 속도를 기준으로 한 레이놀즈 수가 547,000인 팬에서 네 가지 서로 다른 유량을 고려하였다. 하류에서 익단 누설 와류의 발달은 유입 유량에 크게 영향을 받는다. 높은 유량 조건에서 강한 익단 누설 와류가 관찰되고 최대 효율 및 실속 조건에서는 익단 누설 와류가 팬 날개의 후연에서 분열된다. 높은 유량 조건에서도 간헐적으로 익단 누설 와류의 분열이 관찰된다. 유량이 감소함에 따라 익단 누설 와류는 보다 상류에 위치하며 최대 효율 조건에서 익단 누설 와류의 분열로 인해 높은 유량 조건보다 이동 속도가 빠르다. 순간 유동장에서 익단 누설 와류 중심 위치의 분포는 익단 누설 와류가 평균 유동장의 익단 누설 와류 중심 주위를 방랑하고, 익단 누설 와류가 하류로 이동함에 따라 방랑 운동의 크기가 증가함을 나타낸다. 익단 누설 와류의 방랑 운동과 주 유동과의 상호 작용으로 인해 위상 평균 된 익단 누설 와류 중심과 익단 누설 와류의 상류 지점에 높은 난류 운동 에너지가 존재한다. 한편, 높은 유량 조건에서 팬 날개 후연과 케이싱 벽 근처에 존재하는 강한 익단 누설 와류는 팬 덕트 출구로 나가면서 그 강도가 급격히 감소한다. 출구 하류에서 익단 누설 와류의 원주 방향 이동 속도는 날개 후류의 이동 속도보다 빨라 다음 날개의 후류와 상호작용하게 된다. 이때, 익단 누설 와류는 날개 후류와 함께 주 유동의 흐름을 방해하고 팬 성능을 저하시킨다.

.....  
주요어 : 축류팬, 입자 영상 유속계, 익단 누설 와류, 방랑 운동,  
분열

학 번 : 2009-20713